UNIVERSITY OF
LIVERPOOL

School of Engineering

PhD Thesis

Femtosecond laser internal structuring of transparent materials using a spatial light modulator

Thesis submitted in accordance with the requirements of
the University of Liverpool for the degree of
Doctor of Philosophy
by

Dun Liu

Laser Group
School of Engineering
University of Liverpool
Brownlow Street
Liverpool
L69 3GH
UK

February 2011

Abstract

A Spatial Light Modulator (SLM), addressed with optimised Computer Generated Holograms (CGHs) has been integrated with a femtosecond laser system (1 kHz, 170 fs, λ = 775 nm) to create a dynamic parallel beam processing system. By focussing the ultrahigh intensity parallel beams inside clinical grade poly(methyl methacrylate) (PMMA) while carefully controlling filamentation and eliminating pulse front tilt, uniform refractive index modification allowed the parallel direct writing of high quality volume Bragg gratings for the first time. At λ = 775 nm, the first order diffraction efficiency η of a series of gratings with dimension 5 × 5 mm^2 with varying thickness L (1-4 mm) and period Λ = 19 μm fit the theoretical curve $\eta = \sin^2\varphi$, confirming that highly uniform modification throughout was achieved with η_{max} = 75% at 4 mm thickness and refractive index change $\Delta n = 4.6 \times 10^{-5}$. Fabrication time was approximately 50 minutes using 16 parallel beams. By placing a thin nonlinear beta-BaB_2O_4 (BBO) crystal after the SLM, parallel beam direct writing of 5 × 5 mm^2, 15 μm pitch volume Bragg gratings at λ = 387 nm was achieved, reaching the diffraction efficiency η_{max} = 70% with a 2 mm thickness and inferred $\Delta n = 8.4 \times 10^{-5}$ with fabrication time only 18minutes using 18 parallel beams. Gratings written at λ = 775 nm show time dependent diffraction efficiency over weeks to months, related to the diffusion of monomer MMA after exposure. On the contrary, those created at λ = 387 nm stabilise after a few days and are potentially useful photonic components in integrated optics. Internal structuring of fused silica is also demonstrated along with dynamic modification of PMMA by running pre-calculated CGHs in real time.

Declaration

I hereby declare that all of the work contained within this dissertation has not been submitted for any other qualification.

Signed:

Date:

Acknowledgements

I would like to thank everyone who encouraged and supported me during the time of my PhD.

Sincere acknowledge goes to my supervisors, Prof. Ken Watkins and Dr. Geoff Dearden, who always give me encouragement, help, advice and guidance through the ups and downs of my research. I would like to thank Dr. Walter Perrie for his invaluable advice, endless patience and support. Without their dedication, this work would not have been possible. I am very grateful to everyone from the Laser Group of the University of Liverpool who was involved in my research, in particular, Dr. Stuart Edwardson, Dr. Eamonn Fearon, Dr. Martin Sharp, Dr. Paul French, Dr. Zheng Kuang and Mr. Doug Eckford.

I thank Dr. Patricia Scully, Dr. Alexandra Baum, Miss Shijie Liang, Ms. Anca Taranu, and Mr Bo Pang, from the Photonic Science Institute of the University of the Manchester for providing kind help and advice for this research. I also acknowledge Prof. Miles Padgett and Dr. Jonathan Leach at the University of Glasgow for providing the hologram calculation software used for this research.

I would like to thank the UK North West Development Agency for providing financial support for this work (under grant N0003200).

Finally, I would like to sincerely acknowledge my beloved wife, Qin Liang, for her constant support and understanding, and my parents for their financial support and unwavering faith throughout my study in the UK.

List of publications to date

Journal papers:

1. **D. Liu**, Z. Kuang, W. Perrie, P. J. Scully, A. Baum, S. P. Edwardson, E. Fearon, G. Dearden, and K. G. Watkins, "High speed uniform parallel 3D refractive index micro-structuring of poly(methyl methacrylate) for volume phase gratings," Applied Physics B, 101, 817–823 (2010) - **First author.**

2. Z. Kuang, **D. Liu**, W. Perrie, J. Cheng, S. Shang, S. P. Edwardson, E. Fearon, G. Dearden, K. G. Watkins. "Diffractive Multi-beam Ultrafast Laser Micro-processing Using a Spatial Light Modulator (Invited Paper)," Chinese Journal of Lasers, 36 (12): 3093-3115 (2009) - **Corresponding author.**

3. **D. Liu**, W. Perrie, Z. Kuang, P. J. Scully, A. Baum, S. Liang, S. P. Edwardson, E. Fearon, G. Dearden, and K. G. Watkins, "Parallel ultrafast NUV 3D refractive index structuring of poly(methyl methacrylate)", - **Under review.**

4. S. Liang, P. J. Scully, J. Schille, J. Vaughan, M. Benyezzar, **D. Liu**, and W. Perrie, "3D refractive index structures written by femtosecond pulses at 400 nm in polymethyl methacrylate," Journal of Laser Micro/Nanoengineering, 5, 68-73 (2010)

5. A. Baum, P. J. Scully, W. Perrie, **D. Liu**, and V. Lucarini, "Mechanisms of femtosecond laser-induced refractive index modification of poly(methyl methacrylate)," Journal of Optical Society of the American B, 27, 107-111 (2010)

6. Z. Kuang, **D. Liu**, W. Perrie, S. Edwardson, M. Sharp, E. Fearon, G. Dearden and K. G. Watkins, "Fast parallel diffractive multi-beam femtosecond laser surface micro-structuring," Applied Surface Science, 255, 6582-6588 (2009)

7. Z. Kuang, W. Perrie, **D. Liu**, S. Edwardson, J. Cheng, G. Dearden, and K. G. Watkins, "Diffractive multi-beam surface micro-processing using 10ps laser pulses," Applied Surface Science, 255, 9040–9044 (2009)

8. A. Dima, M. Gagliardi, **D. Liu**, W. Perrie, C. J. Williams, I. Rendina, G. Dearden, and K. G. Watkins, "Nano-Silicon Sol-Gel Film Refraction Index Modulation with Femtosecond Laser", Solid State Phenomena, 154, 101-106 (2009)

9. A. Dima, M. Dima, K. G. Watkins, G. Dearden, **D. Liu**, C. J. Williams, M. Casalino, M. Gagliardi, I. Rendina, and F.G. Della Corte, "Switching devices in sol–gel hybrid thin film technology", Thin Solid Films, 517, 4658–4662 (2009)

Conference contributions:

1. **D. Liu**, W. Perrie, S. P. Edwardson, E. Fearon, G. Dearden and K. G. Watkins, "Femtosecond NUV parallel processing inside PMMA for volume Bragg gratings", Photonex 2010 - Optical Micro & Nano Fabrication meeting, Telford, October 2010

2. **D. Liu,** W. Perrie, Z. Kuang, P. J. Scully, S. Liang, A. Baum, A. Taranu, S.P. Edwardson, E. Fearon, G. Dearden, and K. G. Watkins, "Multiple beam refractive index modification of PMMA," Photon10, Southampton, August 2010

3. **D. Liu**, W. Perrie, Z. Kuang, S. P. Edwardson, E. Fearon, G. Dearden, and K. G. Watkins, "Picosecond laser processing using tuneable annular beam generated by a spatial light modulator," Photon10, Southampton, August 2010

4. **D. Liu**, W. Perrie, Z. Kuang, P. J. Scully, A. Baum, S. Liang, A. Taranu, S. P. Edwardson, E. Fearon, G. Dearden, and K. G. Watkins, "Multiple Beam Internal Structuring of PMMA", Proceedings of LPM2010 - the 11th International Symposium on Laser Precision Microfabrication, Stuttgart, Germany, June 2010

5. **D. Liu**, Z. Kuang, W. Perrie, P. J. Scully, A. Baum, S. Liang, A. Taranu, S. P. Edwardson, E. Fearon, G. Dearden, and K. G. Watkins, "Femtosecond laser internal structuring of materials using a spatial light modulator," PICALO 2010, Wuhan, China, March 2010

6. **D. Liu**, D. Karnakis, A. Kearsley, M. Knowles, Z. Kuang, W. Perrie, S. P. Edwardson, G. Dearden, and K. G. Watkins, "Ultrafast parallel laser processing of materials for high throughput manufacturing," LAMP2009 - the 5th International Congress on Laser Advanced Materials Processing, Kobe, Japan, June 2009

7. **D. Liu,** W. Perrie, S. P. Edwardson, M. Sharp, G. Dearden, and K. G. Watkins, "Refractive Index Modification using Femtosecond Lasers," Developments in Industrial Photonics, AILU, Daresbury Laboratory, June 2008

8. **D. Liu,** W. Perrie, S. P. Edwardson, M. Sharp, G. Dearden, and K. G. Watkins, "Femtosecond NUV Refractive Index Structuring in Optical Materials," Photon Northwest, May 2008

9. **D. Liu**, J. Cheng, W. Perrie, A. Baum, P. Scully, M. Sharp, S. P. Edwardson, Z. Kuang, N. G. Semaltianos, P. French, G. Dearden, L. Li, and K. G. Watkins, "Femtosecond laser micostructuring of materials in the NIR and UV regime," ICALEO 2007, USA

10. Z. Kuang, **D. Liu**, W. Perrie, J. Cheng, S. P. Edwardson, G. Dearden, and K. G. Watkins, "Fast parallel diffractive multi-beam laser surface micro-structuring," Proceedings of the 36th International MATADOR Conference, Manchester, UK, July 2010

11. O. J. Allegre, W. Perrie, K. Bauchert, **D. Liu**, S. P. Edwardson, G. Dearden and K. G. Watkins, "Real-time control of polarization in ultra-short pulse laser micro-processing," Proceedings of the 36th International MATADOR Conference, Manchester, UK, July 2010

12. Z. Kuang, **D. Liu**, W. Perrie, J. Cheng, S. Shang, S. P. Edwardson, E. Fearon, G. Dearden and K. G. Watkins, "Multiple beam ultrashort pulse laser microprocessing (Invited paper)," PICALO 2010, Wuhan, China, March 2010

13. A Dima, M. Gagliardi, **D. Liu**, W. Perrie, C. J. Williams, I. Rendina, G. Dearden, and K. G. Watkins, "Nano-Silicon Sol-Gel Film Refraction Index Modulation with Femtosecond Laser," EMRS Fall Meeting 2008

14. P. W. French, T. Li, J. Clowes, W. Perrie, M. Sharp, **D. Liu**, and K.G. Watkins, "Ultrafast Short Pulse Laser Material Processing of Aerospace Materials," Proceedings of the Fourth International WLT-Conference on Lasers in Manufacturing 2007, Munich, June 2007

Contents

List of figures

List of tables

List of symbols

Symbol	Unit	Description
E_b	eV	Bandgap energy
E_p	J	Pulse energy
f	mm	Focal length
F	J/cm^2	Fluence
G	n/a	Gain factor
I	W/cm^2	Intensity
k	n/a	Wave number
L	mm	Grating thickness
l_{fil}	μm	Filament length
n	n/a	Refractive index
n_2	cm^2/W	Nonlinear refractive index
NA	n/a	Numerical Aperture
P	W	Peak power
P_{cr}	W	Critical power
P_{th}	W	Threshold power
Q	n/a	Grating thickness parameter
s	mm/s	Scan speed
Δn	n/a	Refractive index change
$\Delta\lambda$	nm	Spectral bandwidth
ΔX	μm	Offset in X direction
ΔZ	μm	Offset in Z direction
$\Delta\theta$	°	Angular sensitivity of volume gratings
θ_b	°	Bragg angle
θ_i	°	Incident angle
θ_m	°	mth order diffractive angle
η	n/a	Diffraction efficiency
η_b	n/a	Diffraction efficiency at Bragg condition
λ	nm	Wavelength

Λ	μm	Grating period
τ	*fs / ps*	Pulse duration
φ	*n/a*	Phase of complex field
ϕ_C	°	Crystal orientation
ϕ_L	°	Input laser polarisation direction

List of abbreviations

BBO	beta-BaB_2O_4
COP	Cyclo-olefin polymer
CW	Continuous Wave
CGH	Computer Generated Hologram
DOE	Diffractive Optical Element
DOF	Depth of Focus
FBG	Fibre Bragg Grating
FTIR	Fourier Transform infrared Spectroscopy
FWHM	Full Width Half Maximum
GAA	Generalised Adaptive Additive
GL	Gratings and Lenses
GRENOUILLE	Grating-eliminated no-nonsense observation of ultrafast incident laser light e-fields
GS	Gerchberg-Saxon
GSW	Weighted Gerchberg-Saxon
HF	Hydrofluoric
ITO	Indium tin oxide
LC	Liquid Crystal
LCoS	Liquid Crystal on Silicon
MPA	Multiphoton Absorption
MPFL	Multiplexed Phase Fresnel Lenses
MOEMS	Micro-Opto-Electro-Mechanical System
MRAF	Mixed-Region Amplitude Freedom
NA	Numerical Aperture
NIR	Near Infrared
NUV	Near Ultra-violet
ORA	Optimal Rotation Angle
OLED	Organic Light Emitting Diodes
PC	polycarbonate

PDMS	polydimethylsiloxane
PI	polyimide
PMMA	poly(methyl methacrylate)
PMMI	poly-*N*-methyl methacrylimide
PMP	polymethylpentene
PRR	Pulse Repetition Rate
PS	polystyrene
SLM	Spatial Light Modulator
SVGA	Super Video Graphics Array, 800×600 pixels
WD	Working Distance
XGA	Extended Graphics Array, 1024×768 pixels

Chapter 1 - Introduction

1.1. Background and motivation

Femtosecond laser internal structuring of transparent materials presents unique abilities for localised refractive index modifications through nonlinear multiphoton absorption (MPA), thus allowing fabrication of various photonic devices with simplicity, flexibility and 3D capability. Bulk refractive index modification of polymeric materials, particularly poly(methyl methacrylate) (PMMA), is of current interest because of the potential of creating useful devices for clinical biological and chemical applications which can be integrated with lab-on chip micro-fluidic devices. However, with commercial kilohertz Ti:Sapphire femtosecond laser systems, the refractive index modification process requires only pulses with sub-microjoule level energy, whereas, mili-joule pulse energy is generally available, resulting in low throughput with a light utilisation factor of < 0.1%. In order to increase the throughput and efficiency, multi-beam parallel processing with a Spatial Light Modulator (SLM) is proposed and demonstrated.

An SLM is a remarkable optical device that can be used not only to correct wavefront aberrations, but also to split an energetic laser beam into many arbitrary diffracted spots in 2D and 3D. In fact, both of these abilities can be demonstrated simultaneously. By using an SLM addressed with appropriate Computer Generated Holograms (CGHs) to create a large number of diffracted beams of the requisite pulse energy, processing efficiency can be increased by more than an order of magnitude, reducing the fabrication time while allowing arbitrary parallel processing. The present study employs Liquid Crystal on Silicon (LCoS) SLM technology allowing nearly 20 uniform beam parallel writing inside PMMA.

Hence, throughput is increased by more than an order of magnitude, reducing the fabrication time by this factor while allowing arbitrary parallel processing. A novel technique for rapid fabrication of volume gratings is established by focussing on control of filament length, optimisation of multiple beam uniformity, and elimination of pulse front tilt effect which otherwise would lead to non-uniformity. Because parallel processing using an SLM also holds great promise beyond the field of fabricating volume gratings, it is a technology that creates new research fields and enables innovative applications.

Volume gratings which are considered as great spectral and angular selectors have been used in astronomical, spectroscopy and laser manufacturing areas: spectral beam combining of laser beams with shifted wavelengths, coupling elements in laser resonators, beam deflectors, splitters and attenuators. Using the flexible volume grating fabrication technique described in this research, a number of grating parameters such as angles of incidence, spectral or angular width, and central wavelength, can be adjusted. This technique is applicable to a wide range of transparent optical materials with a single-step process. However, the refractive index change is typically $< 10^{-3}$, requiring grating thickness of several millimetres for high Bragg efficiency. On the other hand, commercial volume gratings are created using a two-step process in dichromated gelatin (photosensitive polymer) using laser holography and chemical development. The refractive index change, however, can be very high ($> 10^{-2}$) so that the grating thickness is small, typically < 100 μm.

The main objectives of this thesis are:

1) to apply SLM generated multiple beams to femtosecond laser internal refractive index structuring of PMMA so as to improve throughput and processing speed.
2) to identify and study the effects of the key parameters that influence the process.
3) to develop a flexible writing technique for rapid fabrication of high quality photonic devices, particularly, volume Bragg gratings, with the fundamental NIR wavelength at 775 nm.
4) to improve the technique for processing with the second harmonic NUV wavelength at 387 nm.

1.2. Contributions of this thesis

This thesis is the first study to explore multi-beam parallel writing of high quality volume Bragg gratings inside transparent materials using an SLM. The approach offers great flexibility so that grating parameters, such as thickness and period, can be easily adjusted for specific applications.

A unique method of combining a thin nonlinear beta-BaB_2O_4 (BBO) crystal with the SLM to create multiple second harmonic beams opens up a new area of dynamic parallel processing at NUV wavelengths where nematic liquid crystal devices are more sensitive to optical damage. The volume gratings written with this technique demonstrates excellent optical quality and high stability.

In order to obtain high quality volume gratings, a series of optimisation techniques are adopted. Filaments that affect the axial length of refractive index modification are carefully controlled to maximise their length while avoid nonlinear self-focussing. Writing asymmetry due to pulse front tilt is also studied and eliminated. Furthermore, uniformity of multiple beams is improved greatly by breaking symmetry of the multiple spots pattern.

1.3. Overview of the thesis

The thesis consists of seven chapters. The current chapter is the main introduction of the proposed work. Chapter 2 commences with the introduction of relevant background about laser-matter ultrahigh intensity interaction inside transparent materials and mechanisms of refractive index modification (Section 2.2 and 2.3), followed by a review of lasers and materials employed by other researchers (Section 2.4 and 2.5). Common laser direct writing geometries and photonic devices fabricated by femtosecond laser pulses are demonstrated in Section 2.6. The effects of laser parameters, focussing conditions and materials on femtosecond laser internal structuring and refractive index change characterisation techniques are discussed in detail (Section 2.7 and 2.8). Finally, Section 2.9 presents the background of parallel processing and SLM technology, followed by a review of internal structuring using an SLM.

In Chapter 3, materials, equipment and experimental setups employed in this study are presented, followed by detailed descriptions of a series of

characterisation methods, including calculation of computer generated holograms (CGHs), diffraction efficiency measurements and other optical measuments.

Chapter 4 begins with experimental results and discussion of single laser beam direct writing including cotrol of filament length, elimilating pulse front tilt effect and fabricating optical components, followed by a demonstration of a series of refractive index structures generated by multiple laser beam direct writing.

Chapter 5 focusses on producing high quality volume gratings using multiple NIR beams generated by an SLM. Detailed optical analysis and theoretical modelling are also presented.

In Chapter 6, a novel technique for generating multiple NUV beams is described in detail. Analysis of the characteristics of the volume gratings produced using this technique is demonstrated.

Finally, Chapter 7 summaries the results and conclusions of the individual chapters, and suggests potential improvements and ideas for future work.

Chapter 2 - Literature review

2.1. Introduction

This chapter reviews the background literature in the topic of the research project. The basic theory and the mechanisms of internal structuring of materials by laser are presented, followed by an introduction to the commonly used laser systems and materials. The femtosecond laser internal structuring techniques, the effects of different process parameters and modified material characterisation methods will also be discussed. Finally, the parallel processing technique explored and its application to femtosecond laser based internal structuring will be described.

2.2. Laser-matter interaction inside transparent materials

Transparent materials usually have two distinct properties. First, their optical bandgaps are wide, with a range from 2.2 - 2.4 eV for chalcogenide glasses to 8.9 eV for fused silica. Second, their thermal conductivity, which is characterised by the thermal diffusion coefficient of typically ~ 10^{-7} m^2/s (~ 10^{-4} m^2/s for metal), is relatively low. These properties define the mode of the laser-material interactions that are discussed below.

When a transparent material is exposed by a femtosecond laser pulse with photon energy smaller than the material bandgap energy E_g, linear absorption cannot occur. At high intensities ($I > 10^{12}$ W/cm^2), nonlinear absorption of photons takes place via multiphoton [1] or tunnelling effects [2], followed by an avalanche mechanism [3] leading to strong ionisation.

In multiphoton ionisation, the number of photons, m, that is absorbed simultaneously to promote an electron from the valance band to the conduction band satisfies the relation $mhv > E_g$. As shown in Fig. 2.2-1, an electron in PMMA (bandgap E_g = 4.58 eV) needs to simultaneously absorb the energy from 3 photons at a wavelength λ = 775 nm or 2 photons at λ = 387 nm in order to be promoted to the conduction band. The ionisation rate, related to the probability for multiphoton absorption, also depends strongly on laser intensity [4].

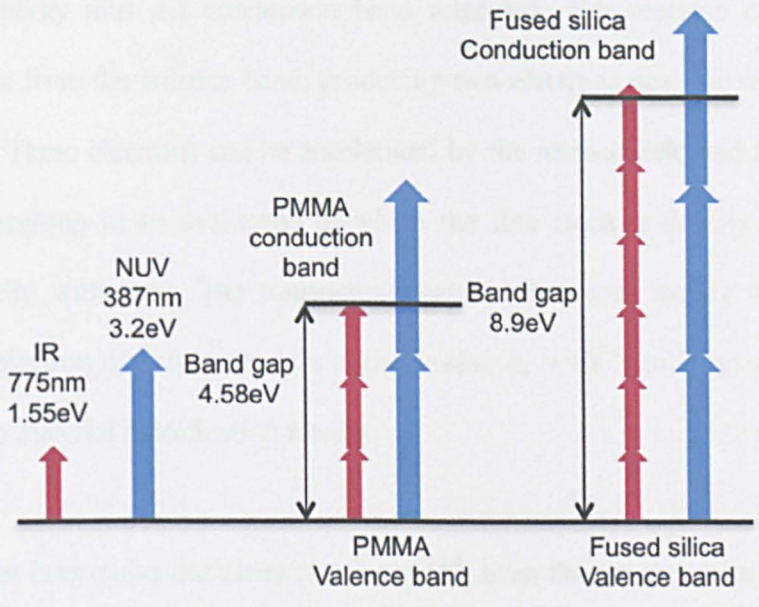

Fig. 2.2-2: Schematic of the multiphoton excitation of an electron in PMMA and fused silica from the valence to the conduction band.

In tunnelling ionisation, the strong electric field of the laser pulse reduces the Coulomb potential energy barrier and allows an electron to quantum mechanically tunnel from the valance band to the conduction band. The tunnelling ionisation rate is less dependent on the laser intensity. Although these two nonlinear

processes compete at ultra-high intensities, multiphoton ionisation generally dominates over tunnelling in femtosecond laser interaction with transparent materials.

In avalanche ionisation, electrons absorb laser energy through inverse Bremsstrahlung followed by impact ionisation. During inverse Bremsstrahlung, a free electron at the bottom of the conduction band is accelerated and moves to the higher energy states in the conduction band. When its total energy exceeds the bandgap energy plus the conduction band minimum, this electron can ionise another one from the valance band, producing two electrons near the conduction minimum. These electrons can be accelerated by the intense field and repeat the process, resulting in an avalanche in which the free electron density increases exponentially with time. The transparent material becomes locally absorbing, when the electron density exceeds a critical value $n_e \approx 10^{21}$ cm^{-3}, beyond which irreversible material modification results.

With longer laser pulse durations ($\tau > 1$ ps) [5], even though the pulse energy is quite high, the peak intensity is generally still too low to initiate the multiphoton process. Thus, avalanche ionisation is the only possible absorption mechanism. However, this process is unpredictable and chaotic.

In contrast, with a femtosecond laser pulse, the peak intensity is much higher, which leads to significant multiphoton ionisation. When the intensity exceeds a threshold value, unbound electrons are produced in the focal volume and act as

seeds for avalanche ionisation in a deterministic manner [5]. Hence, the energy deposition process and subsequent structural change are well controlled and highly reproducible, thus enabling precision material modification at a sub-micron scale.

2.3. Mechanisms of femtosecond laser internal structuring

Although the nonlinear absorption process of femtosecond laser pulses in transparent materials is well investigated, the physical mechanisms that induce refractive index changes in some materials are still not fully understood. With low laser pulse energy, there is a regime in which either reversible or irreversible refractive index modification can be achieved and the material retains good optical quality. With higher pulse energy, the material undergoes permanent structural changes, namely optical breakdown, such as the formation of microcracks and voids [6]. To explain such changes, several mechanisms have been proposed as detailed in the following paragraphs.

In polymeric materials, such as PMMA, a photochemical modification that involves a direct cleavage of the polymer backbone and propagation via chain unzipping under the formation of monomers has been reported [7]. Both positive [7, 8] and negative [9] refractive index changes can be obtained at the centre of the modified region, depending on the writing conditions.

In crystalline materials, such as quartz, a decrease in refractive index can be produced in the central modified region by femtosecond laser exposure. The reason for this is that the adjacent atoms in a crystal are initially in the closest possible positions, and any changes to the lattice will result in a lower atomic density. However, light-guiding effects have been observed in the nearby region where increased refractive index was induced by stresses [10, 11].

For fused silica, it is believed that femtosecond laser (1 kHz, 130 fs, 800 nm) induced densification due to rearrangement of the network of chemical bonds is responsible for the refractive index change [12]. When using a high repetition rate laser system (25 MHz, < 100 fs, 800 nm) to write refractive index structures in a borosilicate glass, heat accumulation with melting and subsequent resolidification is a possible mechanism [13]. However, Streltsov and Borrelli [14], who investigated both cases, argued that colour centre formation was the identified mechanism, and densification had only a small effect for the refractive index change. In short, it is difficult to disentangle the relative contributions of the mechanisms discussed above in practical cases. In fact, it is possible that all these mechanisms are involved in the process of the refractive index change.

2.4. Internal structuring using different lasers

Laser systems that have been utilised for modification of PMMA can be categorised into three groups: continuous wave (CW) light from broad band UV sources or He:Cd lasers; long pulses from excimer lasers; and ultrashort pulse femtosecond lasers.

2.4.1. Continuous wave UV lasers

During UV irradiation, single-photon absorption, where the photon energy is near the material bandgap energy, occurs and leads to refractive index change. In 1970, Tomlinson et al. [15] reported that refractive index increase of 3×10^{-3}, corresponding to a density increase by 0.8%, in PMMA generated by CW UV laser radiation (He:Cd, λ = 325 nm)was due to a crosslinking effect. A series of studies on wavelength sensitivity of PMMA indicates that there is no photodegradation for wavelength $\lambda > 340$ nm, while at 300 nm, maximum main chain scission is initiated by photoinduced side chain scission [16-18].

However, the limitations to UV laser modification are firstly that the process requires long developing times of about 200 hours [15, 19]; secondly the fabrication of 3D structures is constrained to within a region of < 1 mm below the interface due to the linear absorption of the transparent material [9].

2.4.2. Long pulse (ns) lasers

A number of experiments using ns lasers have been conducted with dye-doped PMMA material. Effective tuneable Fibre Bragg Gratings (FBGs) were inscribed in doped, single mode polymer optical fibre by excimer laser radiation, demonstrating a refractive index change of about 10^{-4} [20]. The holographically produced gratings, which showed self-development times of several weeks or required thermal fixing, were obtained in PMMA containing residual monomer and UV absorbing photoinitiator [21].

Material doping processes are usually complex and costly. In contrast, commercial or clinical grade, undoped PMMA materials are inexpensive and widely available. Several studies were conducted at excimer laser wavelength to produce refractive index changes in pure PMMA thin films [22-24]. A significant refractive index increase of ~ 0.5% at the readout wavelength of 632 nm and reduction in polymer film thickness were observed by Baker and Dyer [24] and the results explained in terms of photochemical modification and weak ablation of the polymer.

There are, however, drawbacks to ns laser modification. For doped materials, the linear absorption is higher, and so the fabrication depth is limited; whereas for undoped materials, higher exposures are required, so surface ablation is difficult to avoid.

2.4.3. Ultrashort pulse (fs) lasers

Compared with CW and ns laser modification, ultrashort pulse lasers operate at photon energies well below the material bandgap energy, allowing 3D processing via multiphoton absorption to a depth limited only by the working distance of the focussing element [9]. The distinct advantages of utilising ultrashort pulse lasers can be summarised as follows [25]. Firstly, since the energy of a single photon is below the bandgap energy, transparent materials cannot undergo linear absorption of ultrashort laser pulses. The induced structural changes are confined to the vicinity of the focal volume owing to nonlinear absorption. As a result, it is possible to fabricate geometrically complex structures in three dimensions.

Secondly, the multiphoton absorption process can be induced in any transparent dielectric, hence allowing fabrication of optical devices inside different materials. Thirdly, photonic integrated circuits can be produced by microfabrication of separate photonic devices and interconnections using ultrafast laser before or after assembly [25].

Thermal conductivity of dielectrics, which is characterised by the thermal diffusion coefficient, is usually relatively low at ~ 10^{-7} m^2/s, comparing to that of metals at ~ 10^{-4} m^2/s. A micron-sized exposed region will cool in ~ 10 μs ($\delta t \sim l^2/D \sim 10^{-5}$ s) [26]. Depending on whether the period between the pulses is longer or shorter than the time required for heat to diffuse away from the focal volume, femtosecond internal modification can be divided into three regimes: the low-frequency regime, in which material modification is induced by the individual pulses [27], the high-frequency regime, in which heat accumulation takes place [13, 28], and the intermediate regime, in which the heat diffusion time (τ_{heat}) is comparable to the inter-pulse period.

2.4.3.1. Low repetition rate regime – Amplified Ti:Sapphire systems

Amplified Ti:Sapphire lasers, which work at low repetition rates (1 - 200 kHz) are the most common laser systems for internal structuring of transparent materials [29]. At 1 kHz, high pulse energy of ~ 1 mJ is available, which provides the possibility of splitting a single beam to multiple beams using a spatial light modulator for parallel processing. Although the focussing of the energetic pulses can lead to asymmetric refractive index profiles (elliptical cross sections), which

are undesirable when writing waveguides, it is perfectly acceptable when producing volume gratings. However, these systems suffer from a number of drawbacks, such as, the processing speed is relatively low ($\leq$ 1 mm/s), the refractive index changes are relatively low ($\Delta n < 2\times10^{-3}$) [29], and the systems are complex and costly.

2.4.3.2. High repetition rate regime – Long-cavity Ti:Sapphire oscillators

Heat accumulation effects caused by high repetition rate ultrashort laser pulses can mitigate defect-induced damage and avoid collateral damage such as microcrack formation during laser material processing [30]. When a high repetition rate ultrafast laser is focussed and scanned transversely to the laser propagation direction, the formation of symmetric optical waveguides can be obtained as a result of isotropic heat diffusion out of the focal volume [28]. The writing speeds are relatively high at a few cm/s [29], compared with the low frequency systems.

There are shortcomings with the use of high frequency laser systems. Due to their low pulse energy (~ 100 nJ), high NA objectives are needed to focus laser beam tightly, which limits the working distance and depth for full 3D fabrication, Consequently, only a limited range of materials can be processed with such systems [31].

2.4.3.3. Intermediate regime – Ytterbium-based lasers

Ytterbium (Yb) - based lasers operating in an intermediate regime (~ 1 MHz) with a pulse period in the order of the heat diffusion time have the ability to modify materials with high speed and good quality. Usually, such systems consist of a bulk cavity-dumped oscillator [32, 33] and a fibre-based master oscillator/power amplifier system [27], and are able to produce pulses of < 300 fs at a fundamental NIR wavelength with MHz repetition rates and a few μJ pulse energy.

The major benefits of employing Yb-based lasers are that the systems are simple and cost effective without regenerative amplification stage, and a wide range of different materials can be processed. Furthermore, diode pumping allows the systems to be compact and efficient, which is important for industrial applications.

2.5. Internal structuring using different materials

2.5.1. Inorganic glasses

In 1996, the first demonstration of femtosecond laser (200 kHz, 120 fs, 810 nm) induced refractive index changes inside a variety of glasses was reported by Davis et al. [34]. Since then, a wide range of glass materials have been investigated, including amorphous fused silica [12, 27, 35-48], BK7 [40], quartz [10], sapphire [11, 49], Foturan glass [50-67], borosilicate glass [27, 68], some specially doped glasses [53, 56, 57, 69-76] and so on. Among these materials, fused silica is particularly attractive, owing to its excellent optical properties from UV through IR wavelengths and extraordinary chemical stability. Foturan glass has also

attracted great interest in the last few years. It is a photosensitive glass that can be modified by laser irradiation to create 3D microstructures for lab-on-chip and μ-TAS (micro-total analysis system) applications without the need for stacking or bonding procedures. The processing of Foturan glass involves three main steps: Firstly, 3D structures are written in a Foturan sample by focussed femtosecond laser pulses. Secondly, the sample is heated in a programmable furnace which leads to the formation of modified regions. Thirdly, the sample is etched in a 10% diluted solution of hydrofluoric (HF) acid in order to selectively remove the modified regions. As a result, the desired 3D hollow structure is formed [51].

2.5.2. Polymers

Compared with inorganic glass materials, optically transparent polymers have been widely used in various fields, ranging from microfluidics to Micro-Opto-Electro-Mechanical System (MOEMs), owing to numerous advantages including low cost, accessibility, light weight, flexibility, high transmission in the visible region and especially, processability due to the threshold fluence requirement being at least one order of magnitude lower than that for glass [25]. One approach to processing polymers is by femtosecond laser two-photon polymerization followed by post-exposure treatments, which allows the creation of micro- and nanostructures in various photoresists or polymer resins to be achieved [77-82].

Another technique investigated has been femtosecond laser direct writing within bulk polymers. Although a number of suitable polymer materials have been proposed (polymethylpentene (PMP), cyclo-olefin polymer (COP), polystyrene

(PS), poly-*N*-methyl methacrylimide (PMMI), polycarbonate (PC), polyimide (PI), polysiloxane, and polydimethylsiloxane (PDMS)) [83-88], it is PMMA that remains the most commonly studied material. A large variety of photonic devices have been created in PMMA including structures for optical data storage [77, 89, 90], 2D/3D gratings [7, 91-96], waveguides [8, 9, 97], photonic band gap structures[82, 98, 99], microfluidic structures/devices [100-103].

Second harmonic femtosecond laser (70 MHz, 200 fs, 385 nm) was first employed by Bityurin et al. [104] in 1999 to produce micro-sized structures within PMMA for optical storage. In this case, a combination of the fundamental and second harmonic wavelengths were used to minimise processing time. The mechanism of modification was described as bulk damage rather than refractive index modification, indicating that the process was operating above the ablation threshold of the material.

Since 2000, Scully and her group (including collaborators at the University of Liverpool) have conducted a series of studies on NIR (800 nm) and NUV (387 and 400 nm) femtosecond laser photomodification of PMMA with pulse durations between 40 and 200 fs [7, 91, 93-96, 105]. The work reported refractive index changes of the order 5×10^{-4} produced inside commercial grade bulk PMMA by an NIR femtosecond laser (1 kHz, 40 fs, 800 nm), thus demonstrating that efficient modification could be achieved without pre or post processing. Also, a refractive index change of 4×10^{-3} and cumulative modification behaviour were observed when using a NUV femtosecond laser (1 kHz, 180 fs, 387 nm).

Photodegradation of the polymer was investigated through polymer molecular weight distribution analysis, which revealed that the primary interaction mechanism was random main chain scission. While volatile analysis revealed that the monomer, MMA, was the sole reaction product. A Bragg diffraction efficiency of ~ 40% in the first order was measured when writing with a lens of focal length f = 75 mm, operating at 387 nm (NA < 0.03). At such low NA, self-focussing was significant, leading to non-uniform millimetre long filaments. All this work was carried out using single beam processing.

Li et al. created a small (50 μm diameter) volume phase grating holographically written inside bulk PMMA using a single femtosecond laser pulse (130 fs, 800 nm) [106]. The grating of thickness 100 μm and of period 1.5 μm was fabricated using a two-beam interference setup that recombined the two components focussed at an angle of 17°. The measured first order diffraction efficiency was approximately 0.8%, indicating that the refractive index change was ~ 2×10^{-4}.

2.6. Femtosecond laser internal structuring

2.6.1. Writing geometries

Two primary writing geometries have been widely utilised for femtosecond laser internal structuring. Those are longitudinal and transverse, in which the writing is carried out along and perpendicular to the beam propagation direction respectively [107]. These two geometries are illustrated in Fig. 2.6-1.

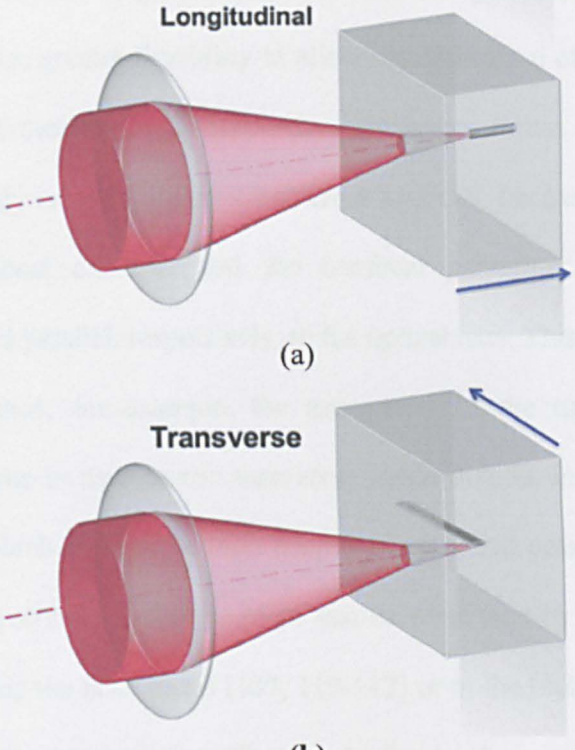

Fig.2.6-1: Writing geometries: (a) Longitudinal and (b) Transverse. The blue arrows denote the translation direction of the sample.

In the longitudinal geometry (Fig. 2.6-1(a)), the cross section of the modified region is inherently symmetric due to the rotational symmetry of the laser beam, and the transverse size of the region is determined by the focal spot size. However, the total dimension and structural complexity of this region are limited by the focal length of the objective [38, 108]. Since waveguides written in longitudinal geometry degrade with the focussing depth owing to spherical aberration generated at the air-dielectric interface, dynamic compensation synchronized with the writing procedure is required to obtain homogeneous longitudinal modification [19].

The transverse geometry (Fig. 2.6-1(b)) has attracted significantly more attention, because it provides greater flexibility in allowing fabrication of photonic devices with arbitrary dimension and complexity. However, it has the drawback of producing strongly asymmetric modified cross sections, because it is determined by the beam focal diameter and the confocal parameter in the direction perpendicular and parallel, respectively, to the optical axis. This is problematic for device performance; for example, the asymmetry of the transversely written waveguides results in asymmetric transverse mode distributions and waveguide birefringence, which can induce high coupling losses and polarisation dependent losses [109]. Nevertheless, this problem can be overcome in the low frequency regime by shaping the laser beam [107, 110-112] or in the high frequency regime by introducing heat accumulation effects to the focal volume [13, 28].

2.6.2. Femtosecond laser fabrication of photonic devices

The ability to modify refractive index inside transparent materials using femtosecond laser pulses can be employed to fabricate a wide range of microstructures including volume gratings [67, 87, 94, 96, 113-117] and waveguides [9, 14, 25, 29, 34, 35, 38, 107, 111]. In this section, the approaches taken to fabricate these two types of device are discussed in detail.

2.6.2.1. Volume phase gratings

Volume phase gratings are usually recorded holographically in a photosensitive volume medium, producing periodic variations of the varying refractive index ($n = n_0 + \Delta n\cos\varphi$). These volume gratings, available commercially, can theoretically

have peak diffraction efficiency approaching 100%, if the Bragg condition $2\Lambda\sin\theta_b = m\lambda$ (where Λ is the period of the volume grating, λ is the wavelength of incident light, θ_b is the Bragg angle and m is the diffraction order) is satisfied. Under this condition, any change with respect to the incidence angle or wavelength results in a significant decrease of the diffraction efficiency. Therefore, volume gratings are considered as perfect spectral and angular selectors that have been used in applications such as spectral beam combining of laser beams with shifted wavelengths, coupling elements in laser resonators, beam deflectors, splitters and attenuators. By changing the thickness, period or orientation of the grating vector of volume gratings, a number of grating parameters can be adjusted, including angles of incidence, spectral or angular width, and central wavelength.

Volume gratings demonstrate many advantages over other types of gratings. Thin gratings operating in the Raman-Nath regime show broad angular and spectral bands, while volume gratings operating in the Bragg regime have high angular and spectral selectivity and can diffract most of the power into one diffractive order. Volume gratings are also less dependent on the polarisation state of the input light. By adjusting the grating design, volume gratings can be tuned to shift the diffraction efficiency peak to a desired wavelength, and to direct the diffracted energy into higher diffractive orders. Ghosting and scattering from volume gratings are significantly reduced compared to surface gratings. On the other hand, the negative aspects of volume gratings are: the requirement for high line density, the wavelength and angular bandwidths of the volume gratings are quite

narrow; and the difficulty in fabricating volume gratings that can generate diffraction orders higher than $m = 10$ [118].

Traditional method of producing volume gratings

Usually volume gratings with thicknesses from a few to over a hundred microns are recorded holographically, by the interference of two laser beams, in photosensitive media such as dichromated gelatin, photopolymers, photorefractive crystals, and inorganic photosensitive glasses [119]. Although it is a well-established process, it still has a few drawbacks. First, active phase stabilisation system is employed so as to avoid phase changes between the two writing beams during the recording, which makes the process more complicated. Second, the process is slow, as the response time during recording is long. Third, most oxide photorefractive crystals are sensitive to a range of wavelengths, even with low intensity light, which limits their use as devices. Fourth, volume gratings recorded at room temperature in photorefractive crystals have a limited lifetime, thus a thermal fixing technique is required. It is still difficult to achieve true permanent changes through this technique [67]. Finally, each volume holographic grating is a master – while in surface gratings, reproduction from the master produces many copies thus reducing costs

Femtosecond laser direct writing using a single beam

In recent years, volume gratings in non-photorefractive optical materials such as fused silica [42, 120, 121], PMMA [7, 93, 94, 116, 122] and Foturan glass [67] have been produced using femtosecond laser direct writing with a single beam. This technique is simple to implement and can provide total flexibility in 3D.

Furthermore, the total thickness of the volume gratings can be controlled through a layer-by-layer stacking process, and their periodic spacing can also be adjusted easily. Permanent volume gratings can be generated in these non-photorefractive materials that have excellent stability. However, the throughput of this approach is low so that its scaling to high throughput processing is severely limited. Yamada et al. [121] reported that the fabrication of volume gratings induced by the self-trapped long 'filament' of the femtosecond laser pulses in silica glass. By changing the NA of the focussing lens (hence varying the filament length) and stacking multiple layers periodically, the grating thickness could be adjusted. A volume grating generated with a period of 3 μm and a thickness of 150 μm demonstrated a maximum diffraction efficiency of 74.8%. However, this method took 5 to 9 hours to fabricate a grating with dimension of 300 × 300 μm^2.

One approach to rapid fabrication of volume phase gratings in Foturan glass employed a line focus (2 μm × 1800 μm) generated by cylindrical lenses with energetic 80 μJ, 40 fs, 800 nm pulses at 1 kHz repetition rate. However, the modification achieved was quite non-uniform due to filamentation during exposure, and the process also required a post baking procedure for the grating to be properly formed [67].

Femtosecond laser writing using two-beam interference

Femtosecond laser writing of gratings inside transparent materials by interfering two beams at the focal point has been reported by several authors [91, 113, 123]. In 2000, Kawamura et al. [123] demonstrated permanent gratings written inside

diamond. The experimental setup in this case was rather complex. The laser beam from a femtosecond laser (10 Hz, 180 fs, 800 nm) was split into two beams, and focussed by two lenses at an angle of 10° – 30° to each other. One beam was directed through a delay line so as to adjust the relative timing of the pulses to achieve temporal overlap. The method produced a grating with a period of ~ 2.5 μm and a diffraction efficiency of ~ 20%. However, the drawback of this approach was the technical difficulty in precisely adjusting the two focussing lenses simultaneously to overlap the beams spatially inside the sample. Furthermore, changing the grating period required adjustment of the angle between the two beams, which could only be accomplished by major realignment of the entire optical system. Using a similar setup, Zhai et al. [113] produced holographic gratings both on the surface and inside an azo-dye-doped polymer bulk with femtosecond laser (1 kHz, 150 fs, 800 nm). An impressive diffraction efficiency of up to 76% at the first Bragg order was obtained.

Baum et al. [91] employed a less complex experimental setup, as shown in Fig. 2.6-2(a), which consisted of a phase mask that split the incoming beam into two, in conjunction with a bi-prism to produce two parallel beams and a focussing lens to overlap the beams at focal point. A grating with a period of 1.4 μm (see Fig. 2.6-2) was generated inside pure PMMA material at a depth of 100 μm using NUV femtosecond laser pulses (1 kHz, 180 fs, 387 nm). A diffraction efficiency of ~ 10% was measured with a 633nm readout beam. It was concluded that the relatively low efficiency was due to the limited thickness of the grating. The advantage of this method is the grating period can be easily adjusted by changing

the separation between the phase mask and the bi-prism. The drawbacks are that due to very small focal spots, the alignment for spatially overlapping the two beams is critical, the processing speed is restricted and the modification depth is limited.

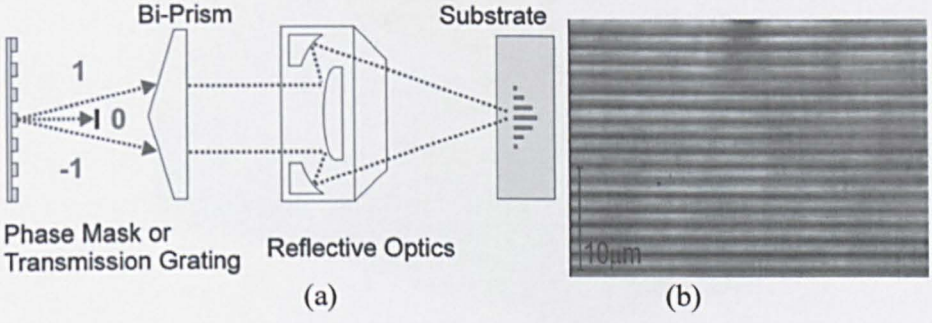

Fig. 3.6-2: (a) Holographic writing setup consisting of a phase mask, a bi-prism and a Schwarzschild objective; (b) A grating written holographically inside PMMA (Λ = 1.4 μm, s = 2 mm/s, 0.12 mJ/cm^2, NA = 0.15). [91]

Recently, Voigtlander et al. [124] employed a simple setup for volume Bragg gratings fabrication in fused silica using a cylindrical lens and a phase mask, as shown in Fig. 2.6-3. A line focus (6.1 μm × 4.8 mm) was employed to provide a large number of interference fringes, hence increasing fabrication speed. A volume grating with a period of 1.075 μm was produced by stacking multiple modified layers. Transmission and diffraction analysis revealed a refractive index Δn of 4 × 10^{-3}. A potential application as wavelength-specific reflectors was proposed. The advantages of this technique include simple experimental setup and relatively fast processing speed compared to the methods reviewed above. The shortcoming is that the grating period cannot be changed.

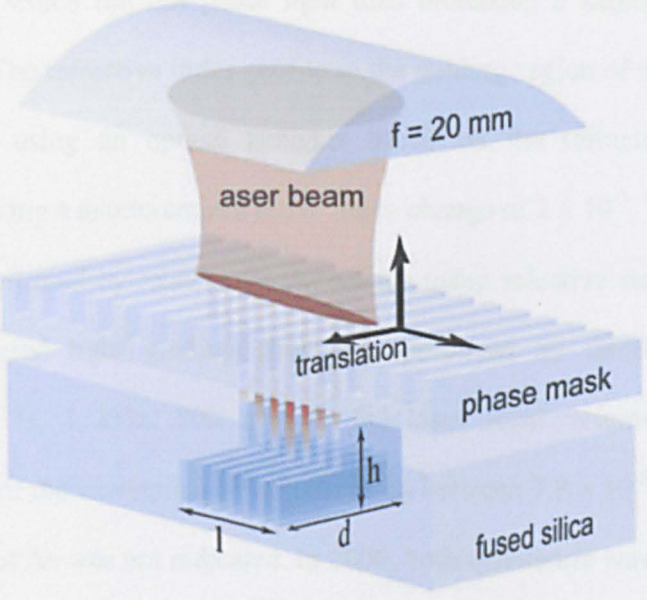

Fig. 2.6-3: Schematic of volume Bragg gratings written in fused silica using a cylindrical lens and a phase mask. [124]

In general, writing with two-beam interference enables the fabrication of the fine-pitched grating structures (sub-micron) at a relatively high speed thanks to the interference fringes at the focal spot. However, the intensities of the interference fringes are modulated by the Gaussian beam profile and the modifications are limited only to periodic grating structures.

2.6.2.2. Waveguides

Femtosecond laser direct writing of waveguides in PMMA has attracted strong interest. In 2004, waveguides were produced by Zoubir et al. [9] in bulk commercial grade PMMA with a longitudinal setup (30 fs, 25 MHz, 800 nm).The refractive index modulation had a depressed tubular structure surrounding the

central region, which did not guide light thus indicating a negative refractive index change. The refractive index profile in the guiding region of the waveguide was measured using an optical analyser based on the refractive near-field technique, showing a maximum refractive index change of 2×10^{-3}. The measured profile was confirmed by relative measurements using selective etching. Ohta et al. [125] reported light guiding structures, produced by femtosecond laser radiation (100 fs, 1 kHz, 800 nm) in the laser focal volume in PMMA. Measurements of the waveguide NA revealed Δn between 7.8×10^{-5} and 1.5×10^{-4}, while the sign of Δn was not indicated. In 2006, both symmetric waveguides and a directional coupler in PMMA were produced by femtosecond laser (85 fs, 1 kHz, 800 nm) irradiation with a transverse setup in conjunction with a slit beam shaping technique [8]. The single-mode guiding structures had a positive refractive index change of 4.6×10^{-4}, attributed to the scission of polymer chains causing volume contraction.

2.7. Effect of different parameters on femtosecond laser internal structuring

Femtosecond laser induced refractive index modification has been shown to be not only dependent on a range of laser parameters such as pulse energy [93, 126], pulses duration [39, 93], wavelength [94], scan speed [127], repetition rate [27, 43], polarisation [128, 129], and number of overscans [94]. It also relies on focussing conditions including NA and focussing depth from the interface. Furthermore, material properties e.g. structure [130] and composition [131] can also affect the modification process.

2.7.1. Effect of laser parameters

2.7.1.1. Effect of pulse duration, pulse energy, wavelength and number of overscans

For fluences below the ablation threshold, femtosecond laser pulses can induce permanent material refractive index changes or absorb through accumulation in the case of multiple-pulse irradiation. An incubation effect occurs for weakly absorbing materials, which can increase absorptivity and lower the damage threshold compared with single-pulse irradiation [132].

In fused silica, Guo et al. [39] conducted a detailed analysis on the effects of pulse duration on refractive index change. Femtosecond laser pulses (1 kHz, 800 nm, 130 – 500 fs) were focussed by a 0.08 NA objective into the samples. As demonstrated in Fig. 2.7-1(a), a decrease in bulk damage threshold and an increase in refractive index change threshold with increasing pulse duration between 130 and 230 fs were observed when using repetitive irradiation with sub-ablation threshold fluences. Also, no refractive index change could be obtained when the pulse duration was longer than 230 fs. The triangular Region 2 in Fig. 2.7-1(a) indicates the process window for refractive index modulation under this focal condition. Within this region, at fixed pulse energy, shorter pulse durations induced higher refractive index change and the refractive index change increased with increasing pulse energy (see Fig. 2.7-1(b)). Further investigation revealed that both the refractive index change and the breakdown filament length decreased when the pulse duration was increased, indicating the strong dependence of the filament length on the pulse duration (see Fig. 2.7-1(c)). [39]

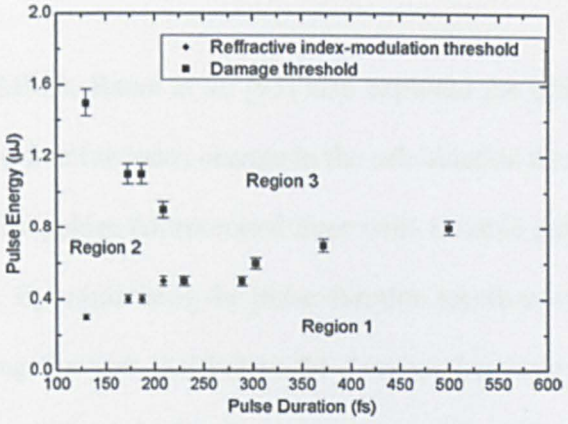

(a)

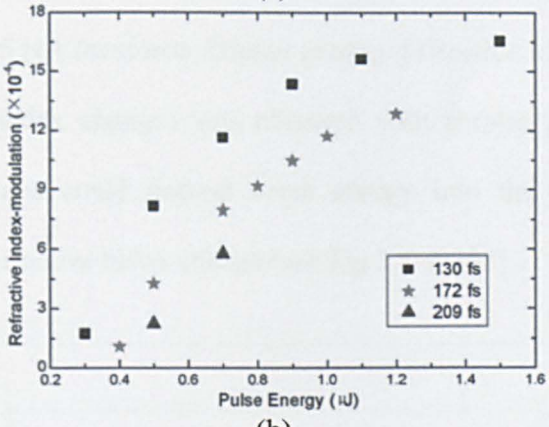

(b)

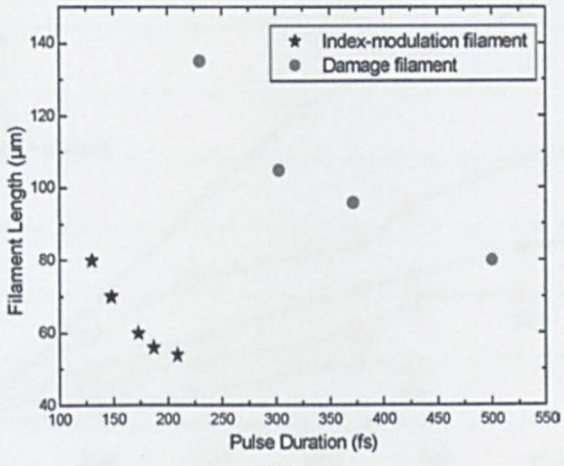

(c)

Fig 2.7-1: (a) Effects of the pulse duration on the refractive index change threshold and the breakdown threshold with scan speed of 10 μm/s. (b) Effects of the pulse energy on the refractive index change at the different pulse duration. (c) Effects of the pulse duration on the filament length at the pulse energy of 5 μJ (star) and 12 μJ (round). [39]

For the case of PMMA, Baum et al. [93] also explored the effect of variation in pulse duration on refractive index change in the sub-ablation threshold regime. An 800 nm, 1 kHz Ti:sapphire femtosecond laser with variable pulse duration down to 40 fs was used. By minimising the pulse duration together with a high number of over scans using fluences just below the damage threshold provided optimal refractive index modification. Gratings with a period of 40 μm were directly written using a 0.15 NA focal lens. Higher grating diffraction efficiency (inferring higher refractive index change) was obtained with shorter pulse duration. In addition, more scans could deposit more energy into the local area, hence produced higher refractive index change (see Fig 2.7-2) [93].

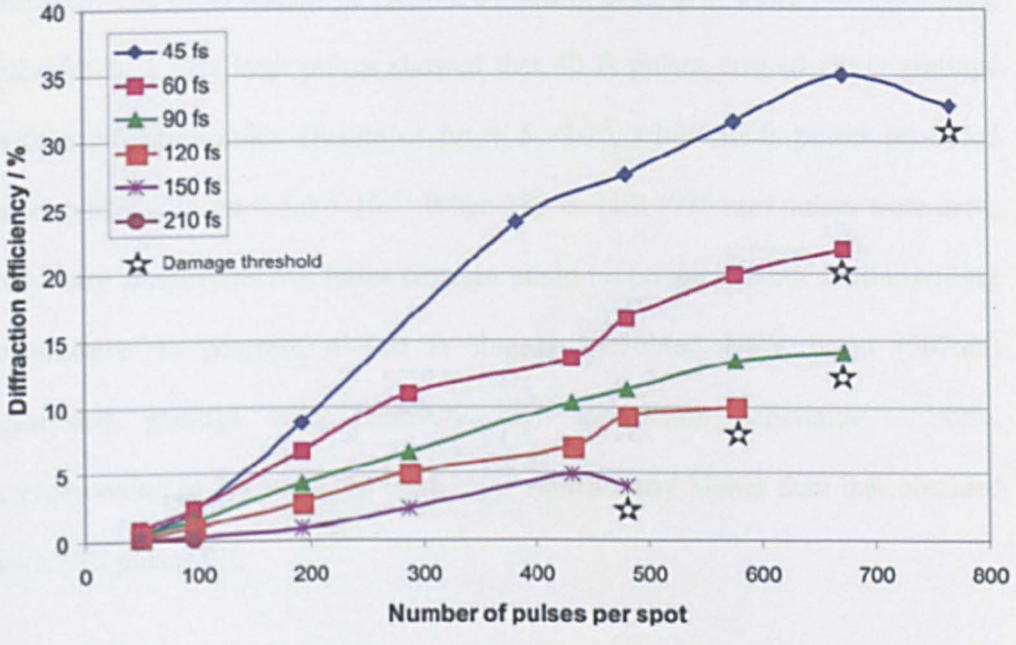

Fig. 2.7-2: Dependence of grating diffraction efficiency on pulse duration and number of pulses per spot (converted from number of overscans) for a fluence of 0.14 J/cm^2. [93]

A decrease of the bulk damage threshold with increasing pulse duration was also observed [93]. All these findings are consistent with the results shown in Fig 2.7-1(b). Therefore, it was concluded that a higher number of low energy pulses with shorter pulse duration could provide higher refractive index change, revealing a means of controlling photomodification via the incubation process and thus controlling avalanche ionisation.

In pure PMMA, which has a bandgap energy of 4.58 eV [7], three simultaneously absorbed photons at 800 nm ($h\nu$= 1.55 eV) can provide sufficient energy to excite electron transitions, whereas two photons cannot (see Fig 2.1-1). However, at 387 nm, a single photon has 3.2 eV, and the energy of two photons is above the bandgap. The modification of PMMA by Scully et al. [94] using NIR (800 nm), sub-100 fs, 1 kHz laser pulses showed that 40 fs pulses created phase gratings with a refractive index change of $\Delta n = 5 \times 10^{-4}$, while 85 fs pulses produced waveguides with $\Delta n = 4.6 \times 10^{-4}$. When 180 fs, NIR (775 nm) pulses were used, only very small refractive index changes could be produced with similar writing parameters. In contrast, a 180 fs frequency-doubled NUV beam (387nm) generated gratings with relatively high diffraction efficiency ~ 40%, corresponding to $\Delta n = 4 \times 10^{-3}$, which is significantly higher than that obtained with NIR pulses [7].

2.7.1.2. Effect of pulse repetition rate (PRR)

High PRR femtosecond laser systems usually induce heat accumulation effects, because the laser pulse interval is shorter than the heat diffusion time of dielectric

materials, as discussed in Section 2.4.3. As a result, in PMMA heat accumulation can result in thermal expansion at the focal point [9]. A waveguide with an expanded core and a depressed tubular structure therefore resulted when using 20 nJ pulses at 25 MHz and 800 nm in longitudinal writing geometry. Here, the core was found to exhibit a negative refractive index change, while the surrounding area could guide light indicating a positive refractive index change. For glass materials, high repetition rate pulses can lead to isotropic heat diffusion out of the focal volume. Waveguides with symmetric cross-sections were obtained with 100 nJ laser pulses at 4 MHz, 800 nm and 80 fs in transverse writing geometry [28]. Because of the different mechanism involved, the refractive index change within the waveguides created was found to be positive. Generally, the processing speed using high PRR lasers is much faster.

Low repetition rate pulses have negligible thermal effect, and usually generate positive refractive index changes in both polymer and glass materials. With transverse writing setup, the induced structures had asymmetric cross sections [109]. The processing speed in this case was somewhat restricted.

2.7.1.3. Effect of polarisation direction

Effects of incident laser polarisation states on the refractive index change in silica glass have been investigated by Yamada et al. [133-135]. The refractive index changes were produced by filaments formed by femtosecond laser pulses (1 kHz, 130 fs, 800 nm) with linear (x-polarised or y-polarised) and circular polarisation (see Fig. 2.7-3). The substrate was held stationary with the laser beam propagated

along z-axis and focussed by a lens with 0.036 NA and f = 80 mm. After 5 min exposure with 1 μJ pulses, 200-μm-long, refractive index change regions were generated, as illustrated in Fig. 2.7-3. The results suggested that there were differences between the refractive index changes induced by x-polarised and y-polarised laser pulses. Further investigation revealed that the cross sections those regions modified with linear polarisation were elliptical (ellipticity = 0.85) with long axes parallel to the polarisation direction, as illustrated in Fig. 2.7-4(a) and (b).Whereas, the cross section produced with circular polarisation was more round (ellipticity = 0.93) (see Fig. 2.7-4(c)). [135]

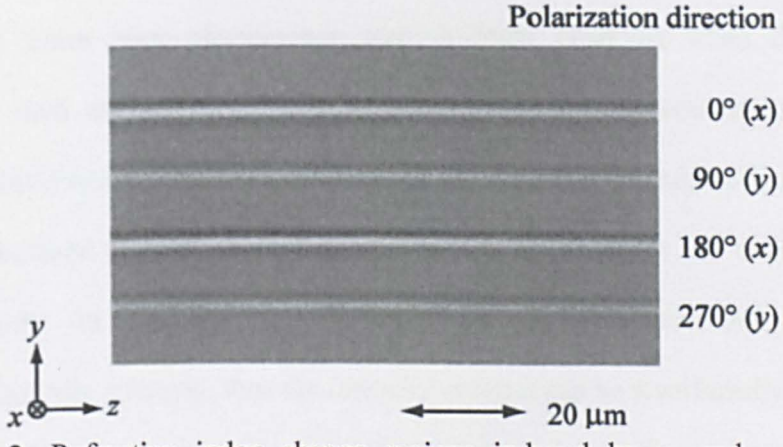

Fig. 2.7-3: Refractive index change regions induced by *x*- and *y*-polarized pulses.[135]

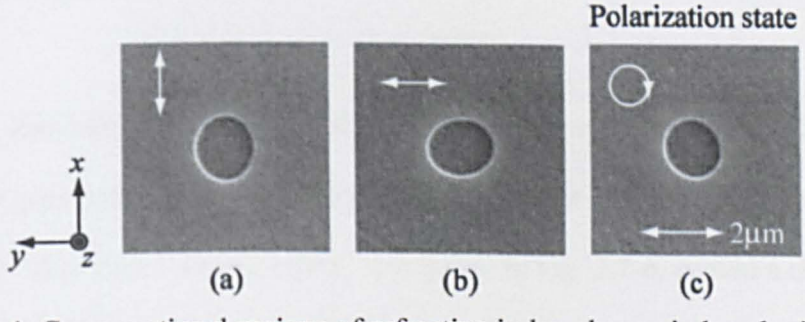

Fig. 2.7-4: Cross-sectional regions of refractive index change induced with (a) *x*-polarisation, (b)*y*-polarisation, and (c) circularly polarisation.[135]

The dependence of the optical transmission properties of waveguides on the polarisation states of the writing beam (1 kHz, 120 fs, 800 nm) was also evaluated [136]. The transmission through waveguides written in fused silica using circularly polarised light was found to be higher than that using linearly polarised radiation.

2.7.1.4. Effect of scan direction and pulse front tilt

Pulse front tilt, or a spatiotemporal distortion across the pulse front, is an ultrashort pulse laser phenomenon that is often observed when dispersive elements such as gratings or prisms are used in typical stretcher-compressor ultrafast laser systems [137]. The distortions that change the pulse characteristics on propagation can be due to even slight misalignments of stretchers or compressors. In the focal region, pulses with such distortions will be spatiotemporally enlarged, thus the intensity at focus can be significantly less than that of the pulses without distortions [138]. There are two sources of pulse front tilt: angular dispersion (see Fig. 2.7-5(a)) and combination of spatial and temporal chirp (See Fig. 2.7-5(b)) [137].

In 2008, Kazansky et al. [139] proposed that pulse-front tilt should be considered as a new parameter that can have an effect on internal structuring of transparent materials. The "quill" writing effect, as depicted in Fig. 2.7-6, caused a change in material modification when writing in the reverse direction. It was explained as a

consequence of anisotropic electron plasma trapping by a tilted pulse front along the writing direction.

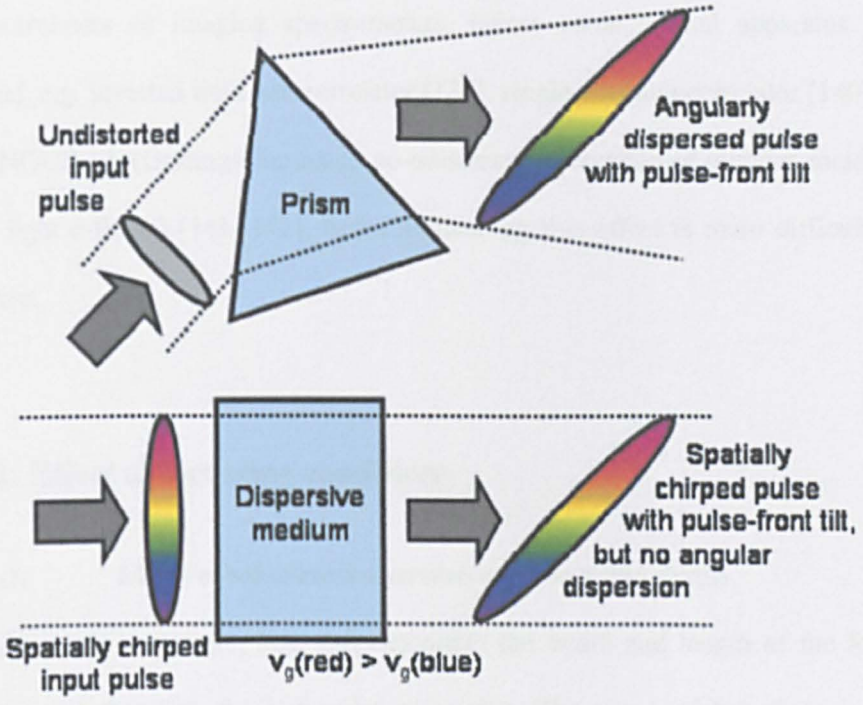

Fig. 2.7-5: Two sources of pulse-front tilt. (a) Angular dispersion. (b) Combination of spatial and temporal chirp [137].

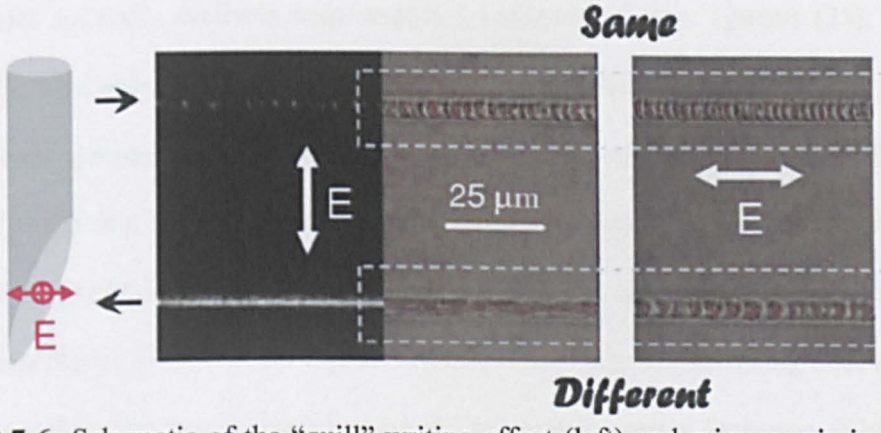

Fig. 2.7-6: Schematic of the "quill" writing effect (left) and microscopic images showing different modified structures when writing in the opposite directions (right). [139]

Pulse front tilt is not easily monitored with standard diagnostic equipment such as autocorrelators or imaging spectrometers, unless some special apparatus are utilised, e.g. inverted field autocorrelator [138], single-shot autocorrelator [140] or GRENOUILLE (Grating-eliminated no-nonsense observation of ultrafast incident laser light e-fields) [141, 142], hence controlling this effect is more difficult in practice.

2.7.2. Effect of focussing conditions

2.7.2.1. Effect of numerical aperture and focussing depth

The focussing parameter, NA, can determine the width and length of the focal volume and therefore the induced feature size. The range of NA that can be utilised is restricted, because theoretically NAs of > 0.002 are required to achieve a high enough threshold intensity for internal structuring with the mJ level pulse energies generally available with amplified femtosecond laser systems [25]. In reality, the minimum NA required is significantly higher than that, due to two nonlinear processes, self-focussing and white-light continuum (see Section 2.7.2.2). At low NAs, the feature size is no longer determined by the external focussing, but is affected by the nonlinear processes which are difficult to control and reproduce [143-145] (see Fig. 2.7-7). For NAs > 0.6, self-focussing does not occur and feature size is dependent on the external focussing. However, if high PRR laser systems are employed, the heat accumulation effects can significantly enlarge the feature size, e.g. a focal spot of 0.5 μm has created spherical features

0.5 μm has created spherical features up to 50 μm in diameter [13]. Usually, at LRR regime and below a NA of 0.6, the induced structures are asymmetric and elongated along the optical axis; above this value, the structures are nearly spherically symmetric [25].

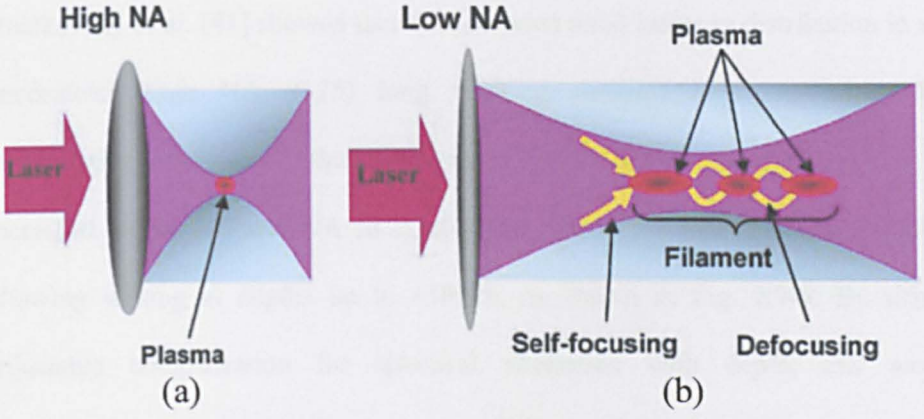

Fig. 2.7-7: Schematic of the damage processes induced by (a) external focussing and (b) internal self-focussing. [146]

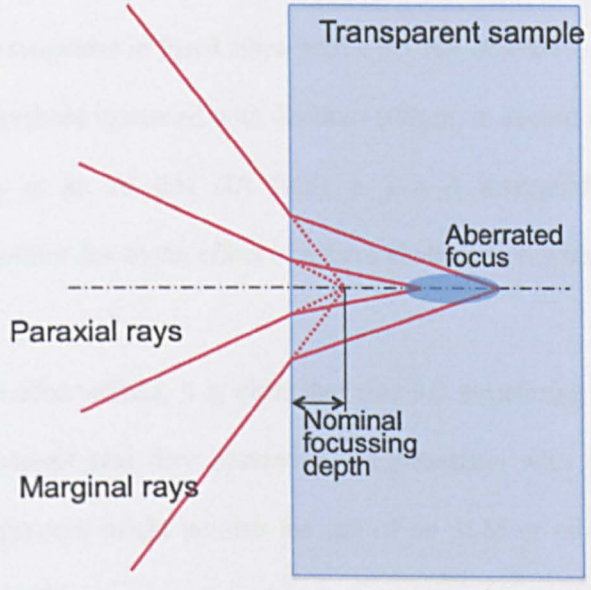

Fig. 2.7-8: Focussing through an air/dielectric interface with a high NA objective. (Marginal rays focus at a different depth than paraxial rays, which elongates the focal spot, thus inducing a spherical aberration).

Internal femtosecond laser structuring for 3D micromachining is complicated by the air/dielectric interface, which introduces depth dependent spherical aberration, as shown in Fig. 2.7-8, with increasing NA, as studied primarily in fused silica [41, 147]. This results in higher modification thresholds with increasing depth. Hnatkovsky et al. [41] showed that the aberrated axial intensity distribution in an uncorrected high NA (0.75) long working distance objective limits the modification depth to < 40μm from the interface unless the pulse energy is increased, while at lower NA (0.2), spherical aberration was almost negligible, allowing writing at depths up to ~10mm, as shown in Fig. 2.7-9. By using adjustable compensation for spherical aberration with depth, this work demonstrated uniform modifications using 800 nm, 100 fs, 100 kHz pulses at 0.75 NA up to ~ 1 mm from the interface with structures limited axially to < 4 μm. Liu et al. [147] also showed that the influence of focussing depth was significant when writing waveguides in fused silica with a 0.5 NA objective, showing that the modification threshold increased with depths >300μm, in accord with calculations by Hnatkovsky et al. At this NA (0.5), a 3 × 3 waveguide array showed asymmetric coupling due to the effect of spherical aberration with depth.

Based on these observations, it is clear that true 3D structuring in bulk material will require dynamic real time aberration compensation with depth during 3D writing. One approach might involve the use of an SLM or other beam shaping technique [148, 149].

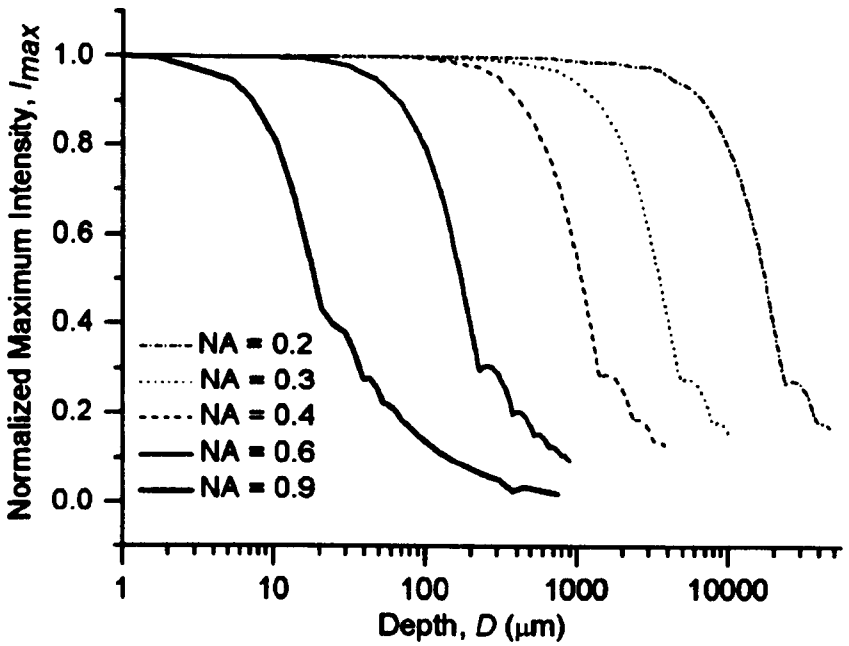

Fig. 2.7-9: Calculated maximum axial intensity I_{max} as a function of focussing depth for different NAs in fused silica. [41]

2.7.2.2. Filamentation and self-focussing

The ultrahigh intensity associated with femtosecond pulses leads naturally to non-linear interaction in dielectrics hence inducing an intensity related component to the refractive index. Filamentation or self-guiding occurs when Kerr self-focussing is dynamically balanced by de-focussing due to the electron plasma initiated by multi-photon absorption. The control of filament length (and hence modification length) is sensitive to pulse energy, wavelength, pulse duration and in particular, the effective NA. Much of the previous research on filamentation or self-guiding at ultrahigh intensity has been carried out on fused silica [127, 150, 151]. For example, Saliminia et al. [127] analysed the interplay between self-focussing and filamentation with 810 nm, 45 fs, 1 kHz laser pulses in fused silica

for 0.03 < NA < 0.85. Sufficiently high pulse energies always resulted in refractive index modifications ahead of the geometrical focus, accompanied by irregular voids due to optical breakdown. At low NA, while carefully controlling pulse energy and pulse number, refractive index structures with modification lengths up to ~ 2 mm were demonstrated with periodic structuring due to self-focussing (see Fig. 2.7-10). As the pulse energy was increased, the modified regions moved towards the laser source, away from the geometrical focus; while, as the NA was increased, the modification length reduced to < 20 μm. Peak powers were always well above the critical power for self-focussing (P_c of few MW) in fused silica.

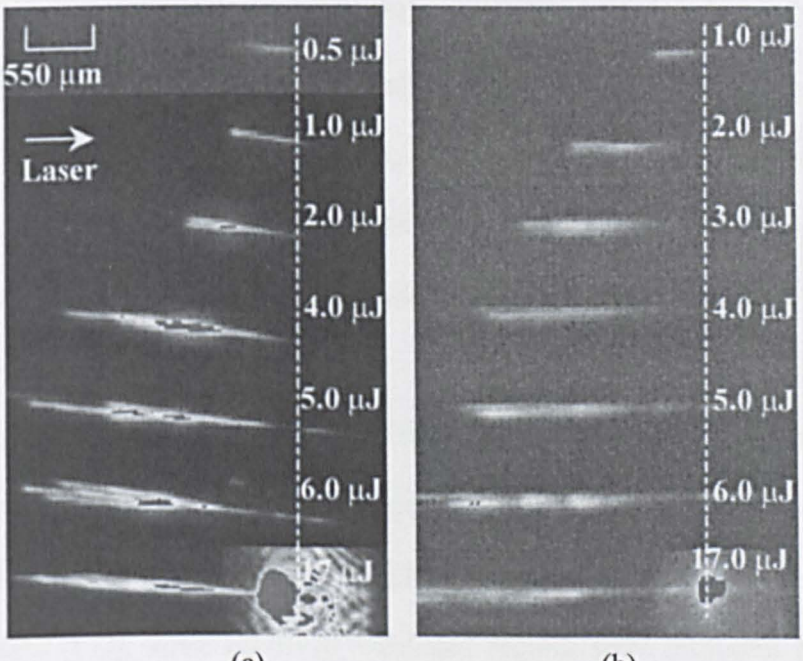

(a) (b)

Fig. 2.7-10: CCD images of the accumulated laser scattering and plasma fluorescence signals at different pulse energies. An objective lens with 0.03 NA (f = 73.5 mm) was used to focus the beam inside the glass. The sample was irradiated by roughly (a) 10,000 shots and (b) 10 shots. The dotted lines represent the geometrical focal positions. [127]

More recently, self-focussing has been studied in PMMA by Uppal et al [97, 152]. For example, 3D waveguides were created in PMMA and the study demonstrated the effect of NA on the ability to create 15 mm long waveguides (longitudinal writing) using 150 fs, 800 nm, 1 kHz laser pulses as well as the effect of pulse energy and writing speed.

At low NA (~ 0.1) and with pulse energies < 2 μJ, self-focussing and self-guiding lead to long modification length and waveguides were found to be sensitive to polymer degradation and void formation. As the critical power for self-focussing was only ~ 23 kW in the case of PMMA ($n_2 \approx 2.7 \times 10^{-14}$ cm^2/W [80]), peak powers used were orders or magnitude above this value. Tight focussing using a 0.4 NA objective combined with pulse energies from 0.1 - 1.5 μJ improved waveguide fabrication significantly, limiting modified depths from 20 - 250μm and allowing the creation of 3D waveguide splitters at 0.1 μJ pulse energy.

Watanabe recently studied femtosecond filamentary modification of PMMA with 100 fs, 800 nm, 1 kHz laser pulses and a low NA (0.1) objective with the radiation focussed to ~ 1.5 mm below the sample surface while translating the sample transversely [152]. After exposure, irradiated regions were inspected under an optical microscope. Pulse energies from 0.8-1.6 μJ produced modified refractive index regions from 210-420 μm in length with scattering damage observed above 1.7 μJ in agreement with Uppal et al [97]. The head of the modified regions elongated towards the laser source as the pulse energy was increased, a

characteristic of filamentation in dielectrics. In addition, the authors simultaneously studied the spectral broadening of the laser pulse during irradiation, showing that the super-continuum broadens with increasing pulse energy.

Filamentation extends the modification in dielectrics well beyond the Rayleigh length, but clearly may not necessarily guarantee uniform modification throughout a material due to the complex non-linear interactions, which makes exact balancing of the self-focussing with plasma de-focussing difficult.

2.7.3. Effect of materials

Material compositions and structures caused large differences in femtosecond laser induced refractive index change in various glasses, as studied by Ehrt et al. [131]. In particular, in fluoride phosphate glasses, the induced refractive change increased with increasing phosphate content up to 5×10^{-3}.

Yang et al. [130] observed a very rare and material dependent effect, which was non-reciprocal ultrafast laser writing (150 fs, 800 nm, 250 kHz) in a homogeneous medium, z-cut $LiNbO_3$ crystal, induced by a tightly focussed ultrafast laser beam. They concluded that the effect was due to light pressure, photon drag effect and the associated light-induced thermal current in crystalline media.

2.8. Characterisation of refractive index change

2.8.1. Positive or negative refractive index change

The sign of the refractive index change induced by femtosecond laser is relevant for waveguides fabrication, because it determines whether the light guiding occurs in the core or in the surrounding area. On the other hand, for grating fabrication, the absolute value of the refractive index change is more important.

For internal structuring of PMMA, the sign of the refractive index change is dependent on the repetition rate of the laser pulses. Using a high repetition rate femtosecond oscillator (25 MHz, 30 fs, 800 nm), a negative refractive index change was obtained in the focal volume due to thermal accumulation which leads to expansion and consequent density decrease [9]. However, with a low repetition rate system (1 kHz), positive refractive index changes caused by a combination of depolymerisation and crosslinking were observed [7].

Negative refractive index changes were also reported in other materials when kilohertz low repetition rate lasers were used. For example, in crystalline quartz, irradiated material can transform into amorphous state, which causes localised expansion and induces strong strains to the surrounding matrix, hence, the irradiated region shows a negative refractive index change [10, 11, 153]. Chan et al. [154] observed a similar behaviour in sodium aluminium phosphate glass (Schott IOG-1). A negative refractive index change was due to increased cooling rates leading to a stress mechanism around the exposed area. In general, these

modifications in inorganic glass materials are fundamentally different to that of PMMA, and they can be attributed to restructuring of the silica networks [155, 156].

2.8.2. Measurements of refractive index change

The refractive index change value is a very important parameter that can be used to characterise the modified structures inside transparent materials. It can significantly affect the diffraction efficiency of gratings, and the acceptance angle of waveguides. A number of methods have been utilised to determine the refractive index change. They can be categorised into three groups. Firstly, traditional direct measurements can be made using ellipsometry, Abby refractometry, interferometeric methods, and prism coupler devices [157]. They can be used on large homogeneous areas, such as thin films, but are not suitable for internal structures. Secondly, there are indirect measurements, which use optical or physical properties of the modified structure to calculate refractive index changes, e.g. waveguide NA, grating diffraction efficiency or chemical etching speed. Thirdly, high resolution measurements can be made by employing the refracted near-field method [7], focussing method [158], and quantitative microscopy technique [159].

Grating theories

Kogelnik theory (Coupled Wave Theory) [160] and Raman-Nath theory [161] are the most commonly used models for theoretical analysis of thick gratings (Bragg regime) and thin gratings (Raman-Nath regime), respectively. A grating thickness

parameter, Q, is generally used as a criterion to determine whether the grating is thick or thin [162, 163]. Q is given by

$$Q = \frac{2\pi\lambda L}{n\Lambda^2} \tag{2.1}$$

where, λ is the readout wavelength, L is the grating thickness, n is the refractive index of the bulk material, and Λ is the grating period, as depicted in Fig. 2.8-1. When the grating thickness parameter $Q > 10$, the grating is a thick grating; while for $Q < 1$, the grating is thin [164].

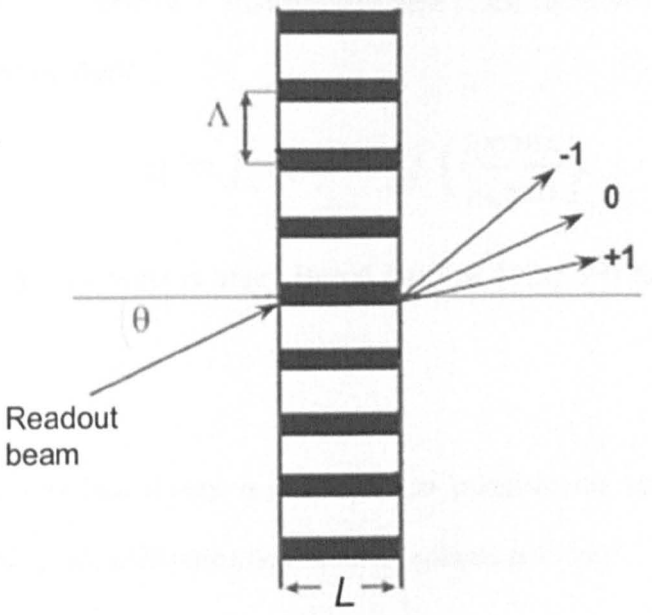

Fig. 2.8-1: Schematic of a readout beam passing through a grating.

For a thick grating under the Bragg condition, according to Kogelnik theory, the first order diffraction efficiency η is related to the refractive index change, Δn, by the equation,

$$\eta = sin^2\left(\frac{\pi\Delta nL}{\lambda cos\theta_b}\right) \tag{2.2}$$

where, θ_b is the first order Bragg angle.

In fact, Kogelnik theory only considers the first and zero order components, when a plane wave propagates through a diffraction grating with a sinusoidal variation of its refractive index, $n = n_0+\Delta n\sin(2\pi x/\Lambda)$. Therefore, if higher order harmonics are considered, a more complete theory, Rigorous Coupled Wave theory [162], will be required.

For a thin grating, according to Raman-Nath theory, the refractive index change Δn can be estimated from

$$\eta = J_1^2(\delta) = J_1^2\left(\frac{2\pi\Delta nL}{\lambda cos\theta}\right) \tag{2.3}$$

where $J_1(\delta)$ is the first order ordinary Bessel function [165], θ is the angle of the incident beam.

In this thesis, Kogelnik theory is employed to calculate the refractive index change and analyse the diffraction behaviour of volume gratings.

2.9. Parallel processing

Although amplified Ti:Sapphire laser systems are the most commonly used femtosecond lasers for internal structuring of materials, the effective throughput of such systems is relatively low. At 1 kHz, pulses with energy $E_p < 1$ μJ are typically focussed within an optical substrate with a single beam while carefully

scanning the substrate longitudinally or transversely to generate the required Δn. Since pulse energy E_p > 1 mJ is generally available at 1 kHz, the light utilisation factor is < 0.1%. A number of approaches have been demonstrated in previous studies to create multiple beams in order to improve the internal processing speed, including two-beam interference [69, 91, 119, 123, 166, 167], Diffractive Optical Elements (DOEs) [168] and Spatial Light Modulators (SLMs) [108, 122, 148, 149, 169-181].

The two-beam interference technique can produce multiple line structures simultaneously for grating writing, but the grating thickness is limited [91]. A DOE, which works as a hologram to modulate the input beam, can be designed to generate arbitrary multi-beam patterns. However, it is costly to manufacture and each device can only produce one fixed pattern [168]. By using an SLM addressed with appropriate CGHs to create a large number of diffracted beams of the requisite pulse energy, processing efficiency can be increased by more than an order of magnitude, reducing the fabrication time while allowing arbitrary parallel processing.

In this section, an introduction to SLM technology, including the operational principle and CGH calculation algorithms, will be presented, followed by a review of applications, with particular regard to femtosecond laser internal structuring area.

2.9.1. Introduction to spatial light modulators

An SLM can provide fine control of incoming light and allow the creation of 3D patterns with controlled characteristics, enabling a wide range of applications in photonics. The device consists of an array of pixels, each of which can individually control the phase or amplitude of incoming light. They can be used not only to correct for wavefront aberrations, but also to split an energetic laser beam into many arbitrary diffracted spots in 2D and 3D. In fact both of these abilities can be demonstrated simultaneously. In short, SLMs are remarkable optical devices which demonstrate sophisticated control of incoming wavefronts.

Since their introduction in the 1980's [182], SLMs have attracted increasing attention in many research areas, such as temporal pulse shaping [182], holographic optical tweezers [183-187], spatial beam shaping [188-192], wavefront correction [108, 149] and laser parallel processing [193-196].

There are two dominating SLM technologies. The first are micromechanical SLMs that use an array of movable mirrors to alter the physical path of the incoming light, and they are only available in reflective mode. The second are electro-optical SLMs that are based on various types of liquid crystal (LC) displays, and can work in either transmissive or reflective mode. In this thesis, only reflective LCSLMs are employed, because they are more cost effective and flexible than the micromechanical SLMs, and offers higher light utilisation efficiency than their transmissive counterparts. Despite the ability of both the

phase and amplitude modulation of the SLMs, only the phase modulation is investigated in this thesis.

Nematic LC is the most commonly used material for the LCSLMs. Fig. 2.9-1 shows a typical structure of a LCSLM. LC molecules in the LC layer can be controlled by the voltage applied to the ITO and the electrodes. This voltage is dependent on the greylevel of the CGH that is applied onto the SLM. Under the E field, the LC molecules make a voltage-dependent rotation, resulting in a refractive index change. Consequently, the phase of the incoming light is modulated (see Fig.2.9-1).

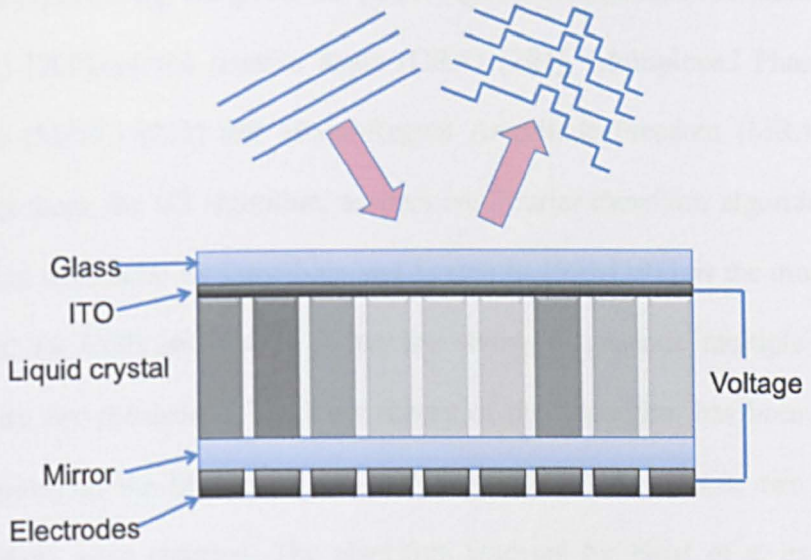

Fig. 2.9-1: Typical structure of a LCSLM.

Depending on the LC cell configuration, the LCSLMs can be divided into two categories, twisted nematic liquid crystal devices and parallel aligned nematic liquid crystal devices. In a reflective twisted nematic LCSLM, the LC cells are filled with LC molecules that form a twisted structure, and they have two director

plates aligned at a relative angle of 45° between the top and bottom of the LC layers. Polarised light passing through these cells follows the helical molecule axes, leading to a polarisation change. However, in a parallel aligned nematic LCSLM, the LC cells comprise two parallel director plates. Therefore, it can modulate the phase of the incoming light without affecting the polarisation.

2.9.2. Computer Generated Holograms

A variety of algorithms for calculating CGHs have been proposed for producing multi-beams using SLMs, including Gerchberg-Saxon (GS) [197], Gratings and Lenses (GL) [198], Weighted GS (GSW) [199], Generalised Adaptive Additive (GAA) [200],optimal rotation angle (ORA) [201], Multiplexed Phase Fresnel Lenses (MPFL) [202] and Mixed-Region Amplitude Freedom (MRAF) [203]. Among them, the GS algorithm, an iterative Fourier transform algorithm, which was first introduced by Gerchberg and Saxton in 1972 [197], is the most popular method for CGH calculation. It has the ability to generate multiple beams in arbitrary two-dimension. The basic theory of this algorithm has been discussed extensively in the literature [185, 197, 204, 205]. Based on it, two improved algorithms were reported. The algorithm reported by Haist et al extended its capability from 2D to 3D [206]. And the weighted GS algorithm further improved the efficiency and uniformity of the multiple beams [199].

Another non-iterative algorithm, Gratings and Lenses reported by Liesener et al. [198], is also widely used. It can generate 3D multiple beams through a complex superposition of prisms and lenses. Due to its non-iterative approach, the

calculation speed of this algorithm is fast. However, the efficiency and uniformity are relatively low, compared with the iterative algorithm. It can be utilised in real-time manipulation of the multiple trapping for optical tweezers, but not suitable for high precision microprocessing.

2.9.3. Surface ablation using a spatial light modulator

This section will demonstrate the typical multi-beam surface processing techniques for different applications, such as selective ablation of organic light emitting diodes (OLED) and silicon wafer processing. Preliminary work has been presented by the author and his colleagues at the Laser Group of the University of Liverpool [169, 195].

Laser patterning is a key industrial process in the manufacturing of OLED displays, solid-state lighting foils and solar cells. Ultrafast lasers are of particular interest for this application as they may enable selective ablative removal of OLED layers with minimum energy density requirements on the target. Since sufficient laser output from commercial laser sources is currently exceeding single beam process requirements, parallel processing with multiple beams could provide a novel route for up-scaling processing speed and reducing manufacturing costs. High throughput precision patterning of thin film electrodes (ITO anode and metal cathode) on flexible and glass substrates was demonstrated using an SLM [169, 195]. By carefully adjusting the number of beams per line, selective removal of different amounts of materials simultaneously in adjacent locations all within a single scanning step was also performed (see the following sections).

2.9.3.1. High throughput multi-beam processing

OLEDs are multi-layer materials, with each layer having its own ablation threshold. For example, the top cathode layer, aluminium, has lower ablation threshold than the underlying anode layer, ITO film [207], so by controlling the laser fluence, selective removal of the aluminium can be achieved. Cross hatch patterning of an OLED sample using 15 parallel beams (from a 10 ps HighQ IC-355-800 Nd:VAN regeneratively amplified picosecond laser system) produced by an SLM at 532 nm wavelength is shown in Fig. 2.9-2.

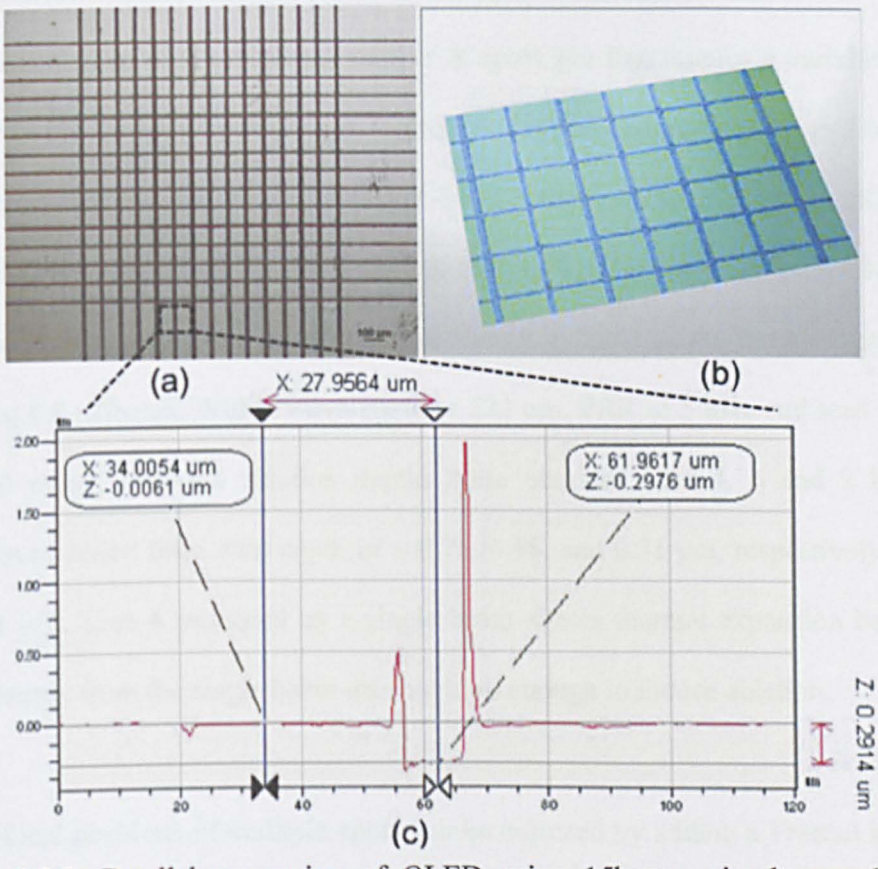

Fig. 2.9-2: Parallel processing of OLED using 15beams simultaneously. (a) Optical micrographs; (b) 3D surface profile; (c) Cross-sectional profile of a single line. [195]

The laser pulse energy, the repetition rate and the scanning speed were 12 μJ, 5 kHz and 30 mm/s, respectively. Only a single scan was conducted, resulting in multiple scribe lines with a pitch of 86 μm, the line widths of ~ 10 μm and the depths of ~ 290 nm. The scribe line, as demonstrated in Fig. 2.9-2 (c), shows a flat bottom area that indicates the cathode and the organic layers were removed, while the underlying anode, ITO film, remained unaffected. Optimisation of parameters can improve the processing quality (see Section 3.5.2).

2.9.3.2. Selective ablation of multi-layer structures

Beam scanning with a different number of spots per line mimics a variable spot overlap and can produce different controlled ablation depths, as presented in Fig. 2.9-3. 10 beams were arranged in a 4-3-2-1 pattern so as to achieve selective ablation with a single scan. The small red dots in Fig. 2.9-3(a) denote the 10-beam pattern used for scribing. The total pulse energy incident on the sample was 8 μJ, giving 0.8 μJ/beam. With a wavelength of 532 nm, PRR of 5 kHz and scan speed of 30 mm/s, different ablation depths were obtained, and 4, 3 and 2 beams produced scribe lines with depth of ~ 0.76, 0.68, and 0.31 μm, respectively (Fig. 2.9-3 (c)). Line 4 produced by a single beam shows thermal expansion because the energy from the single beam was not high enough to induce ablation.

The focal positions of multiple spots can be adjusted by adding a Fresnel lens to the CGH. Using a pulse energy of 0.8 μJ/beam and a scan speed of 30 mm/s, 3 lines with different depths were inscribed on OLED, as shown in Fig. 2.9-4.

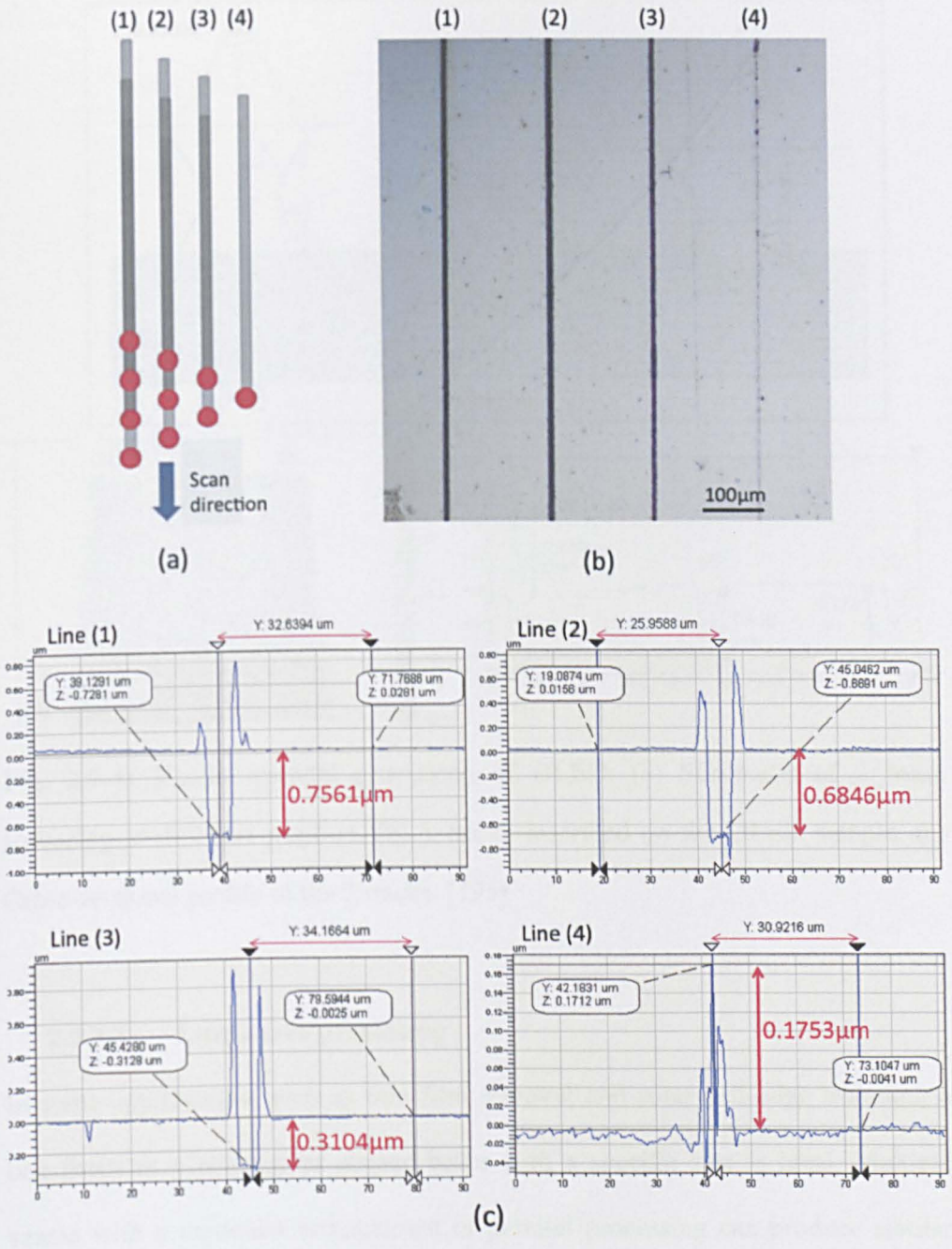

Fig. 2.9-3: (a) Schematic of selective ablation using a different number of spots per line to produce different ablation depths. (b)4 tracks produced by 10 beams on an OLED sample using the spots pattern shown in (a).(c) Surface profile of the 4 tracks. Lines 1, 2, 3 and 4 correspond to the label in (a) and (b). [195]

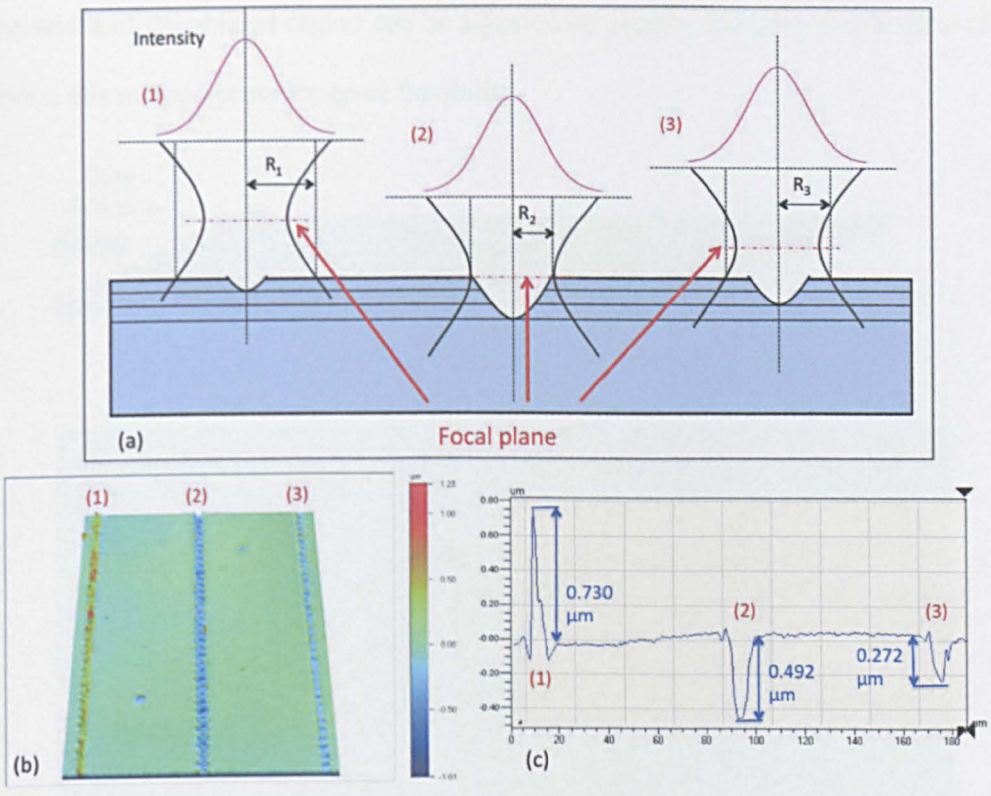

Fig. 2.9-4: 3-beam parallel processing of OLED. (a) Schematic of 3 beam focussing at different position. (b) 3 tracks inscribed on the OLED sample. (c) Cross-sectional profile of the 3 tracks. [195]

2.9.3.3. Large area processing

In some applications, such as thin film removal and solar cell edge isolation, a line focus or a rectangular shaped beam with a specific size is ideal. Multiple beams with a particular arrangement of parallel processing can produce similar results to scanning a rectangular shaped beam, as illustrated in Fig. 2.9-5(a). 40-beam parallel processing on silicon sample (Fig. 2.9-5(b)), with pulse energy ~1.75 µJ/beam, repetition rate 5 kHz, scan speed 1 mm/s and one overscan, produced a 457.6 µm wide and 5 µm deep ablated region. The GSW algorithm was used to calculate the CGH, because a symmetric pattern was required. Since

the width of the ablated region can be adjusted by simply changing the number of spots, this method provides great flexibility.

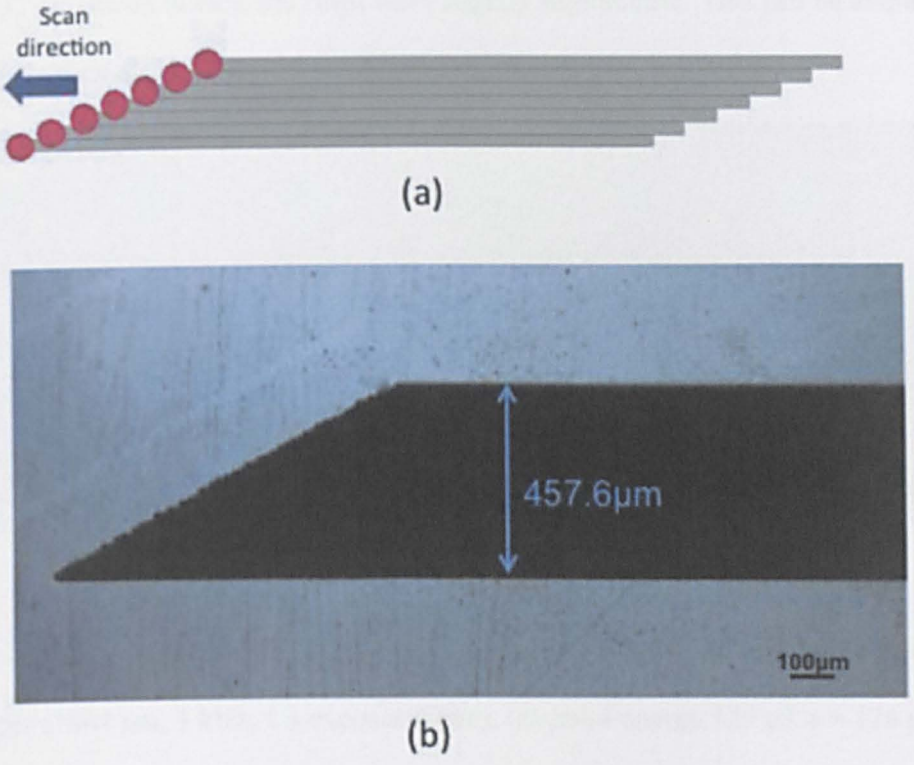

Fig. 2.9-5: Multi-beam large area processing. (a) Schematic diagram, (b) 40-beam parallel processing of silicon at 532nm. [195]

2.9.3.4. Beam shaping

Annular beams, which were generated by an LC-R 2500 SLM using diffractive axicon holograms with a laser at 1064 nm and 10 ps pulse duration, were used to ablate ITO thin film on a glass substrate. The radii of the annular beams were controlled by adjusting the spatial frequency of the holograms. Patterning using a CGH with higher spatial frequency (1.67 line pairs/mm (lp/mm)) produced a ring of radius r = 174 µm (Fig. 2.9-6 (a)), while with lower spatial frequency (0.83

lp/mm) CGH, a ring of r = 90 μm was produced (Fig. 2.9-7 (b)). The pulse energies used were 129 μJ and 75 μJ, respectively. Due to the small curvature of the LC on silicon device, the rings were slightly asymmetric. This can be avoided by applying a distortion correction pattern during the processing.

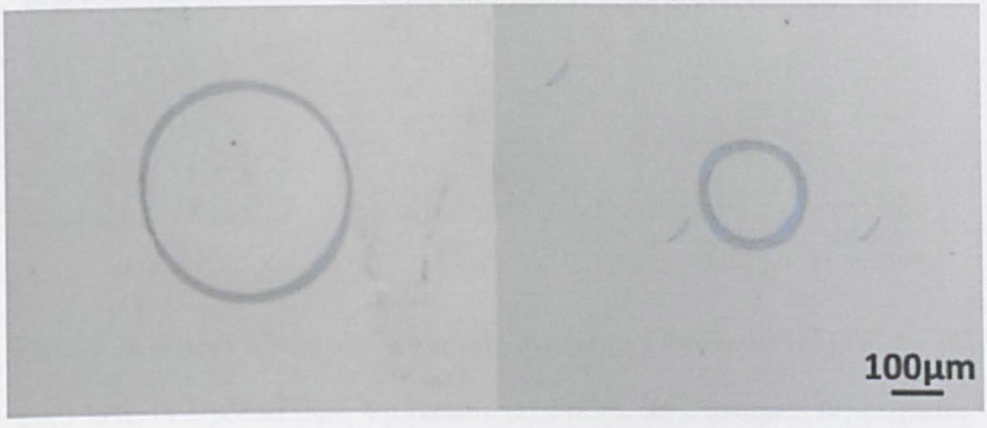

Fig. 2.9-6: Annular shape produced by an SLM with a ps laser on an ITO on glass sample (1064 nm, 5 kHz, 1 s exposure time), (a) pulse energy 129 μJ, r = 174 μm, (b) pulse energy 75 μJ, r = 90 μm. [195]

Parallel marking using a shaped 2-beam generated by using the GS algorithm within a Labview environment (see Section 3.5.1) is demonstrated in Fig. 2.9-7. Femtosecond laser pulses (170 fs, 775 nm, 1 kHz, 4 μJ/beam) were focussed through a 0.5 NA objective onto a stainless steel sample. The exposure time was 1s. The uniformity and the resolution can be improved by increasing the number of iterations during the CGH calculation or using an SLM with smaller pixels, e.g. the Holoeye Pluto SLM with 8 μm pixels.

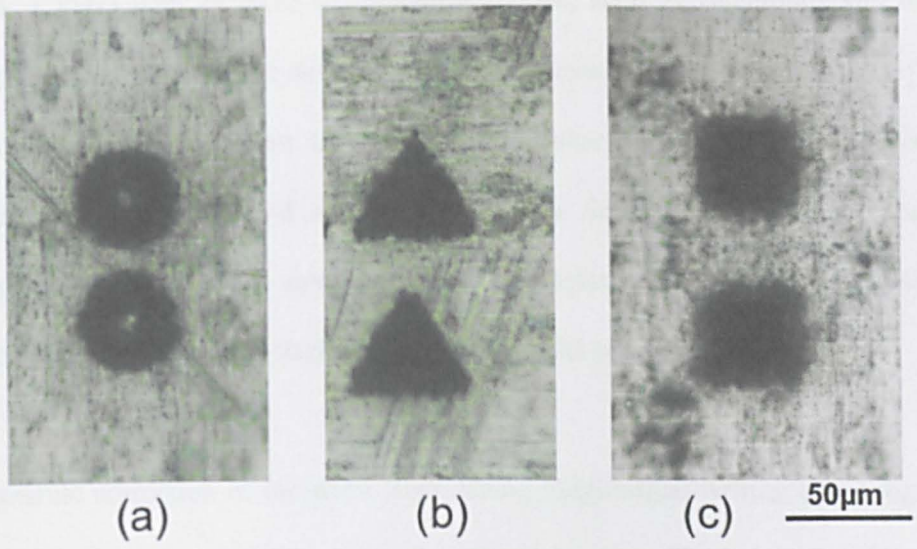

Fig. 2.9-7: Shaped 2-beamsimultaneously marking on stainless steel (170 fs, 775 nm, 1 kHz, 1s exposure time, 4 μJ/beam). (a) 2 rings, (b) 2 triangles, (c) 2 squares. [195]

2.9.4. Internal structuring with a spatial light modulator

In 2005, Hayasaki et al. [208] adopted this technology and applied it to laser material processing. Since then, he and his group demonstrated a number of applications [173, 174, 202, 209-214] using multiple femtosecond laser beams. The first implementation of internal structuring using a femtosecond laser (150 fs, 800 nm, 1 kHz) was realised using a multiplexed phase Fresnel lenses algorithm in 2006 [173]. 15 beams were focussed in three different positions, on the surface and inside glass at 15 μm and 20 μm depths. In order to improve the uniformity of the multi-beam, a method that could compensate for the spatial frequency response of the SLM was proposed [209]. Moreover, in 2008, multi-beam 3D data recording was reported by this group using single pulse irradiation (150 fs, 800

nm, 1 kHz) with an SLM in biological tissues, such as fingernails and dental prostheses [174]. Further developments of this technique by Jesacher at al. [149] provided viable solutions to the problems induced by the zero order beam, chromatic aberration and spherical aberration during the 3D data recording process. In these cases, since only fixed pre-calculated CGHs were employed, they can be described as static multi-beam parallel processing.

Dynamic correction of the wave front during longitudinal writing of waveguides opened up a new route for internal structuring using SLMs by Mauclair et al [108]. Later, the same group presented dynamic multi-beam processing using an adjustable binary phase mask created by an SLM [148]. Efficient waveguide couplers in fused silica were produced by 2-beam (150 fs, 800 nm, 10 kHz) 3D parallel writing in longitudinal geometry. More recently, this dynamic approach was also applied in transverse geometry to generate 2D and 3D waveguides [170, 176, 181]. As depicted in Fig. 2.9-8(a) and (b), 3D 1 × 4 splitter waveguides were dynamically written inside a glass substrate with multiple beams (2 μJ/beam) by displaying a series of CGHs on an SLM. A laser system at 1 kHz, 120 fs, 800 nm and an objective with 0.45 NA were employed. The splitter comprised a single straight region (A-B), a branching region (B-C), a separating region (C-D), and a four-straight region (D-E) (see Fig. 2.9-8(b)). By changing the CGHs, other examples of splitters were also produced, demonstrating the great potential of the SLM technology. [167]

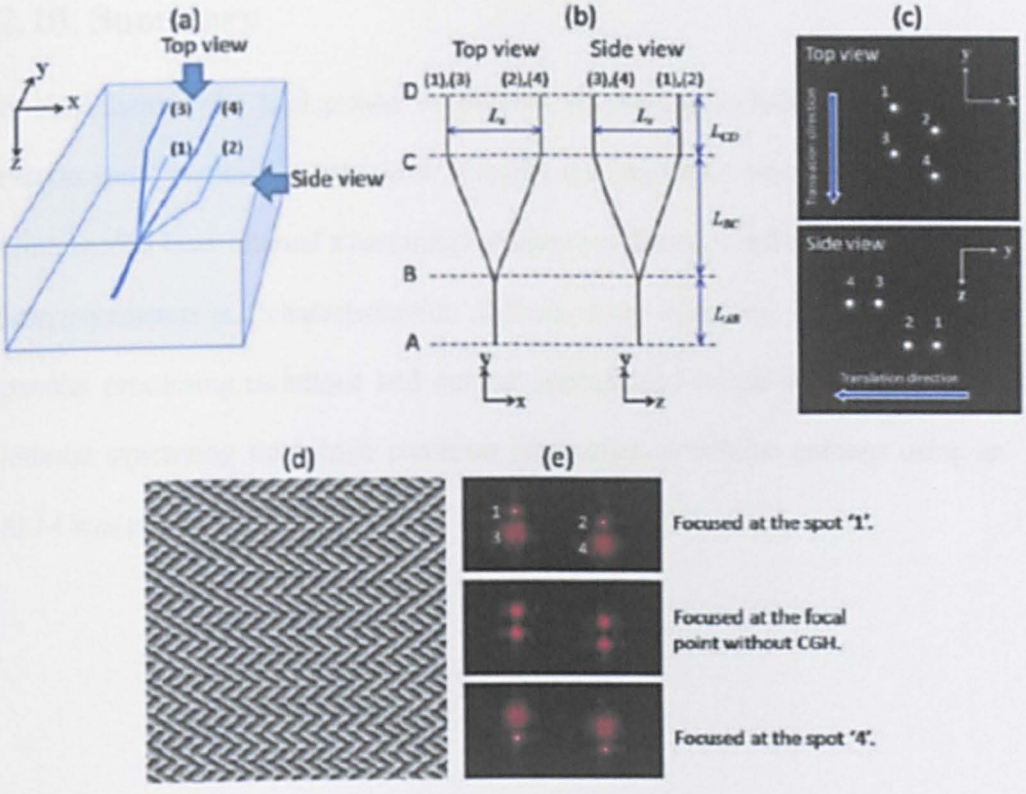

Fig. 2.9-8: (a) Schematic of a 1×4 splitter fabricated in glass substrate. (b) Top and side views of the splitter. (c) Distribution of multiple spots for writing the splitter. (d) Example of a CGH used in writing the splitter. (e) Simulated light intensity distributions in the splitter. [167]

In general, ultrafast laser internal structuring using an SLM has the ability to provide high throughput and remarkable flexibility. However, it is noteworthy that previous works mainly concentrated on two areas, data recording and waveguide fabrication. Little attention has been paid to the fabrication of another important photonic component, the volume Bragg grating. In the next few chapters, a new method of rapid fabrication of volume gratings using an SLM will be presented.

2.10. Summary

In this chapter, the background of internal structuring including basic theory, mechanisms, commonly used laser systems and materials was introduced. The femtosecond laser internal structuring techniques, effects of different material and laser parameters and characterisation methods were discussed. By reviewing the parallel processing technique and current applications in the femtosecond laser internal structuring field, high precision fabrication of volume gratings using an SLM was proposed.

Chapter 3 - Experimental

3.1. Introduction

This chapter will introduce the materials, PMMA and fused silica, and the equipment including the femtosecond laser system and SLMs used in this research, followed by the experimental setups for the single and multiple beam internal structuring. The procedures for measuring grating diffraction efficiency and calculating CGHs will also be discussed.

3.2. Materials

PMMA is a polymer material that is widely used as photonic material due to its ease of processing, low cost and excellent optical performance including high transparency, appropriate refractive index, and high optical isotropy. Because PMMA has high transmission in the visible and near IR spectral region, it has been employed as the core material for polymer optical fibre and as a substrate for integrated optical devices. Therefore, PMMA is the material of choice to explore the rapid fabrication of photonic components by femtosecond laser internal structuring.

Clinical grade bulk PMMA, Vistacryl CQ, from Vista Optics [215] has been employed in this research. Compared to commercial grade PMMA, these samples contain no additives and trace impurities, which are not clinically safe. The material has a density of 1.16 g/cm^3, a refractive index n_0 of 1.48 at 775 nm (n_0 = 1.50 at 387 nm) and a glass transition temperature of 105°C to 120°C.

Fused silica is a high purity colourless synthetic amorphous silicon dioxide. Owing to its very low thermal expansion coefficient, excellent optical qualities and exceptional transmittance over a wide spectral range, especially in UV, it is a commonly used optical material in various applications. The UV grade fused silica samples with a dimension of 30 × 30 × 5 mm^3 used in this project were supplied by UQG Optics [216].

3.3. Equipment

3.3.1. Femtosecond laser system

An amplified fs laser system, Clark-MXR CPA 2010, was used in this research. The system's fundamental wavelength of 775 nm can be frequency-doubled to produce 387 nm NUV wavelength by using a thin, 0.6 mm thick BBO crystal. The output Gaussian beam (see Fig. 3.3-1) has a diameter of 6 mm and a pulse energy of 1 mJ with ~ ±1% stability. The repetition rate, the pulse duration and M^2 are 1 kHz, 170 fs and 1.3 respectively.

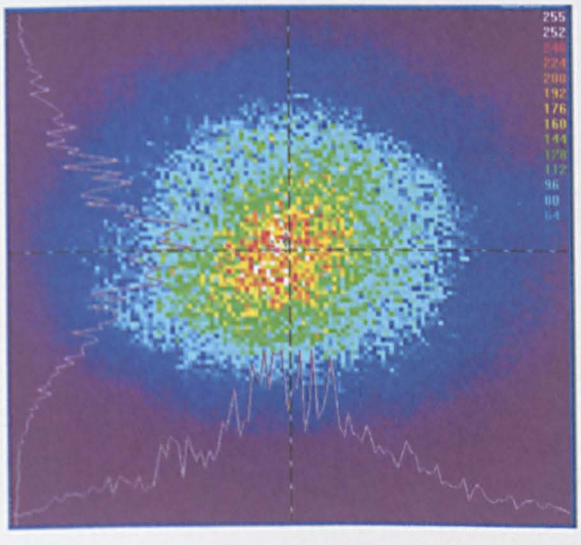

Fig. 3.3-1: Beam profile of the femtosecond laser system, Clark-MXR CPA 2010.

As described in Section 2.9, this laser system provides low throughput and low speed during laser processing, especially internal structuring. Hence, splitting the high pulse energy laser beam into multiple beamlets is an effective approach to increase the throughput and speed, as discussed in Chapter 4, 5 and 6.

3.3.2. Spatial light modulators

Two SLMs, Holoeye LC-R 2500 [217] and Hamamatsu X10468-02 [218], have been employed in this work. Table 3.1 shows the specifications of both SLMs.

Table 3.1 Specifications of SLMs

Model	**Holoeye LC-R2500**	**Hamamatsu X10468-02**
LC Type	45° twisted nematic	Parallel aligned nematic
Number of input level	256 (8 bits)	
Resolution (pixels)	XGA (1024×768)	SVGA (800×600)
Pixel pitch (μm)	19	20
Effective area (mm^2)	19.5×14.6	16×12
Mirror coating	Broadband metallic	Dielectric
Readout wavelength (nm)	400 – 775*	800±50
Light utilisation efficiency**	~75%	94%
Fill Factor	93%	95%
Response time*** **(rise/fall ms)**	10/18	25/65
Frame rate (Hz)	72	60

* Although the standard specifications recommend 400-700 nm, LC-R2500 can operate at 775 nm with low laser pulse energies.

** The actual light utilisation efficiency depends on the amount of diffraction loss caused by the pixelated structures and the reflectivity, which is affected by readout light wavelength.

*** Time required to change from 10 % to 90 % for 2π modulation.

3.3.2.1. Hamamatsu X10468-02

The X10468-02 has a dielectric mirror, which provides 94% light utilisation efficiency, but can only work within a specified wavelength range. Applying a voltage to the X10468-02, which is a parallel aligned nematic crystal device, results in the LC molecules aligning horizontally along the optical axis, hence causing a phase change to the light polarised along the molecular axis, but leaving the light polarised perpendicular to the molecular axis completely unaffected.

3.3.2.2. Holoeye LC-R 2500

By comparison, the LC-R2500 is equipped with a metallic coated mirror that offers lower light utilisation efficiency ~ 75%, but covers a wider wavelength range from visible to NIR. Compared with the parallel aligned nematic crystal device, the LC-R 2500 has a 45° twisted nematic LC layer in which the LC molecules are arranged in a twisted array from the front to the back, hence it can not only modulate the phase of light, but also rotate the plane of polarisation.

Although the X10468-02 can provide higher efficiency, due to limited availability, it was only employed in the NIR multi-beam parallel processing work (Chapter 4 and 5). The LC-R 2500 was adopted for the NUV parallel processing work (Chapter 6).

3.4. Experimental setup

3.4.1. Single beam direct writing

The experiments were performed using the Clark-MXR CPA-2010 with repetition rate of 1 kHz, pulse duration of 170 fs, and fundamental wavelength of 775 nm. The 387 nm NUV wavelength was produced by frequency doubling of the fundamental wavelength using a BBO crystal. The experimental setup is schematically shown in Fig. 3.4-1. A high energy variable diffractive attenuator was used for continuously adjusting pulse energy. After passing through the attenuator, a shutter and a telescope, the laser beam was expanded to a diameter of 15 mm, and reflected by mirrors M2-M5 before being focussed by a lens. The samples employed in the experiments were bulk PMMA (30 × 30 × 5 mm^3), which were optically polished on all surfaces and mounted on a computer controlled 3-axis stage (Aerotech).

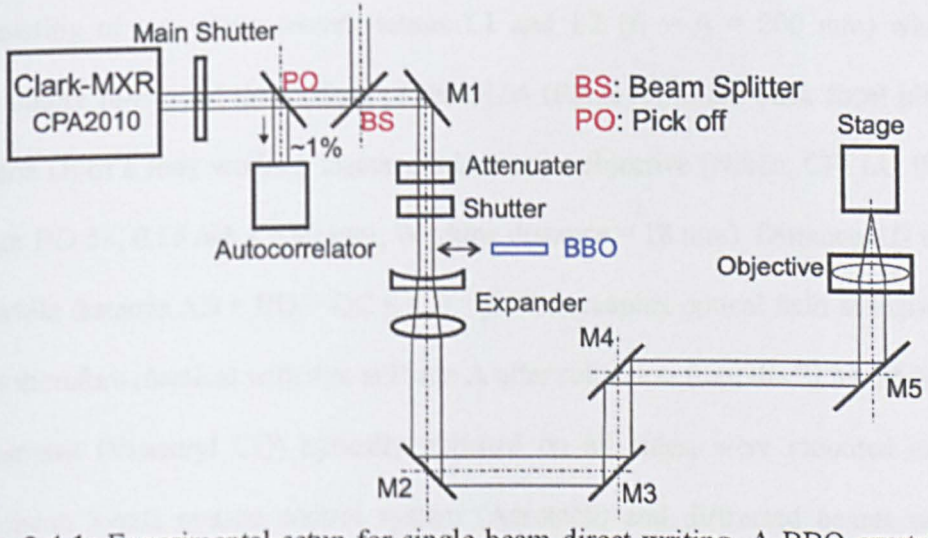

Fig. 3.4-1: Experimental setup for single beam direct writing. A BBO crystal is used to generate the second harmonic at 387 nm. The periscope, M3-M4 is actually in the vertical and rotated here 90° for clarity.

Using this setup, the effects of pulse front tilt and control of filament length were investigated. Different optical components were produced inside PMMA and fused silica samples using a single beam (see Chapter 4).

3.4.2. Multi-beam internal structuring

3.4.2.1. NIR experimental setup

The output from a Clark-MXR CPA-2010 fs laser system was attenuated and expanded to 8 mm diameter onto the SLM (Hamamatsu X10468-02) As shown in Fig 3.4-2(a), a 4*f* optical system was introduced to remove the remaining energetic zero order reflection at Plane P, near the Fourier plane of lens L1 (Plane Q) using a absorbing target on axis (see Fig 3.4-2(b)) [184]. First order diffracted beams, however, were focussed off axis and so were transmitted through a 4*f* system consisting of two plano-convex lenses L1 and L2 ($f_1 = f_2 = 200$ mm) which essentially re-imaged the surface of the SLM (Plane *A*) to the back focal plane (Plane D) of a long working distance microscope objective (Nikon, CFI LU Plan Fluor BD 5×, 0.15 *NA*, $f = 40$ mm, Working distance = 18 mm). Distance *AD* was 4*f* while distance AB = BQ = QC = CD = *f*. The complex optical field at Plane D was therefore identical with that at Plane A after reflection from the SLM. PMMA substrates (Vistacryl CQ) optically polished on all sides, were mounted on a precision 3-axis motion control system (Aerotech) and diffracted beams were carefully focussed > 0.5 mm below the substrate to keep the fluence at the interface below the damage threshold. An effective $NA_{eff} = 0.1$ was used here.

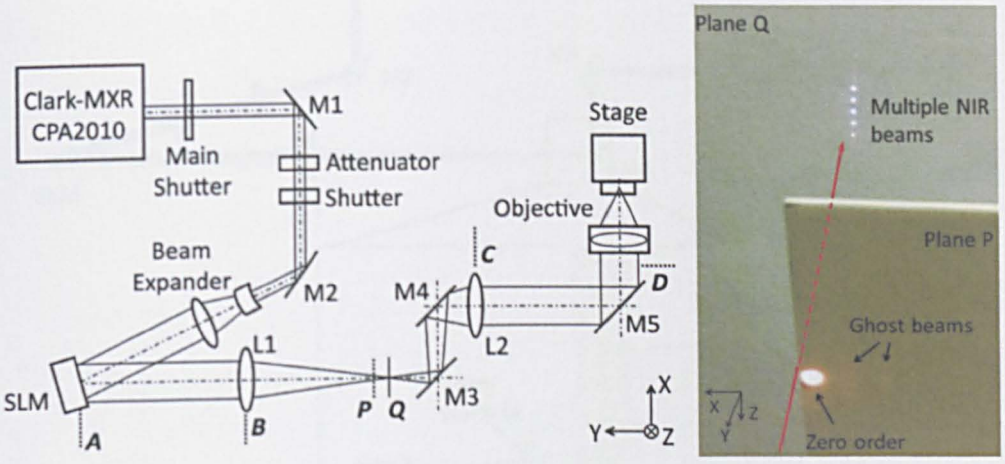

(a) (b)

Fig. 3.4-2: (a) Schematic of the experimental setup for NIR parallel processing. A 4f optical system (L1, L2) with unity magnification helps to remove the residual zero order beam at Plane P while re-constructing the complex field at Plane D. (b) Image showing the elimination of the zero order and ghost beams. The red arrow indicates the laser beam propagation direction around Plane P and Q.

The modelling of the beam path in 3D using Zemax software is demonstrated in Fig. 3.4-3. In order to protect the mirror M3 from damage, it was placed about 16 mm away from the focal plane of the lens L1 (Plane Q). As depicted in the magnified view of Fig. 3.4-3, the Ray 1 with a diffraction angle of ~ 1.1°, which is the highest diffraction angle provided by the SLM (25 line pairs/mm) at 775 nm, has the smallest exposure area on the mirror. According to the modelling, the size of this area is 0.612 mm in diameter, and it is large enough to avoid damage to the mirror. The exposure areas of other beams are larger so that they cannot cause damage to the mirror either.

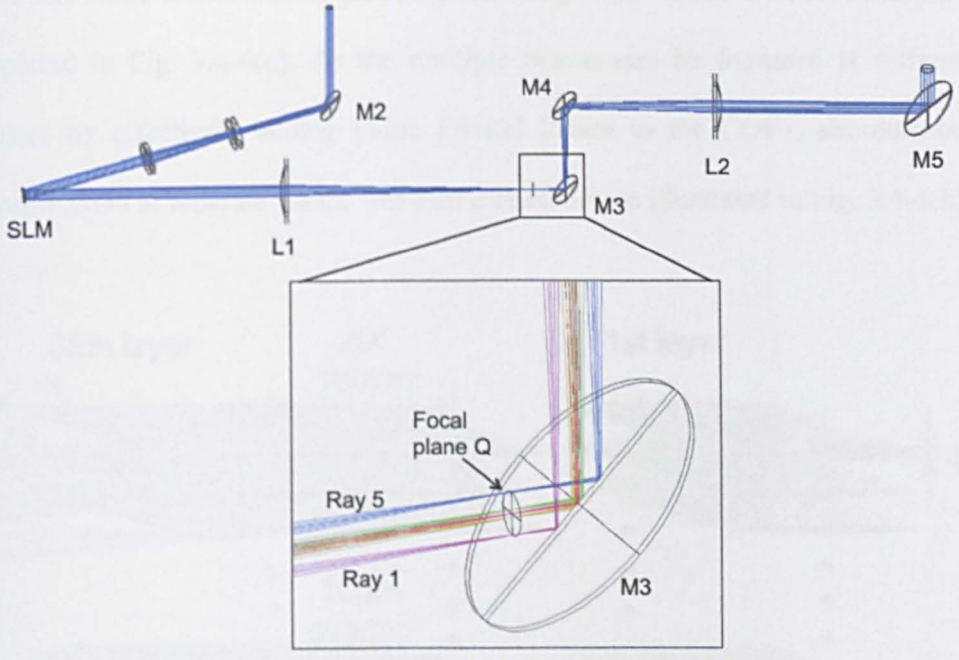

Fig. 3.4-3: Zemax modelling of the 3D beam path. (a) Beam expander and 4f system. (b) Expanded image showing the zero order beam (red) and the diffracted beams reflected from the turning mirror M3. The spot diameters of Ray 1 to Ray 5 are 0.751, 0.652, 0.641, 0.632 and 0.612 mm, respectively.

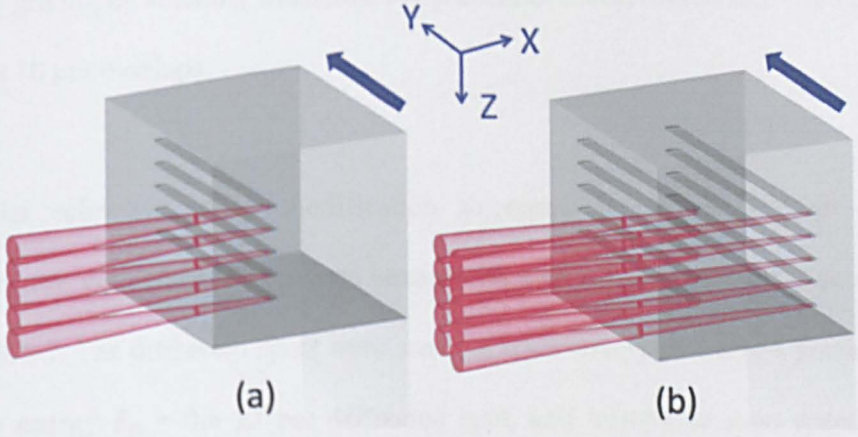

Fig. 3.4-4: Parallel writing inside PMMA. Transverse geometry for writing gratings in (a) single layer (2D) and (b) double layer (3D). The arrows denote the translation direction (+Y) of the sample.

The schematic of multi-beam parallel processing in 2D inside a PMMA sample is depicted in Fig. 3.4-4(a). As the multiple beams can be focussed at different planes by effectively adding phase Fresnel lenses to the CGHs, simultaneous modification at separate planes was also carried out, as illustrated in Fig. 3.4-4(b).

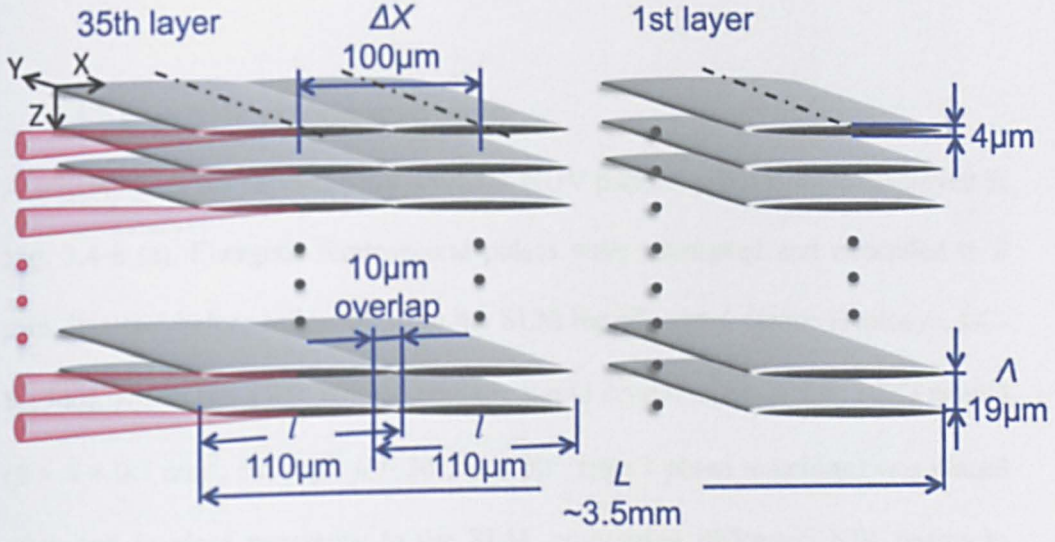

Fig. 3.4-5: Schematic of multi-beam modification to create continuous volume phase grating by stitching filamentary modifications with offsets ΔX =100 μm and hence 10 μm overlaps.

Parallel refractive index modification to create a grating without optical breakdown with 16 nearly uniform beams with a period Λ = 19 μm is illustrated in Fig. 3.4-5. The diffracted spots were scanned transversely to create a grating with pulse energy E_p = 0.6 μJ per diffracted spot, and transverse scan speed s = 1 mm/s, and each modified region was scanned once. As described in Section 2.7.1.4, in order to avoid the possible pulse front tilt effect, leading to asymmetric writing dependent on scan direction, the parallel writing was conducted in a single

direction only. The induced filaments are ~ 110 μm long and 4 μm wide (see Chapter 5 for optical images). By carefully stitching multi-layer with an offset of ΔX = 100 μm and an overlap of 10 μm (~ 10% overlap), a series of volume gratings with dimensions of 5 × 5 × 1-4 mm^3 were produced with reasonable continuity and uniformity (see Chapter 5).

3.4.2.2. NUV experimental setup

A schematic of the experimental setup for NUV parallel processing is displayed in Fig. 3.4-6 (a). Energetic femtosecond pulses were attenuated and expanded to 8 mm diameter before reflection from the SLM liquid crystal device (Holoeye, LC-R2500), which has a 45° twisted nematic liquid crystal layer. A thin BBO crystal (8 × 8 × 0.7 mm^3, cut angle $\theta = 30°$, $\psi = 90°$, type 1 phase matching) was placed after and in close proximity to the SLM, converting diffracted NIR beams to nearly collinear NUV beams. A 4*f* optical system with two plano-convex lenses (L1, L2, f = 194 mm at 387 nm) were set to re-image the SLM surface to the back focal plane of a plano-convex lens with a focal length f = 50 mm (effective NA_{eff} = 0.08). A $\lambda/2$ plate was used to rotate the direction of polarisation on to the SLM. The undiffracted zero order NIR and NUV components were blocked by a target near the Fourier plane of the first lens L1 (see Fig 3.4-6(b)). A periscope, mirrors M3/M4 along with mirror M5 (all dielectric coated for 387 nm) acted as dichroics, eliminating the remaining diffracted first order 775 nm radiation from the optical beam path. The PMMA samples were mounted on the 3-axis stage and the 387 nm parallel beams carefully focussed below the surface.

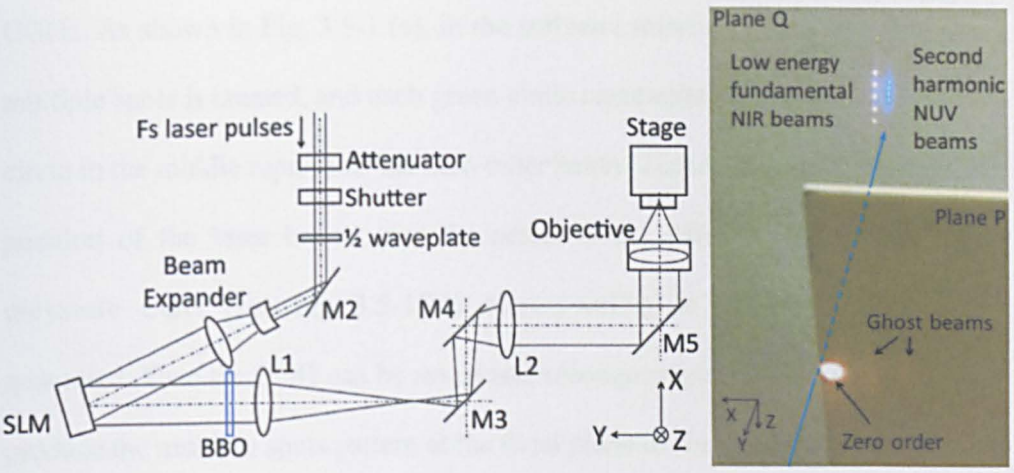

(a) (b)

Fig. 3.4-6: (a) Schematic of experimental setup for NUV parallel processing. (b) Image showing the elimination of the zero order and ghost beams. The blue arrow indicates the laser beam propagation direction around Plane P and Q. The NIR beams are eliminated by M3, M4 and M5, and the remaining energy is too low to cause modification in PMMA.

Since both the Holoeye SLM LC-R2500 and the BBO crystal are very sensitive to the state of input laser polarisation, combining these two devices together requires detailed analysis and careful alignment. The behaviour of the LC-R2500 and the phase matching of the crystal are presented in Chapter 6.

3.5. Calculation of computer generated holograms

3.5.1. Labview environment

A software package based on Labview environment provided by Glasgow University and developed especially for optical tweezers was used to generate

CGHs. As shown in Fig. 3.5-1 (a), in the software interface, a pattern comprising multiple spots is created, and each green circle represents one laser beam. The red circle in the middle represents the zero order beam. These circles only indicate the position of the laser beams, not the actual sizes. After calculation, the 8-bit greyscale CGH (see Fig 3.5-1(b)) corresponding to the desired pattern is generated. Then the CGH can be saved and subsequently displayed on the SLM to produce the multiple spots pattern at the focal plane of the lens.

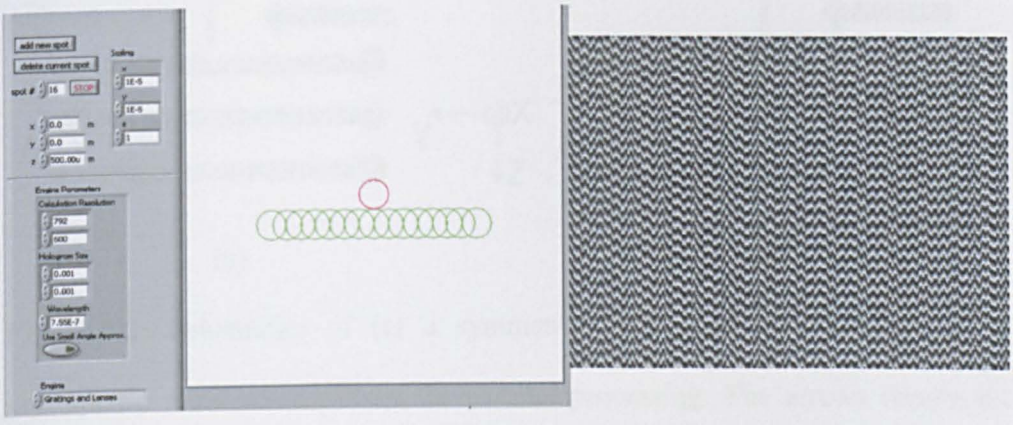

(a) (b)

Fig. 3.5-1: (a) The Labview interface with multiple spots pattern. The red spot in the middle represents the zero order beam. (b) The CGH generated using the GS algorithm in the Labview which will re-create the pattern

3.5.2. Optimisation of computer generated holograms

Periodic spot patterns with a high degree of symmetry (Fig. 3.5-2(a)) create degeneracy, leading to non-uniform intensity in diffracted beams from overlapping ghosts, resulting in significant intensity modulation [219]. Uniformity was improved greatly by breaking symmetry, for example, by introducing slight

random displacements of the required spot pattern (Fig. 3.5-2(b)). If N was a random number chosen between -1 and +1 and shift range S, e.g. 20 μm, the spots were offset randomly by a distance $N \times S$ in the Y axis (scan direction) while maintaining fixed pitch Λ (Fig. 3.5-2(b)).

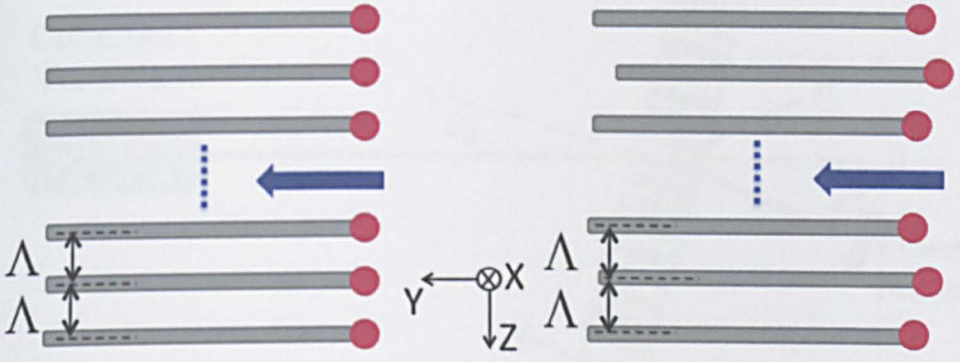

(a) (b)

Fig. 3.5-2: Schematics of (a) a symmetric multi-beam pattern and (b) an asymmetric multi-beam pattern for parallel processing. The arrows denote the translation direction (+Y) of the sample.

3.6. Diffraction efficiency measurement

A solid-state CW laser, Coherent Verdi V2, delivering 2W at 532 nm, was utilised for probing the volume gratings, because it can provide high beam quality (M^2 ≈1.01), high stability and low optical noise (< 0.02% rms). The output from the laser was attenuated to ~ 400 μW, and then passed through a volume grating sample that was mounted on a precision rotation stage. A silicon detector with power meter (Coherent LM1/Fieldmaster) was placed a metre away from the grating to measure the transmitted power into each order (see Fig. 3.6-1). The

diffraction curves were measured by placing the detector in turn at the location of each diffracted order and rotating the grating from normal incidence (see Chapter 5 and 6).

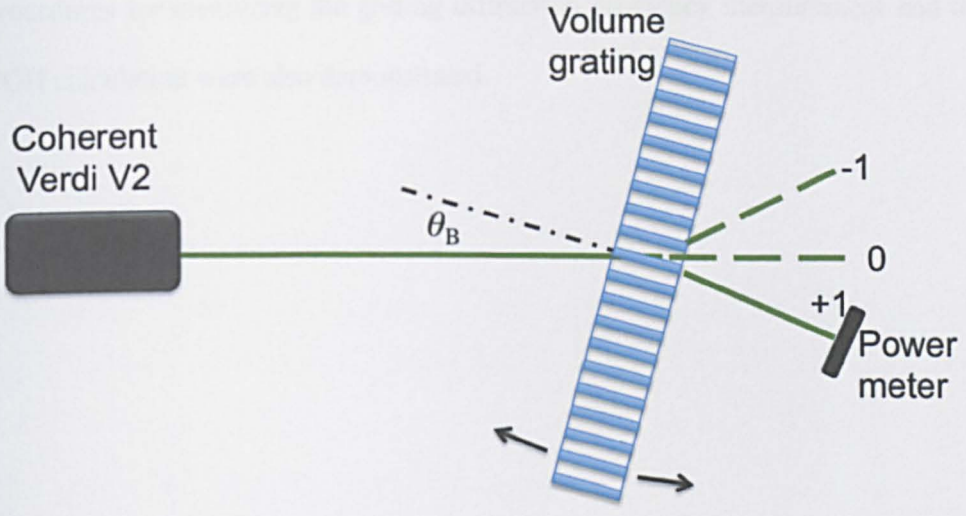

Fig. 3.6-1: Schematic of measuring the diffraction efficiency of volume gratings.

3.7. Other characterisation methods

An optical microscope with back illumination and a Nikon Digital Sight camera system were used to take optical images and measurements of the modified region inside transparent samples. Raman spectroscopy was also employed to analyse the refractive index modulation.

3.8. Summary

This chapter has introduced the materials (clinical grade PMMA and fused silica) and the equipment employed in this research, followed by the experimental setups

including the single beam direct writing, and the multi-beam parallel processing. The phase matching technique of the BBO crystal to optimize the diffractive beams while avoiding intensity modulation was discussed in detail. The procedures for measuring the grating diffraction efficiency measurement and the CGH calculation were also demonstrated.

Chapter 4 - Femtosecond laser internal structuring of materials

4.1. Introduction

This chapter is concerned with the optimisation of the femtosecond laser direct writing process. Firstly, for single beam direct writing, the dependence of induced structure length on laser pulse energy and wavelength is investigated. Secondly, the effect of pulse front tilt on the induced structures under current experimental conditions is presented and an approach for avoiding this effect is proposed. Thirdly, simple structures written with a single beam are demonstrated which can serve as a basis for the fabrication of more complex devices. Finally, multi-beam internal structuring is presented with the aid of an SLM, demonstrating the potential for high throughput rapid volume grating fabrication.

4.2. Single beam direct writing

4.2.1. Controlling filament length

When femtosecond laser pulses propagate through a transparent medium, dramatic changes of their spatial, temporal and spectral properties can occur [220]. The formation of a filament is attributed to the balance between self-focussing due to the nonlinear Kerr effect and self-defocussing associated with the formation of plasma generated by medium ionisation [127]. In order to obtain high quality in internal structuring, the induced structure length, which is related to the filament length during processing, needs to be controlled precisely. In this section, the effects of pulse energy and wavelength on the induced structure length in PMMA are investigated.

Using the experimental setup and procedures described in Section 3.4.1, filamentation has been studied in PMMA with femtosecond laser pulses at λ =775 nm and λ = 387 nm. The laser beam was focussed 2 mm below the sample surface using a plano-convex fused silica lens (f = 50 mm, $NA_{eff} \approx 0.15$). The stage was stationary during the laser exposure. Pulse energy of 0.1-5.5 μJ and exposure time of 0.5 s (500 pulses) were employed.

Fig. 4.2-1 shows highly periodic microstructuring with increasing pulse energy in the range of 0.1 - 1 μJ caused by refocussing in PMMA with a wavelength of 387 nm at peak power well above the threshold for self-focussing. Light scattering indicates that filamentation is also accompanied by dielectric breakdown. The modified regions extend towards the laser source with increasing pulse energy and over 10 periods are demonstrated. At 775 nm (Fig. 4.2-2), however, higher pulse energies were required to modify PMMA, resulting in a more chaotic structure. Re-focussing is also evident with damage regions again extending towards the source with increasing pulse energy. The modification threshold at 387 nm is lower since PMMA requires only two-photon absorption ($\sim \sigma^2 I^2$) to create seed electrons by excitation from the valence band to the conduction band, whereas 775 nm modification requires 3-photon absorption (($\sim \sigma^3 I^3$, $E_b \approx 4.58$ eV). It is observed that the length of the breakdown structure is proportional to the laser pulse energy, and the filaments develop towards the focussing lens, which is in good agreement with the results reported by Saliminia et al [127].

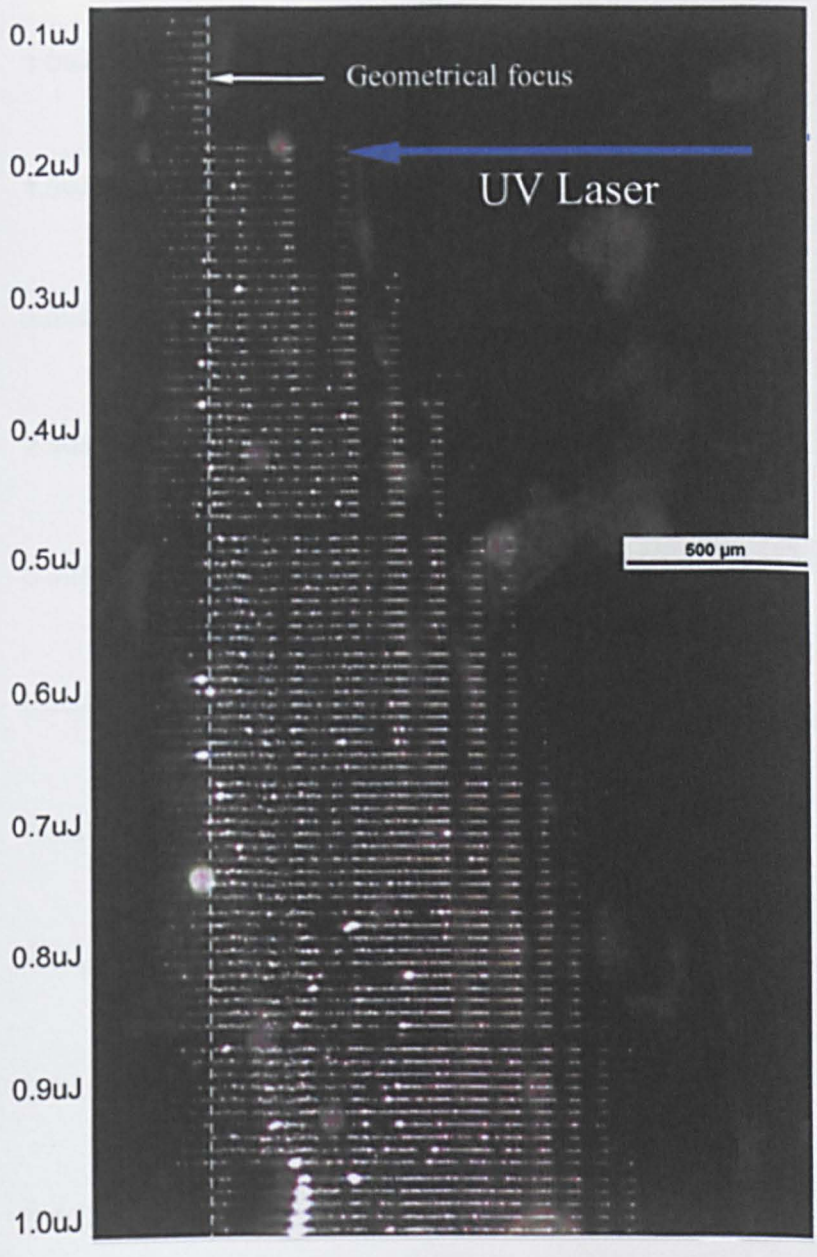

Fig. 4.2-1: Induced structures in PMMA by NUV (387 nm) laser pulses with various pulse energies (0.1 – 1 μJ) and 0.5s exposure time (500 pulses). The dotted line denotes the geometrical focal position. The blue arrow indicates the laser beam propagation direction. Each filament (line structure) was produced by 500 pulses, and at each pulses energy level, 10 filaments (line structure) were generated.

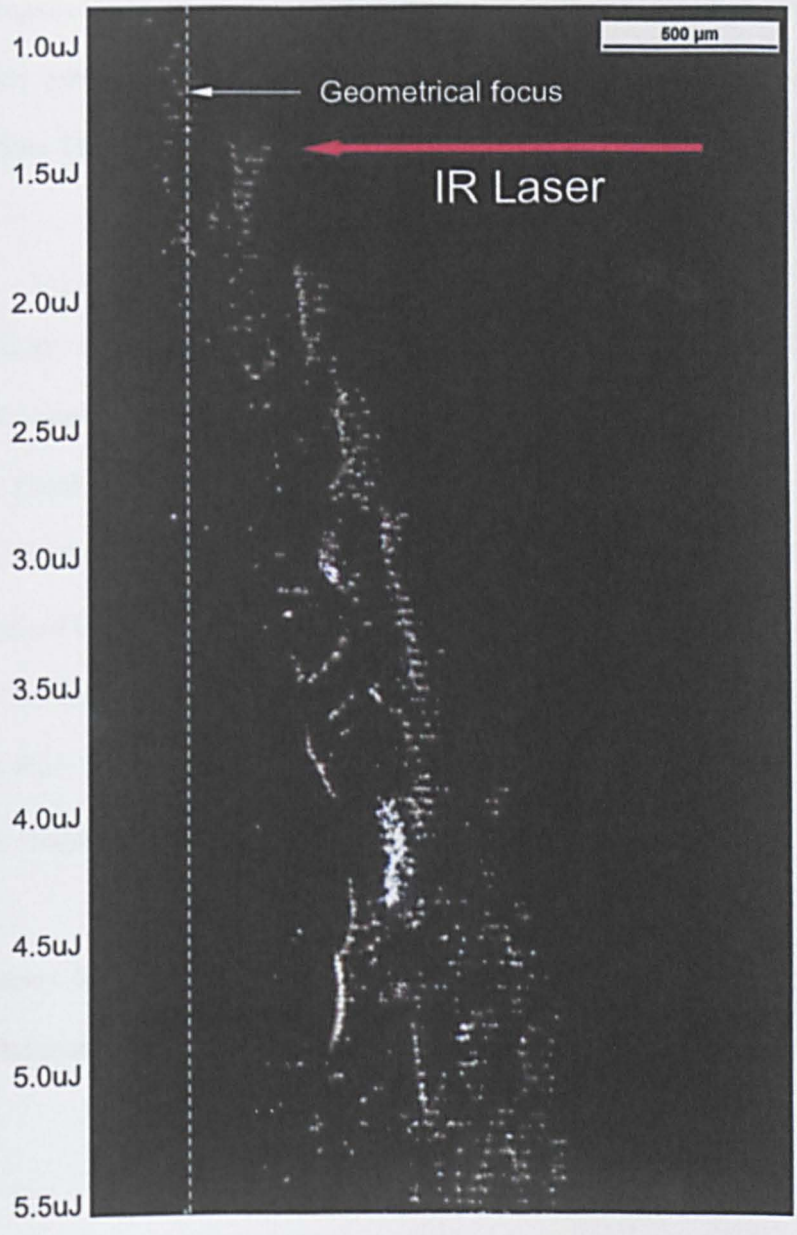

Fig. 4.2-2: Induced structures in PMMA by NIR (775 nm) laser pulses with various pulse energies (1 – 5.5 µJ) and 0.5s exposure time. The dotted line denotes the geometrical focal position. The red arrow indicates the laser beam propagation direction. Each filament (line structure) was produced by 500 pulses, and at each pulses energy level, 10 filaments (line structure) were generated.

In a homogeneous transparent medium, self-focussing of laser pulses occurs when input laser power P exceeds the critical power P_{cr}, and results in filamentary propagation. The critical power P_{cr} is given by [221]

$$P_{cr} = \frac{3.77\lambda^2}{8\pi n_0 n_2} \tag{4.1}$$

where λ is the wavelength, n_0 ($n_0 \approx 1.48$ at 775 nm and $n_0 \approx 1.50$ at 387 nm) is the refractive index of PMMA, and $n_2 \approx 2.7 \times 10^{-14}$ cm^2/W is the nonlinear refractive index of PMMA [222]. In the case of NUV exposure, the critical power is P_{cr} = 5.6 kW. The laser peak power P of 0.55 – 5.53 MW, corresponding to the pulse energies E_p of 0.1 – 1 μJ, used in the experiment, is significantly larger than P_{cr}, so that this nonlinear effect is indeed expected. For the NIR exposure, the critical power is P_{cr} = 22.3 kW, and as peak power P is in the range of 5.53 – 30.4 MW (E_p in the range of 1 – 5.5 μJ) also satisfies $P >> P_{cr}$.

The filament length, l_{fil}, generated by self-focussing of the laser radiation in a transparent material has a dependence, given by [223]

$$l_{fil} \propto \sqrt{\left(\frac{n_2}{n_0}\right)(P - P_{th})} \tag{4.2}$$

where P_{th} is the threshold laser power for inducing structural change. It has been observed that P_{th} has the same wavelength-dependence as that of P_{cr} [224], and P_{th} is related to P_{cr}. Hence, in general, P_{th} can be replaced by P_{cr} in Eq. 4.2 [225].

Assuming the induced structure length is proportional to the filament length, the theoretical values of the induced structure length were calculated and plotted

using Eq. 4.2 for both the NUV and NIR irradiation (see Fig. 4.2-3 and Fig. 4.2-4). Both figures depict the dependence of the induced structure length on the pulse energy. With the NUV exposure (see Fig. 4.2-3), the experimental results are reasonably consistent with the theoretical values, and they are in good agreement with the results reported by Shimotsuma et al. [225]. However, in the NIR exposure (see Fig. 4.2-4), there are differences between the experimental and the theoretical results, due to the less accurate length measurements of the chaotic breakdown structures shown in Fig 4.2-2.

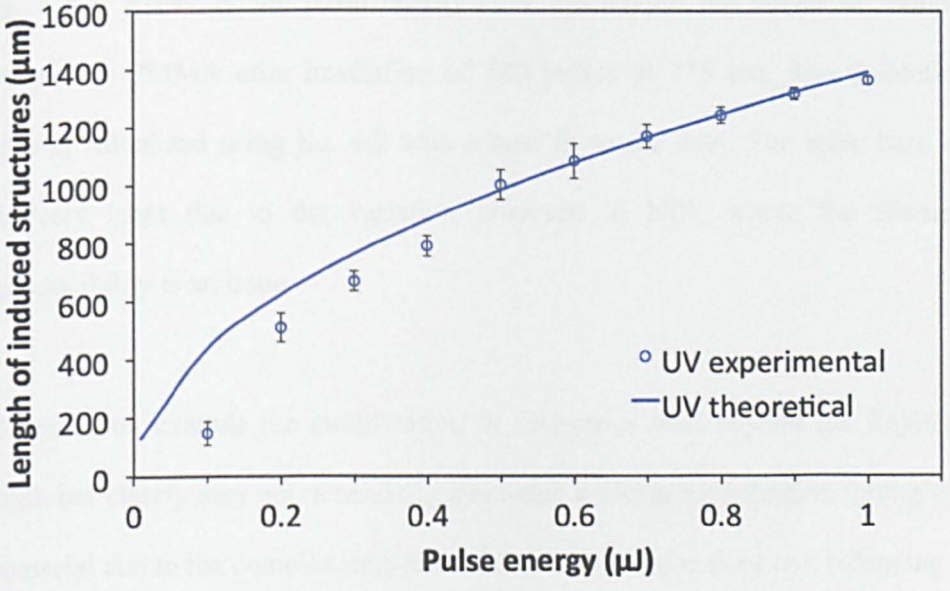

Fig. 4.2-3: Effect of the pulse energy (0.1 – 1 μJ) on the length of induced structure in PMMA after irradiation of 500 pulses at 387 nm. The theoretical curve is calculated using Eq. 4.2 with a best fit to the data showing good agreement.

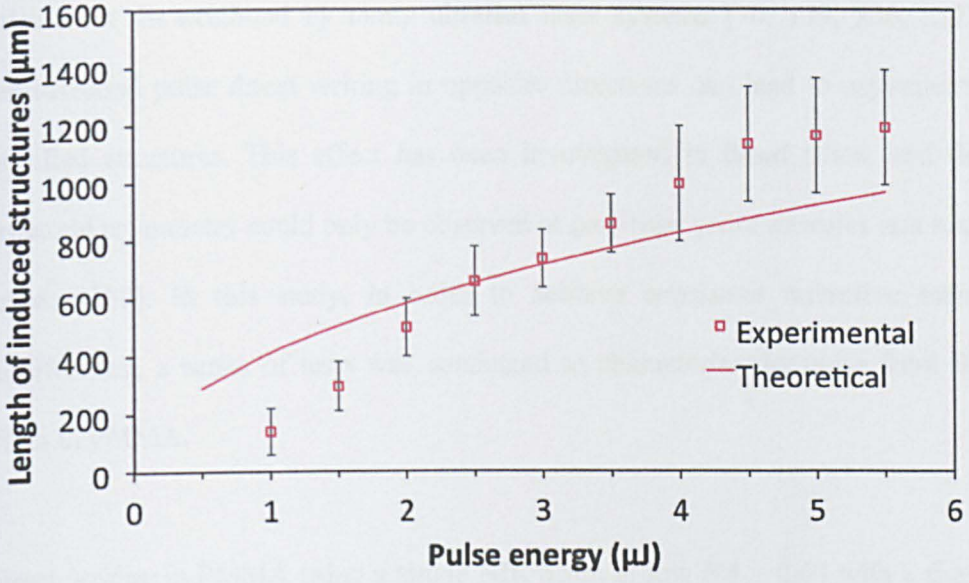

Fig. 4.2-4: Effect of the pulse energy (1 – 5.5 μJ) on the length of induced structure in PMMA after irradiation of 500 pulses at 775 nm. The theoretical curve is calculated using Eq. 4.2 with a best fit to the data. The error bars are relatively large due to the variation observed in NIR, where the filament reproducibility is an issue.

Filamentation extends the modification in dielectrics well beyond the Rayleigh length but clearly may not necessarily guarantee uniform modification throughout a material due to the complex non-linear interactions that make exact balancing of the self-focussing with plasma de-focussing difficult.

4.2.2. Eliminating pulse front tilt effect

As described in Section 2.7.1, an important parameter along with pulse energy, pulse duration, wavelength and scan speed in internal structuring is scan direction, which can cause a variation in the modified region dimensions due to the effect of

pulse front tilt exhibited by many ultrafast laser systems [70, 139, 226, 227]. Femtosecond pulse direct writing in opposite directions can lead to asymmetric modified structures. This effect has been investigated in fused silica, and the structural asymmetry could only be observed at particular pulse energies and scan speeds [139]. In this study, in order to achieve consistent refractive index modification, a series of tests was conducted to characterise the pulse front tilt effect in PMMA.

Direct writing in PMMA using a single NIR beam at low $NA = 0.04$ with a fixed pulse energy ($E_p = 0.6$ μJ, 775 nm) and various scan speeds ($s = 0.3$ - 1 mm/s) was performed. Fig. 4.2-5 (d-h) demonstrates the differences in structuring width obtained with $s \geq 0.6$ mm/s. The biggest variation in the width occurs at $s = 0.8$ mm/s, where the width of the structure written in the –Y direction is almost twice as that of written in the +Y direction. This effect is also accompanied by the observation of a significant change in the intensity of the plasma emission while writing in opposite directions, whereas no detectable difference can be observed when $s < 0.6$ mm/s (see Fig. 4.2-5(a-c)). However, this boundary ($s = 0.6$ mm/s) can change if different pulse energies or focussing conditions are applied [139].

Since there was no equipment able to monitor and quantify the pulse front tilt available to this project, a simple approach was utilised to eliminate the asymmetry by scanning in a single direction only. The drawback of course is that modification times are therefore increased.

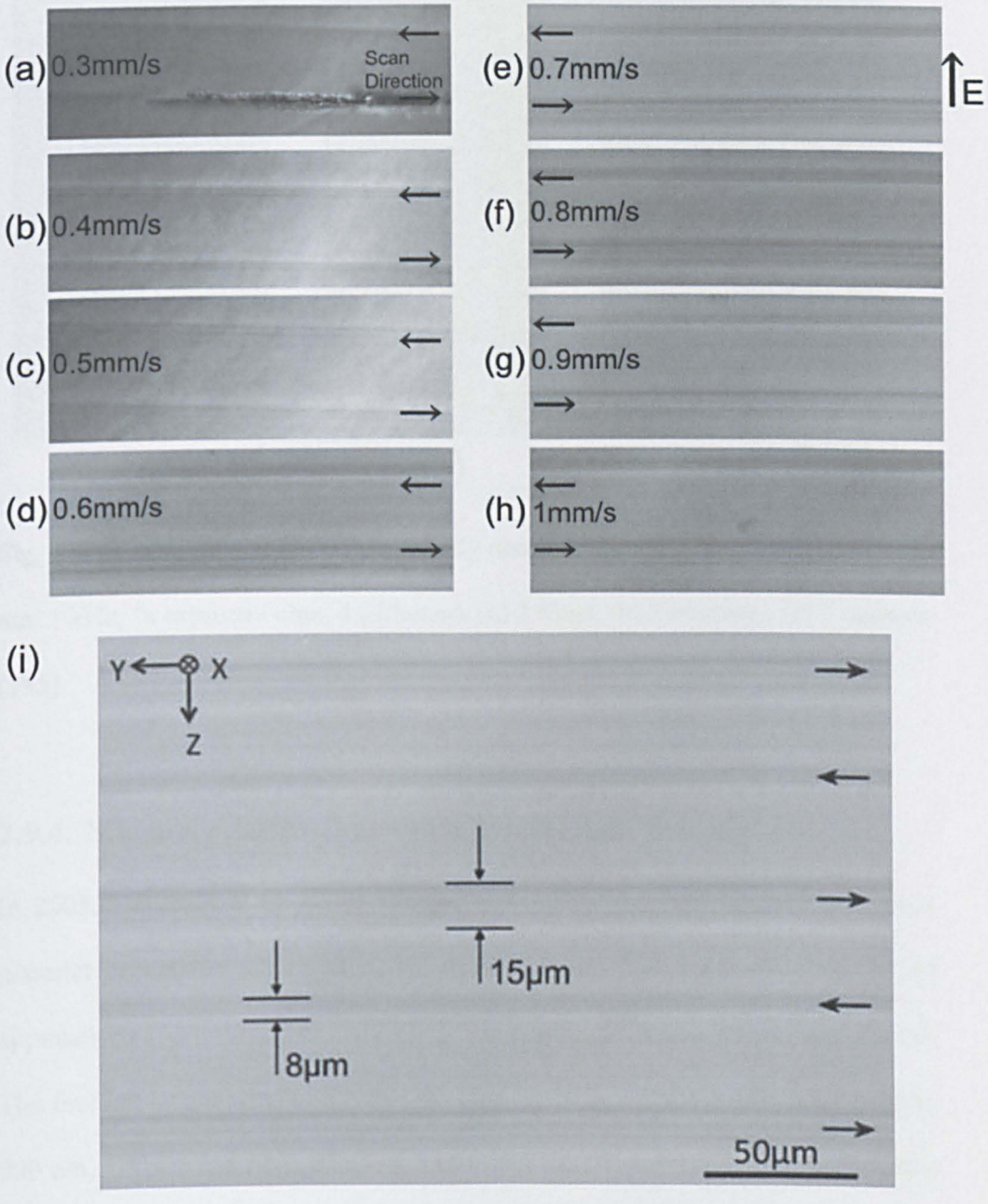

Fig. 4.2-5: Optical images showing the modification asymmetry due to pulse front tilt when writing in opposite directions at 775 nm. (a-h) Direct writing using a fixed pulse energy (E_p = 0.6 µJ) and various scan speeds (s = 0.3 - 1 mm/s) (i) Magnified image of (f) showing a significant difference in the width of the modified region. (E_p = 0.6 µJ, s = 0.8 mm/s, NA = 0.04). The polarisation direction is perpendicular to the writing direction.

4.2.3. Direct writing of optical components

Using the experimental setup and procedure described in the Section 3.4.1, various optical components were fabricated in PMMA and fused silica samples. Fig 4.2-6 shows a waveguide coupler written in PMMA using 387 nm laser pulses with pulse energy of 0.1 μJ, scan speed of 0.1 mm/s, and a 0.3 NA objective. However, coupling and guiding qualities were not good because of the elliptical cross section of the waveguide structures. Using NUV laser pulses with 0.8 μJ pulse energy and 1 mm/s scan speed, a grid grating, a ring grating and a square grating were produced inside PMMA (see Fig 4.2-7 and Fig 4.2-8).

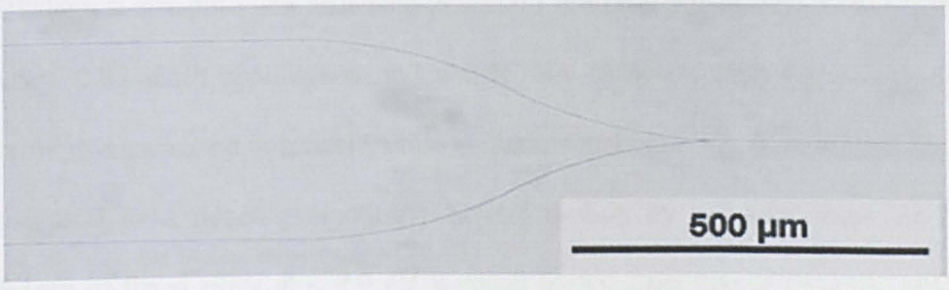

Fig. 4.2-6: A Y-coupler written in PMMA (387 nm, 0.1 μJ, 0.1mm/s, 0.3 NA)

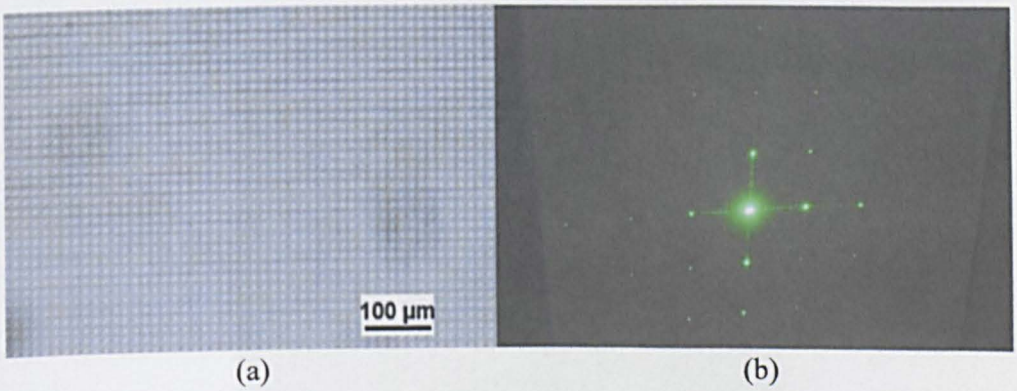

(a) (b)

Fig. 4.2-7: (a) A grid 2D grating with 15 μm period written in PMMA (387 nm, 0.8 μJ, 1 mm/s, 0.3 NA). (b) Diffraction pattern of the grid grating at 532 nm.

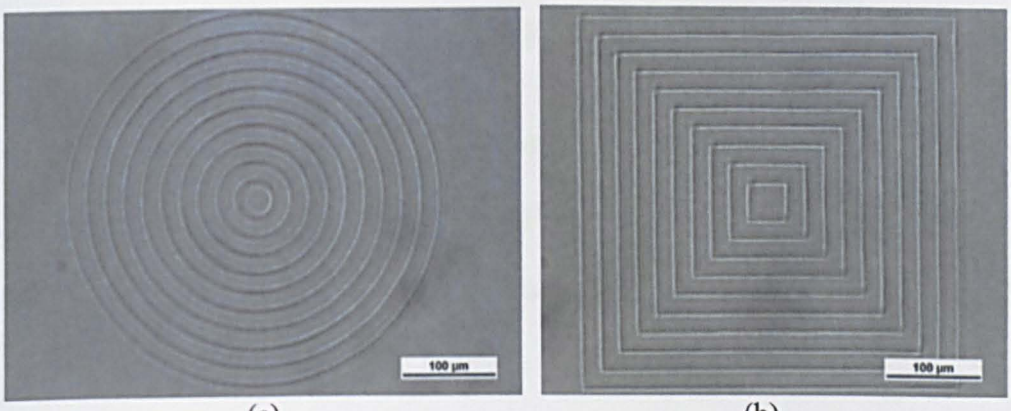

(a) (b)

Fig. 4.2-8: (a) A ring grating and (b) a square grating written in PMMA (387 nm, 0.8 µJ, 1 mm/s, 0.3 NA)

A 3D helical structure was produced using 775 nm laser pulses with 12.6 µJ pulse energy, 0.05 mm/s scan speed and a 0.15 NA objective (see Fig 4.2-9). The sample was translated in a circle while simultaneously moving the substrate along the optical axis, hence generating a helical motion by a 3-axis stage. As the bandgap of fused silica at ~ 8.9 eV is much higher than that of PMMA, and so requiring 6-photon absorption, the pulse energy required to modify the material is much higher and the scan speed is lower.

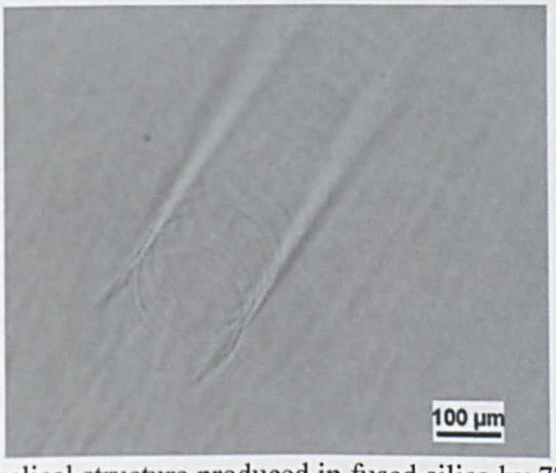

Fig. 4.2-9: A 3D helical structure produced in fused silica by 775 nm laser pulses (12.6 µJ, 0.05 mm/s, 0.15 NA).

4.3. Multi-beam direct writing

4.3.1. Improving multi-beam uniformity

Δn modification of PMMA without optical breakdown at 775 nm, 170 fs with 16 parallel beams with a period Λ = 19 μm is shown in the optical micrographs of Fig. 4.3-1. Pulse energy E_p = 0.6 μJ/beam, transverse scan speed s = 1 mm/s and 0.1 NA objective were used, and each modified region was scanned once only. As shown in Fig. 4.3-1(a), the cross sections of modified structures written with a symmetric beam pattern (see Fig. 3.6(a)) show a large variation in filament length l = 106.2 ± 26.3 μm (1σ) emphasising the intensity non-uniformity generated with this geometry. Adding a slight random asymmetry in the spot pattern, as discussed above in Section 3.6.2, removes degeneracy and ghost beam overlap, reducing intensity modulation, hence structure quality improved markedly. Fig. 4.3-1(b) displays the improved uniformity of the induced structures with filament length l = 109.9 ± 6.1 μm (1σ).

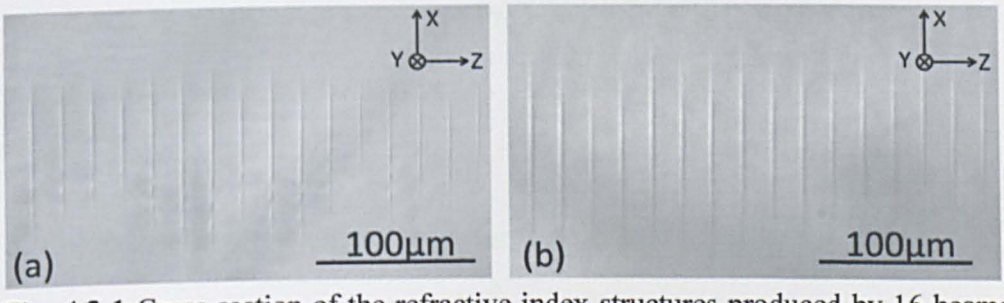

Fig. 4.3-1: Cross-section of the refractive index structures produced by 16 beams with (a) a symmetric spots pattern and (b) an asymmetric spots pattern. The filament lengths shown in (a) and (b) are 106.2 ± 26.3 μm (1σ) and 109.9 ± 6.1 μm (1σ), respectively. The laser beams propagated along the +X direction, and the sample translation direction was in the +Y direction.

4.3.2. Static multi-beam 2D direct writing

Using the optimisation method and the processing parameters discussed in Section 4.3.1, parallel writing with 16 near uniform laser beams within bulk clinical grade PMMA was performed (see Fig. 4.3-2). Clear refractive index modification without optical breakdown was obtained.

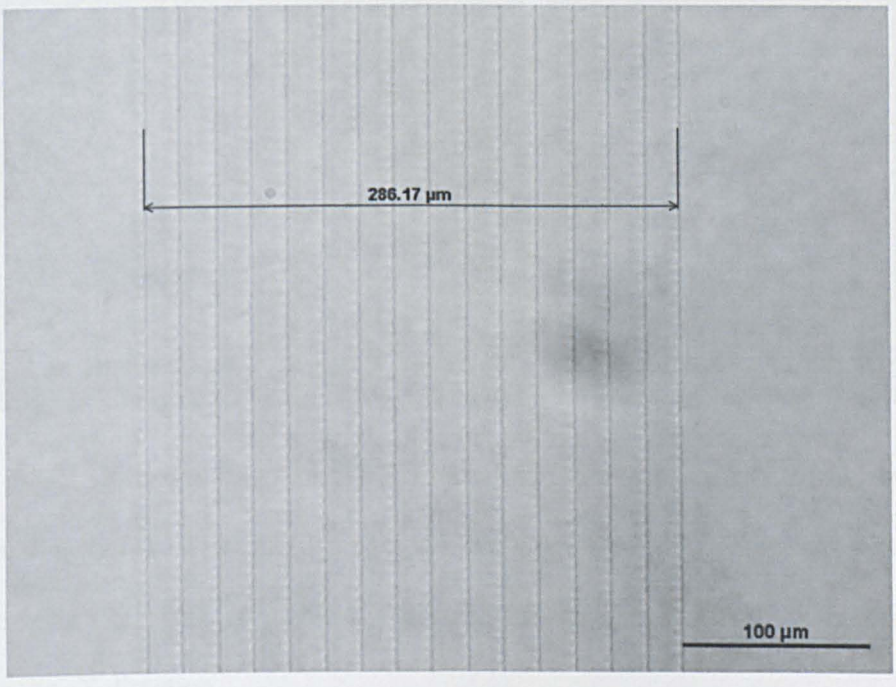

Fig. 4.3-2: 16-beam direct writing in PMMA with the optimised CGH (775 nm, 0.6 µJ/beam, 1 mm/s, 0.1 NA).

4.3.3. Static multi-beam 3D direct writing

By re-calculating CGHs to offset the focal planes of particular spots, simultaneous parallel 3D writing at different depths using 16 (2 × 8) beams in a double layer and 15 (3 × 5) beams in triple layer were demonstrated, as shown in the cross-sections of Fig. 4.3-3(a, b). The writing parameters were the same as those used in Section 4.3.2.

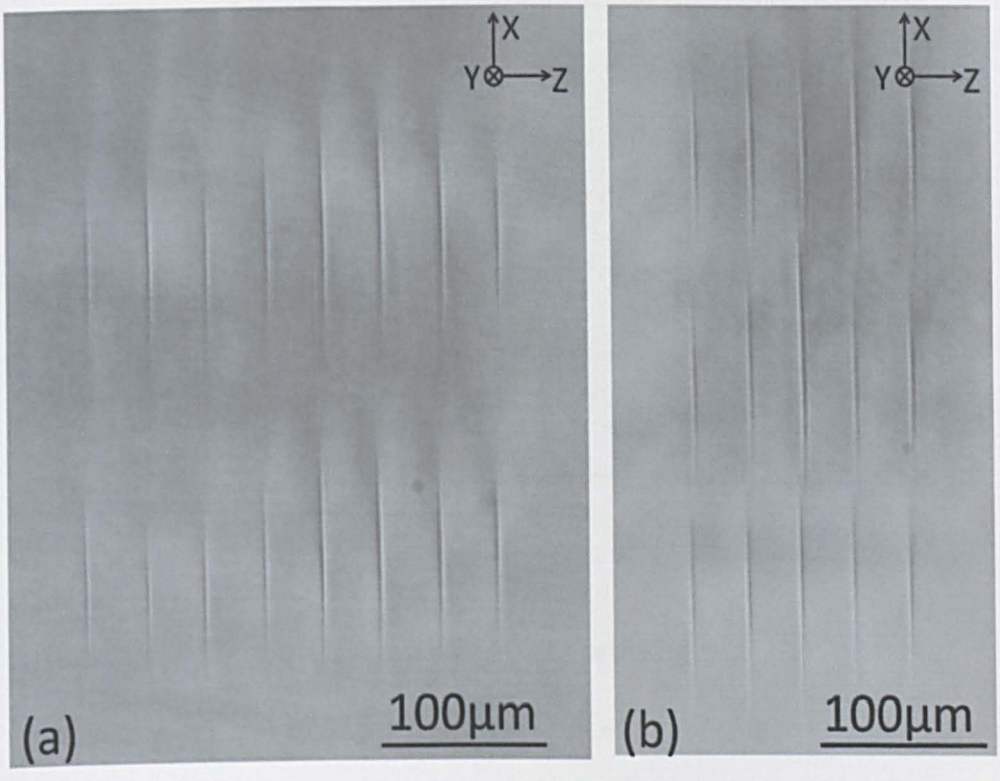

Fig. 4.3-3: Optical micrographs of 3D modified cross-sections in PMMA written in parallel by (a) 16 beams (2 × 8) in double layer and (b) 15 beams (3 × 5) in a triple layer (775 nm, 0.6 µJ/beam, 1 mm/s, 0.1 NA). The laser beams propagate along the -X direction.

3 beams (0 and ±1st order) with pulse energy of 5 µJ/beam produced by a binary grating hologram were used to fabricate cylindrical structures inside a fused silica sample (Fig. 4.3-4) which was translated in a helical motion at 10 µm/s towards the +X direction. The X-axis was parallel to the optical axis. The cylindrical structures produced, which were 1 mm in length and 200 µm in diameter, showed no sign of optical breakdown.

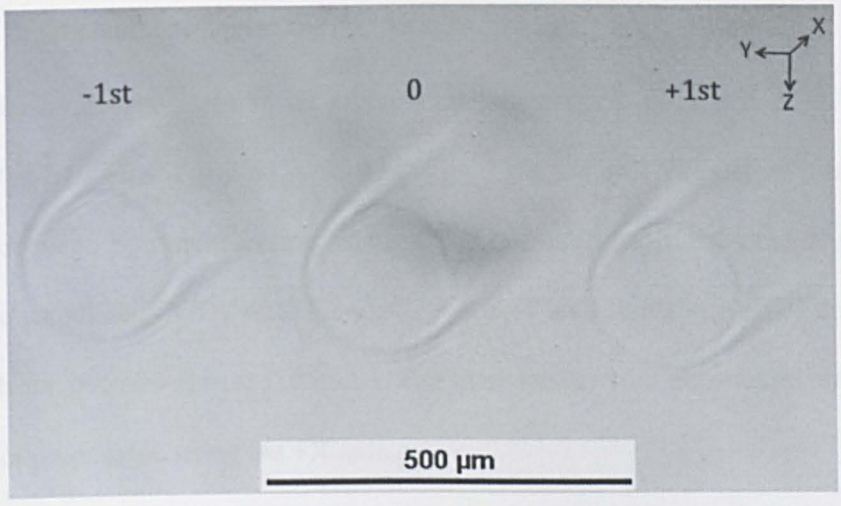

Fig. 4.3-4: 3-beam direct fabrication of cylindrical structures in fused silica.

4.3.4. Dynamic multi-beam 2D direct writing

By calculating a series of CGHs (9 CGHs), storing them, then synchronising to the scan motion (0.1 mm/s scan speed), 2D real time 8-beam modification at 387 nm with 0.21 µJ/beam pulse energy was demonstrated (see Fig. 4.3-5). The experimental setup and the procedures are described in Section 3.4.2.2.

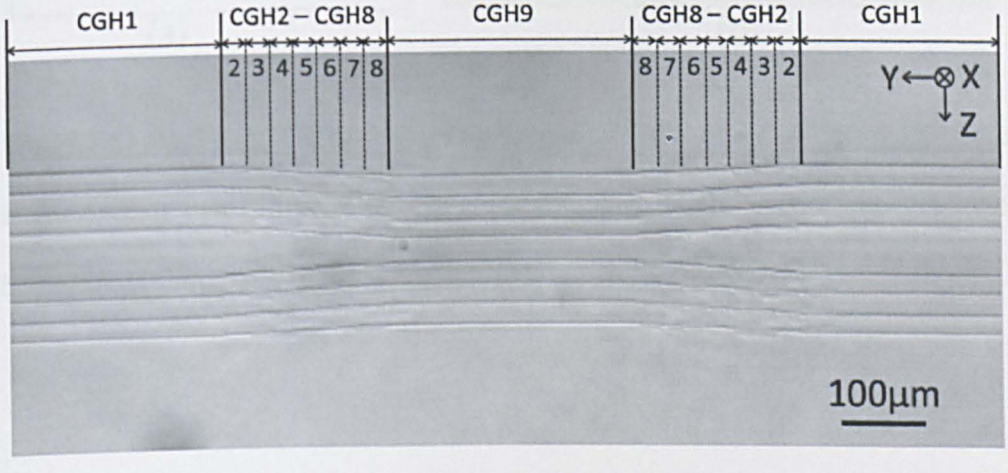

Fig. 4.3-5: 8-beam dynamic modification of PMMA addressing the SLM with 9 CGHs running at 4 Hz (CGH1-CGH9-CGH1) with 0.1 mm/s scan speed (0.08 NA).

4.3.5. Dynamic multi-beam 3D direct writing

Dynamic modification of fused silica with 5 beams (0, ±1st and ±2nd order) generated by a binary grating is demonstrated in Fig. 4.3-6. The helical structures were produced by synchronising rotation of 5 beams through real-time display of 120 pre-calculated CGHs at 20 Hz and 3° interval with linear motion of the stage towards the +X direction at 0.5 mm/s. The laser beams with pulse energies of 1.5 μJ/beam propagated along the +X axis.

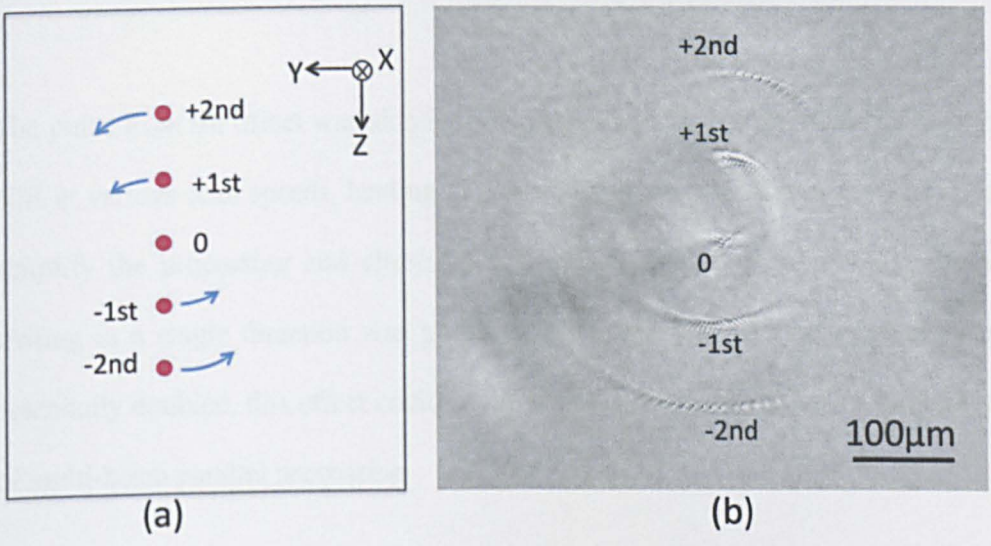

Fig. 4.3-6: (a) Schematic of 5 beams including 0, ±1st and ±2nd order dynamic structuring of fused silica. The blue arrows indicate the rotation direction of the beams. (b) Micrograph of the modified region.

4.4. Summary

Long filaments and multiple foci generated in bulk PMMA by 1 kHz, 775 nm and 387 nm femtosecond laser pulses were investigated. Filaments developed towards

the incident radiation direction as pulse energy was increased, when femtosecond laser pulses were focussed by a low NA (~ 0.04) objective into PMMA. The step-like damage structures, which indicated more than ten times refocussing, were clearly observed when the PMMA sample was irradiated by NUV laser pulses at 1 μJ pulse energy during 0.5 s exposure time. The dependence of filament length on laser pulse energy was measured and compared with the theoretical model [225]. NUV results fitted the model well while NIR results agreed only at the highest pulse energies, possibly related to the order of nonlinearity.

The pulse front tilt effect was also investigated in PMMA for the first time in the NIR at various scan speeds, leading to a remarkable modification asymmetry. To simplify the processing and eliminate the undesired writing asymmetry, direct writing in a single direction was proposed. Although the processing speed was essentially doubled, this effect could be compensated for and improved on the use of multi-beam parallel processing.

Optical components and other structures were generated using a single beam and multiple beams with 2D and 3D, static and dynamic direct writing techniques, which provided the basis for fabrication of more complex devices.

Chapter 5 - NIR multiple laser beam parallel writing of volume Bragg gratings

5.1. Introduction

In this chapter, parallel femtosecond refractive index laser inscription of clinical grade PMMA at 775 nm, 170 fs pulse duration is demonstrated with multiple low fluence beams generated with the aid of a spatial light modulator. Using optimised CGHs (see Section 3.5.2 and Section 4.3.1), 16 diffracted near identical beams were focussed simultaneously within bulk PMMA to create a series of 19 μm period, 5 × 5 × 1-4 mm^3 thick volume phase gratings at high speed. A high quality NIR Nikon objective (Nikon, CFI LU Plan Fluor BD 5×, 0.15 *NA*, f = 40 mm, *WD* = 18 mm) was used with an effective $NA \approx 0.1$. Great care was taken in aligning the incoming beam with the longitudinal X-axis of the 3-axis stage system and the optic axis of the objective was carefully adjusted to be collinear with the stage y-axis. PMMA substrates, with dimensions 30 × 30 × 5 mm^3 and optically polished on all sides were attached to a precision mirror mount bolted to the vertical stage. The front interface was tilted and brought normal to the optic axis using retro-reflection back to a pinhole. First order diffraction efficiency rises with grating thickness in accord with diffraction theory, reaching 75% at the first Bragg angle (4 mm thick) with fabrication time ~ 1 hour. By carefully stitching filamentary modifications while eliminating effects such as pulse front tilt during inscription, gratings were shown to exhibit high uniformity, which has not been achieved previously using femtosecond inscription. Highly uniform modification was exhibited throughout the material consistent with the observed excellent angular selectivity and low background scatter and quantitative comparison with first order diffraction theory is satisfactory. The diffraction efficiency and hence refractive index profile showed a temporal behaviour related to the material

response after exposure. Raman spectroscopy was employed in order to analyse the refractive index modulation.

5.2. Direct writing of volume gratings at NIR wavelength

Using the optimisation method described in Section 3.5.2 and Section 4.3.1 to improve multi-beam uniformity, 16 nearly uniform beams were scanned transversely inside PMMA to produce refractive index modification with pulse energy E_p = 0.6 μJ/beam. The modified regions (4 μm wide) had filaments $l \approx$ 109.9 ± 6.1 μm (1σ) in depth (see Fig. 4.3-1(b)), while the calculated depth of focus was $DOF \approx 34$ μm ($n_0 = 1.49$, $M^2 \approx 1.3$) so that the effect of self-focussing and filamentation is significant. This is not surprising as the peak power $P \approx 4$ MW is much high than the critical power for self-focussing in PMMA (see Section 4.2.1) [80]. The relatively long modification depth is due to the dynamic balance between Kerr self-focussing and the defocussing effects of the electron plasma generated during the ionisation process. A recent study by Watanabe et al. demonstrated refractive index filaments created in PMMA with 100 fs, NIR, 1 kHz pulses and 0.1 *NA* objective had length $l \approx 200$ μm at 0.8 μJ pulse energy [152]. By scanning this 16 beams optimised intensity distribution in the transverse (+*Y*) direction with *Z*-axis increments, ΔZ = 304 μm (16 × 19.0 μm), while offsetting in the axial (*X*) direction with ΔX of ~ 100 μm (deepest first) (see Fig. 3.4-5), a thick grating (35 layers) with dimensions of 5 × 5 × 3.5 mm^3 was created in about 50 minutes (see Fig.5.2-1). The offset was chosen to give a ~10% overlap of filaments in order to create a continuous modification along the X-axis. A

synchronised fast mechanical shutter ($\tau_r \approx 3$ ms) controlled from within the motion control software avoided unwanted exposure of material. Fig.5.2-1(b) shows a cross-sectional view of the volume grating, indicating the continuous and uniform modifications.

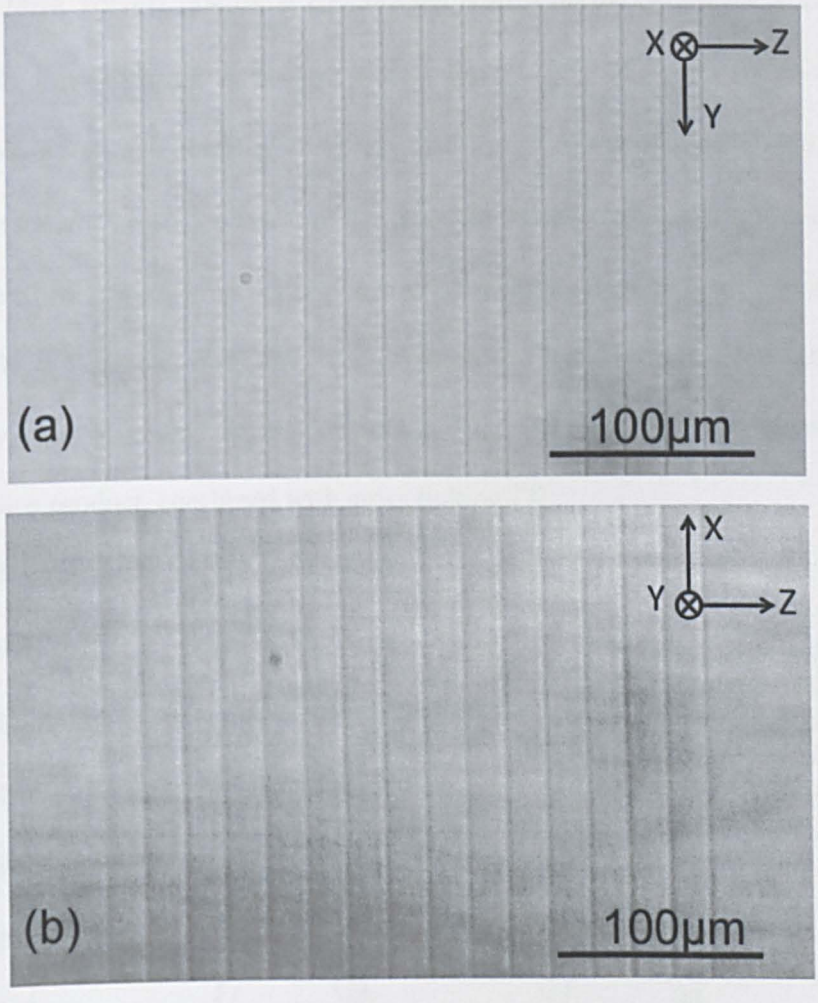

Fig. 5.2-1: (a) Front view and (b) cross-sectional view of a volume grating written with 16 parallel beams using asymmetric spot pattern with slight displacements along the X-axis. The volume grating consists of 35 layers with offsets $\Delta X = 100$ μm (10 μm overlaps) to create continuous modification and no discontinuities can be detected. The laser beams propagate along the +X direction, and the sample translation direction is in the +Y direction.

5.3. Diffraction efficiency and refractive index change measurements

Fig. 5.3-1 shows the $\pm 1^{st}$ order angular diffraction efficiency η measured for the 3.5 mm thick volume grating at λ = 532 nm over a period of 7 days. Diffraction efficiency η peaks at the first order Bragg angle θ_b = 0.813°, in agreement with that expected at $\theta_b = \pm\arcsin(\lambda/2\Lambda) = \pm 0.802°$ (λ = 532 nm, Λ = 19.0 μm). The grating efficiency also showed a remarkable time dependence, with η rising from 22% after one hour to ~ 36% after 12 hours, reaching η_{max}= 66% after almost one week. This suggests that the material modifies and relaxes after exposure, possibly due to diffusion of monomer MMA molecules, the most likely breakdown product, combined with cross linking [7].

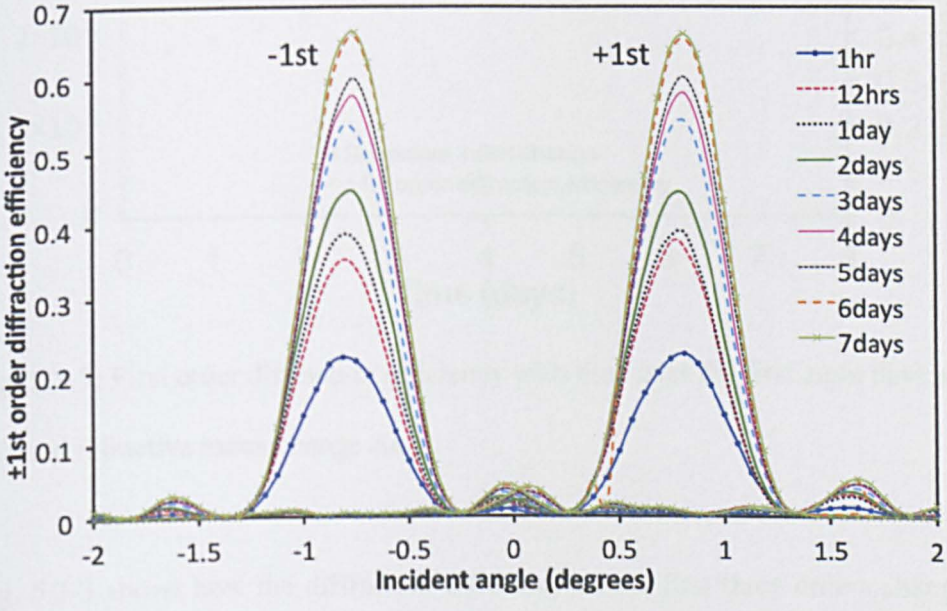

Fig. 5.3-1: First order diffraction efficiency of a 19 μm period, 5 × 5 × 3.5 mm^3 volume grating measured over 7 days written by 16 beams with asymmetric pattern at λ = 775 nm, with 0.15 NA objective.

The grating structure here is of high quality, shown by the extremely low background scatter. The diffraction efficiency with time of the first order and the calculated refractive index change Δn is shown in Fig. 5.3-2. After 7 days, the refractive index change reached a maximum at $\Delta n_{max} = 4.6 \times 10^{-5}$, according to Kogelnik theory **[160]**. Δn is modest but not unexpected at the pulse duration of 170 fs at $\lambda = 775$ nm with a single scan and high diffraction efficiency here has been achieved as a result of the structural uniformity and the large thickness of the grating.

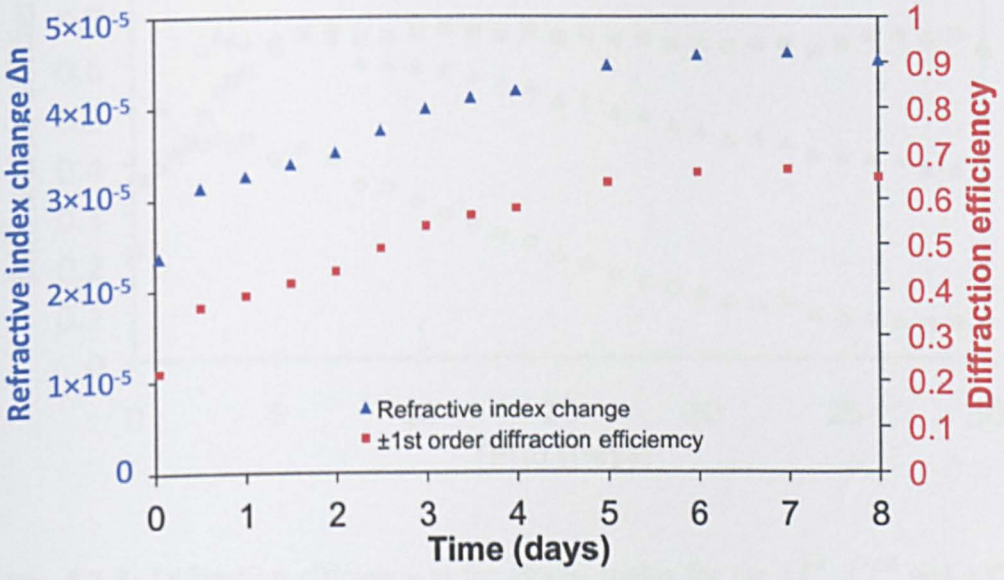

Fig. 5.3-2: First order diffraction efficiency with time over the first eight days and inferred refractive index change Δn.

Fig. 5.3-3 shows how the diffraction efficiency of the first three orders changes over a period of 30 days. Even though the first order has stabilised after 7 days, the second and third orders diffraction efficiencies, peaking after 4 days, continue to fall. The inference is that the Δn modulation is altering both temporally and

spatially as the MMA molecules diffuse out into the unexposed regions between the grating lines. There is clearly a question over the long term stability of volume gratings written in clinical grade PMMA with 170fs long laser pulses. More stable structures can be expected at shorter pulse duration $\tau \approx 100$ fs in the NIR where multi-photon ionisation increases relative to impact ionisation or at shorter NUV wavelengths [7, 93].

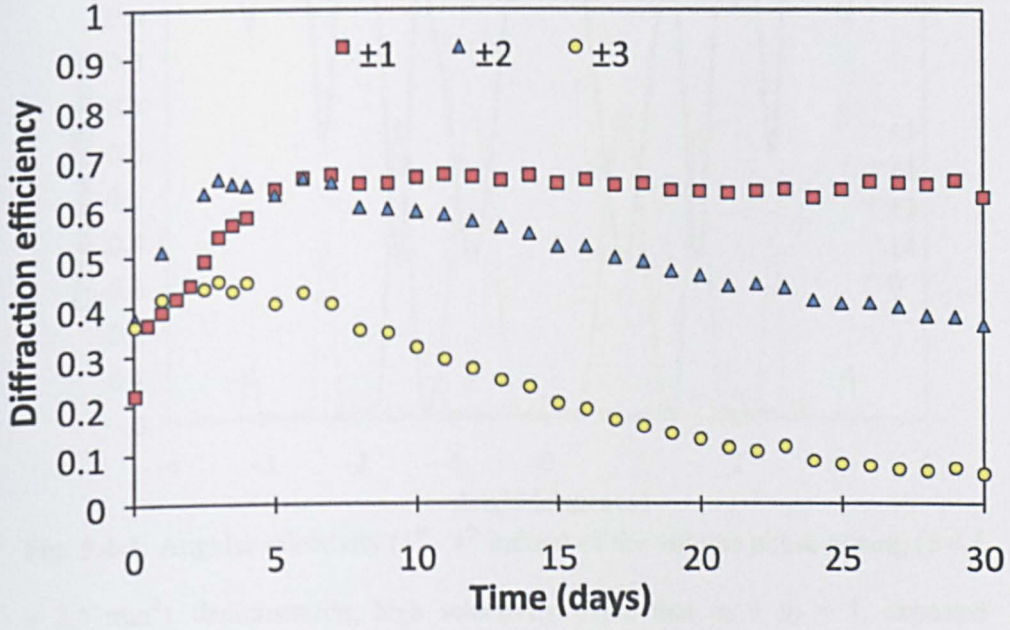

Fig. 5.3-3: Diffraction efficiency at the Bragg angles for the $\pm 1^{st}$, $\pm 2^{nd}$ and $\pm 3^{rd}$ orders showing temporal behaviour over a period of 30 days.

Watanabe et al. [228], while creating 3D directional couplers in PMMA using 1 kHz, 85 fs pulses at 800 nm, observed temporal changes in waveguide cross-sections, indicating that refractive index profile in the central region altered over a period of ~ 20 minutes after irradiation, with the refractive index change Δn going from negative to positive and reaching a maximum value of $\sim 4.6 \times 10^{-4}$.

5.4. Angular selectivity analysis

According to Eq. 2.1, gratings with thickness $1< L < 4$mm infers that the grating thickness parameter, Q, is in the range of $6.3 < Q < 21.9$, so that gratings ($Q > 10$) are thick volume gratings [162, 163] and hence should show a high angular selectivity.

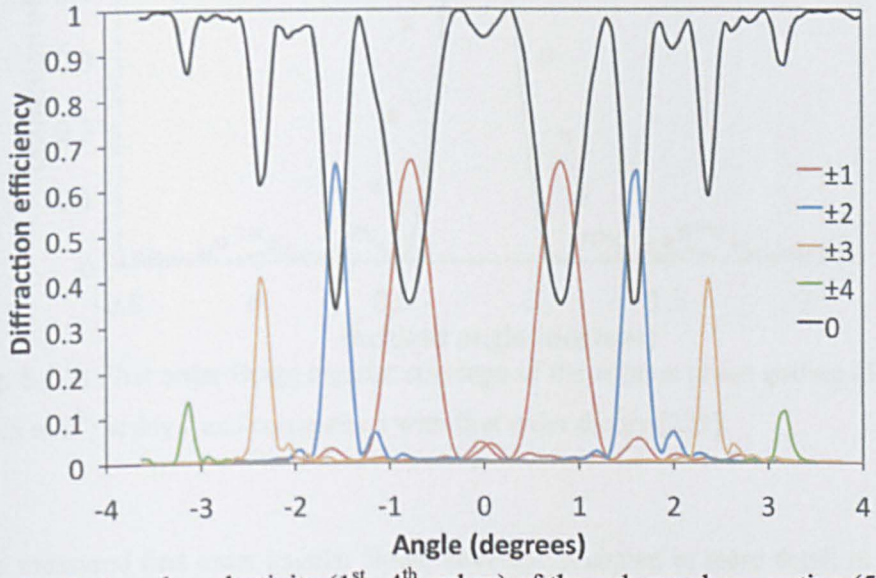

Fig. 5.4-1: Angular selectivity (1^{st} - 4^{th} orders) of the volume phase grating (5 × 5 × 3.5 mm^3), demonstrating high selectivity. Note that $\eta_0 + \eta_1 = 1$, expected theoretically for thick grating.

The measured angular diffraction efficiency $\eta(\theta)$ at $\lambda = 532$ nm (Coherent Verdi) 7 days after exposure is shown in Fig. 5.4-1 and Fig. 5.4-2 ($L = 3.5$mm, first order). The peaks appear close to the calculated Bragg angles $\theta_b = \arcsin(m\lambda/2\Lambda)$ $= 0.80°$ ($m = 1$, experimental Bragg angle $\theta_{b(exp)} = 0.81°$), $1.60°$ ($m = 2$), $2.41°$($m = 3$) and $3.21°$($m = 4$), where m is the order of diffraction. The symmetrical response is very satisfactory. The intensity drop measured in the zero order is also

shown for comparison in Fig. 5.4-1, demonstrating that coupling from zero order to any given order is highly selective.

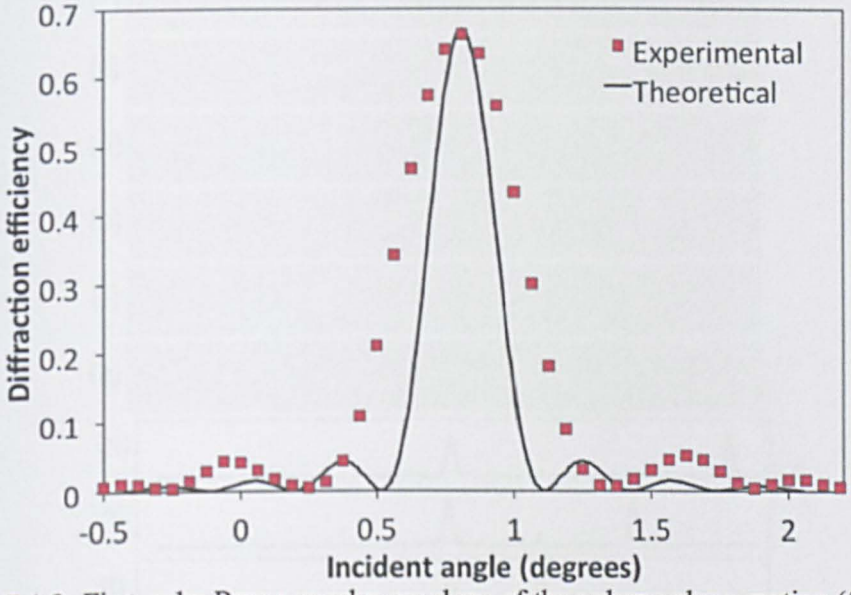

Fig. 5.4-2: First order Bragg angular envelope of the volume phase grating (5 × 5 × 3.5 mm^3) at day 7 and comparison with first order theory [229].

The measured first order angular Bragg envelope is shown in more detail in Fig. 5.4-2 (L = 3.5 mm) and compared with the theory used with thick holographic volume phase gratings (Equation: $\eta(\theta) = \frac{sin^2\left(\pi L\left((\Delta n/\lambda)^2+(\Delta\theta/\Lambda)^2\right)^{\frac{1}{2}}\right)}{1+(\lambda\Delta\theta/\Lambda\Delta n)^2}$) [229]. The theory gives an expected half width $\Delta\theta_{FWHM} \approx \Lambda/L \approx 0.31°$ while the measured FWHM $\Delta\theta_{FWHM(exp)} = 0.47 \pm 0.02°$, a factor of 1.5 wider.However, the general curve with side lobes is well reproduced. Holographic gratings have a harmonic refractive index modulation $\Delta n = \Delta n_0 \cos(2\pi z/\Lambda)$ while the index modulation profile here must be quite different from sinusoidal. The second order provides higher resolution with $\Delta\theta_{FWHM(exp)} = 0.24 \pm 0.01°$, as expected.

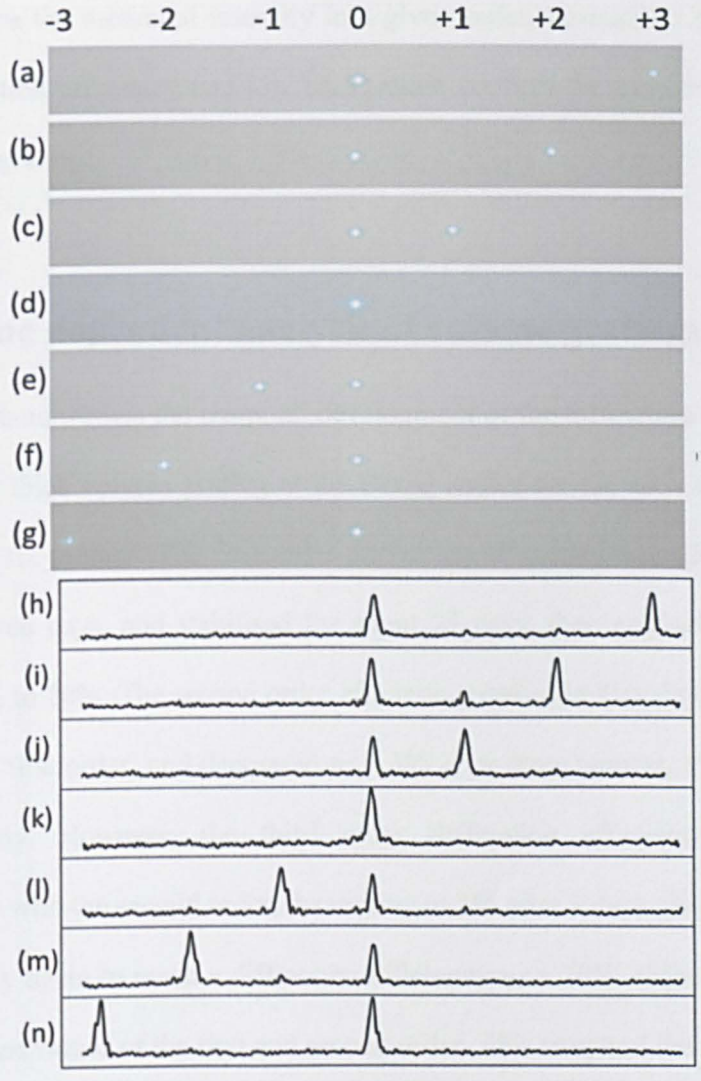

Fig. 5.4-3: (a-g) Composite image of Bragg diffraction at $\lambda = 532$ nm (a) +3rd to (g) -3rd order of the thick volume grating, (h-n) the relative intensity of measured peaks. Background scatter is very low. Note the fidelity of coupling into given orders.

Figure 5.4-3(a–g) shows a photographic image of the diffracted spots when projected on a distant screen as the volume grating was rotated while Fig. 5.4-

3(h–n) shows the measured intensity in a given order, normalised to scale. The high diffraction efficiency and low background confirm the excellent quality of the volume grating.

5.5. Time dependent analysis of volume gratings (NIR)

Fig. 5.6-1 demonstrates the temporal development of the diffraction efficiency of the 3.5 mm thick volume grating at the Bragg angles for the $\pm 1^{st}$, $\pm 2^{nd}$ and $\pm 3^{rd}$ orders over six months. The first order diffraction efficiency increased rapidly in the first seven days, and stabilised for about 25 days, then gradually decreased from ~ 66% to 20%. The second order efficiency peaked in four days at the same level as the first order, and decreased to ~ 5% after three months, then increased again slowly. However, the third order diffraction efficiency peaked in coincidence with the second order, decreasing to 5% after 3 days, then remarkably rises steadily again to reach a diffraction efficiency $\eta_3 > 70\%$, higher than that of the maximum values of the first and second order. This temporal development has a number of sources. The primary photochemical product is monomer MMA [7], which can diffuse out into the unexposed regions between the grating lines. Monomer present in the bulk reduces the refractive index there. In exposed regions, cross-linking, which increases Δn, can also occur so that the Δn modulation alters both temporally and spatially. Stress relaxation may also be important over this timescale. However, the mechanism behind the significant variations of the second and third order diffraction efficiency is still under investigation.

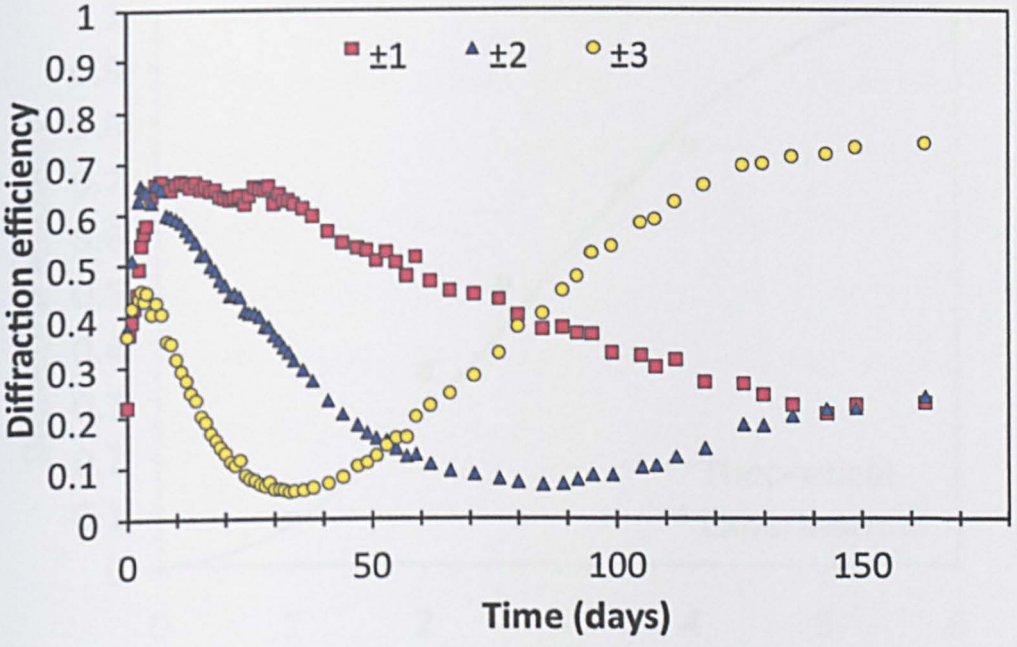

Fig. 5.5-1: Temporal development of the ±1st, ±2nd and ±3rd orders diffraction efficiency over a period of six months for the 3.5 mm thick volume grating written with 16 NIR parallel beams at 775 nm.

5.6. Thickness dependence of volume gratings

The expected first order diffraction efficiency can be estimated from $\eta_{\pm 1} = \sin^2(\pi \Delta n_0 L/\lambda \cos\theta_b) = \sin^2\varphi$ where Δn_0 is the amplitude of modulation and θ_b is the first order Bragg angle [160]. A graph of the measured diffraction efficiency of a series of gratings written under identical conditions with increasing thickness is shown in Fig. 5.5-1 and compared with the expected $\sin^2\varphi$ function. Highest diffraction efficiency, η_b = 75% was observed at 4 mm thickness. The fit is consistent with a $\Delta n = 4.6 \times 10^{-5}$. This experimental curve (Fig. 5.5-1) is consistent with a highly uniform modification throughout the depth of the volume grating.

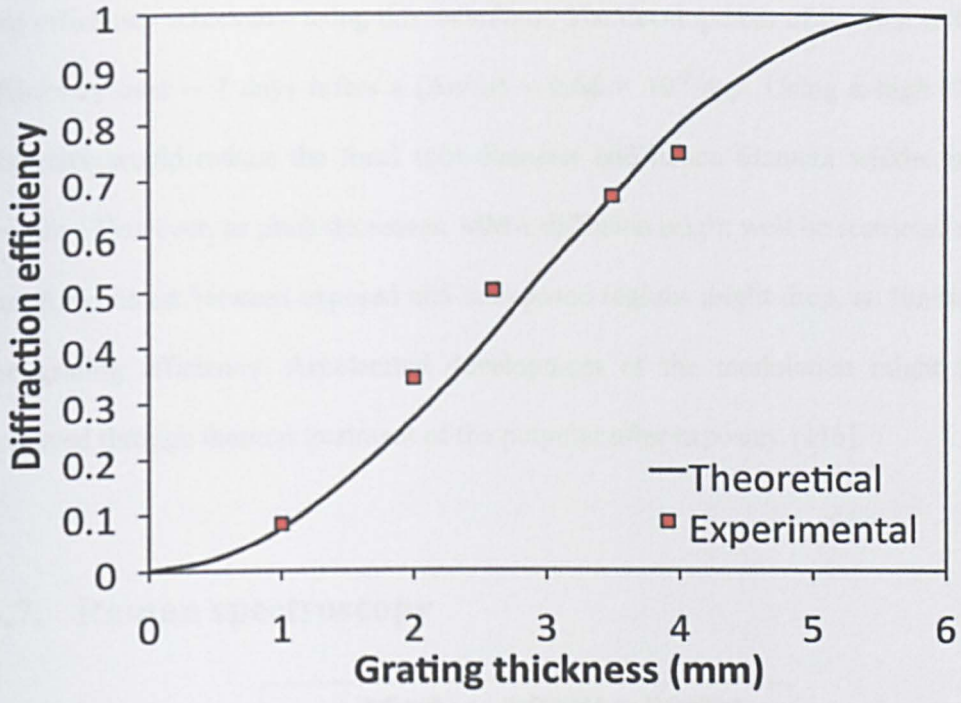

Fig. 5.6-1: Diffraction efficiency of a series of gratings of varying thickness and comparison with first order theory, $\eta = \sin^2\varphi$ [160]. The inferred refractive index modulation from this fit is 4.6×10^{-5} and the experimental curve confirms highly uniform modification with depth.

Using the technique demonstrated here, the maximum spatial resolution will be limited by the filament widths, measured here to be ~ 4 μm, so that a pitch below $\Lambda < 8$ μm (i.e. > 125 lines/mm) is unlikely with this material and geometry. Up to 30 beams were diffracted simultaneously, however, at the cost of intensity uniformity with the calculated CGHs. While grating thicknesses (through stitching filaments) of up to 4 mm have been demonstrated (40 layers) a slight reduction in the filament length (~ 10%) was observed with thickness greater than 3.5 mm in PMMA. This factor may well limit the maximum thickness, uniformity

and efficiency achievable using this technique. The development of the first order efficiency over ~ 7 days infers a $(\Delta n/\Delta t) \approx 0.66 \times 10^{-5}$/day. Using a high NA objective would reduce the focal spot diameter and hence filament widths and lengths. However, as pitch decreases, MMA diffusion might well be restricted so that Δn contrast between exposed and unexposed regions might drop, so limiting the grating efficiency. Accelerated development of the modulation might be achieved through thermal treatment of the polymer after exposure [116].

5.7. Raman spectroscopy

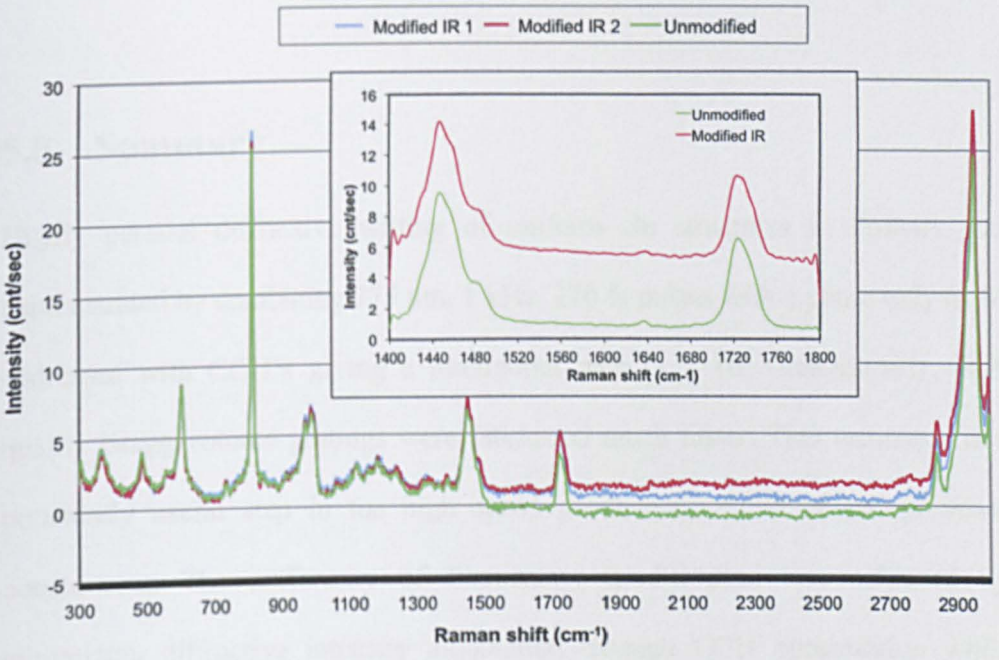

Fig. 5.7-1: Raman spectrum of laser modified and unmodified PMMA at 632.8 nm at wavenumbers between 300 and 3000 cm^{-1}. Insert: Raman spectrum at wavenumbers between 1400 and 1800 cm^{-1}. There is no obvious signal difference between the modified and unmodified regions.

Fig. 5.7-1 shows the Raman spectrum of laser modified and unmodified regions inside a PMMA sample at wavenumbers between 300 and 3000 cm^{-1} with a Raman excitation wavelength of 632.8 nm. No obvious difference between the modified and unmodified regions could be observed. One possible reason for this is that the concentration of unsaturated C=C bonds induced under NIR exposure is too low to detect. The other reason may be that weak signals are caused by large focal spots from low NA objectives. Because the modified structures were located ~ 500 μm below the surface, only low NA objectives could be employed. The focal spot size of the Raman objective used were larger than the width of modified regions (~ 4 μm), generating low signal strength.

5.8. Summary

Highly parallel diffractive writing of uniform Δn structures in PMMA was demonstrated by combining 775 nm, 1 kHz, 170 fs pulses with a phase only SLM addressed with CGH's giving a throughput gain G = 16, Consequently, high quality Bragg volume gratings were fabricated much faster. This technique is a potentially useful step in the high speed production of 3D optical photonic components. The uniformity of filamentary modification was achieved by minimizing diffractive intensity modulation through CGH optimisation while limiting filamentary modifications to ~ 110 μm lengths at NA = 0.1, then carefully overlapping axial filaments to produce a continuous modification. In addition, the asymmetry due to pulse front tilt was eliminated by inscribing in a single direction only. Consequently, thick, high quality volume phase gratings (5 × 5 mm^2, 53

lines/mm) with up to 4 mm thickness and η_b = 75% first order diffraction efficiency have been produced at high speed. The measured Bragg angular envelope is similar but wider by a factor of 1.5 when compared to first order theory while the diffraction efficiency with grating thickness increases with the expected $\sin^2\varphi$ function [160], consistent with a refractive index modulation $\Delta n_0 \approx 4.6 \times 10^{-5}$. Temporal changes in refractive index are observed after material inscription, probably related to the primary photoreaction product, most likely monomer MMA which diffuses into the bulk over periods of days to weeks. Monomer present in the bulk reduces the refractive index there while exposed regions may also suffer cross linking, increasing the refractive index [230]. No obvious difference between the modified and unmodified regions could be observed by Raman spectroscopy.

Although the volume gratings written with NIR femtosecond beams demonstrated instability, this method for rapid fabrication of volume gratings can be easily adopted to process with shorter temporal pulse durations and wavelengths (see Chapter 6) and different optical materials, in which high quality permanent volume gratings can be inscribed.

Chapter 6 -NUV multiple laser beam parallel writing of volume Bragg gratings

6.1. Introduction

In this chapter, 3D parallel refractive index structuring at 387 nm, 170 fs inside PMMA is investigated. The arrangement used for this is to place a thin BBO non-linear crystal after an SLM, then apply CGHs to the SLM to create parallel diffracted beams at 775 nm then frequency doubled to 387 nm, which can then be focussed inside the substrate. This procedure, investigated for the first time, aims to open up parallel processing at NUV wavelengths where nematic liquid crystal devices are more sensitive to optical damage.

For a laser pulse duration of $\tau > 100$ fs in the NIR, the contribution of impact ionisation towards plasma density increases relative to multi-photon ionisation, thus reducing the damage threshold for optical breakdown [39, 93]. With pure PMMA at a pulse duration of 170 fs, the advantage of applying a NUV wavelength of 387 nm would be to reduce the order of the non-linear absorption from three to two photon [93]. Presently, no SLM based on nematic liquid crystals operates in the NUV (< 400 nm) due to photodegradation of the liquid crystal or the polymer alignment layer with such high photon energy. Thus, exposure at NUV wavelengths with high peak intensity risks irreparable damage and possible device failure. By placing a thin BBO nonlinear crystal immediately after an SLM addressed with CGHs, the first order diffracted NIR components at 775 nm here are converted to parallel NUV beams at 387 nm, avoiding this potential problem while simultaneously reducing the order of non-linear absorption for Δn structuring.

6.2. Conversion efficiency of the BBO

The maximum conversion efficiency of the BBO crystal from 775 nm to 387 nm was measured to be ~ 17% in the crystal ($8 \times 8 \times 0.5$ mm^3) with 375 μJ incident pulses ($I(\omega) = 1.13 \times 10^{10}$ W/cm^2), and the efficiency varies almost linearly with peak intensity (shown in Fig. 6.2-1), as expected [231]. The BBO conversion efficiency (Fig. 6.2-2) with linear polarisation indicates that the crystal acts also approximately as a polarisation analyser. The input laser polarisation direction ϕ_L at vertical ($\phi_L = 0°$ or 180°) can provide the highest BBO conversion efficiency.

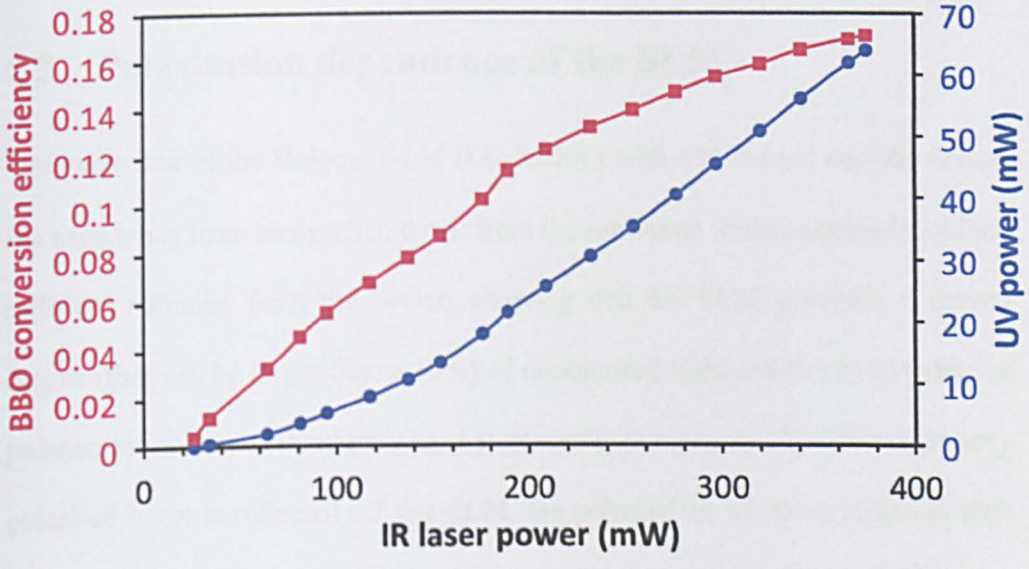

Fig. 6.2-1: BBO conversion efficiency (square) and the actual output NUV power (round) versus input NIR laser power.

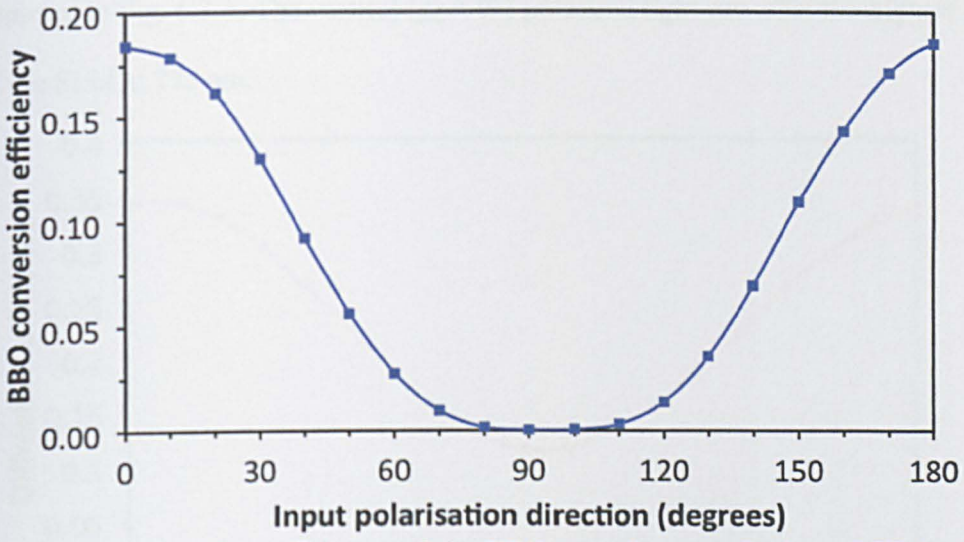

Fig. 6.2-2: Conversion efficiency of the BBO crystal versus the input NIR laser polarisation direction ϕ_L. The input polarisation rotates from vertical ($\phi_L = 0°$) to horizontal ($\phi_L = 90°$) in clockwise direction.

6.3. Polarisation dependence of the SLM

The behaviour of the Holoeye SLM (LC-R2500) with 45° twisted nematic crystal has previously been analysed in detail from the measured Stokes parameters of the reflected radiation from the device, showing that the SLM generates a certain degree (that can be larger than a 10%) of depolarised light and the output state of polarisation with addressed grey level is generally complex [232]. When a linearly polarised beam is reflected off this SLM, the polarisation becomes elliptical with a complex CGH applied. The intensity modulations and inferred polarisation behaviours of the SLM are shown in Appendix A.

When an optimised CGH (see Section 3.5.2) creating 18 diffracted beams is applied to the SLM, the measured diffraction efficiency, η, of the SLM at 775 nm (before the crystal) as a function of the input linear polarisation direction is

depicted in Fig. 6.3-1. The vertical ($\phi_L = 0°$) polarised light can offer the highest η of the SLM at 775 nm.

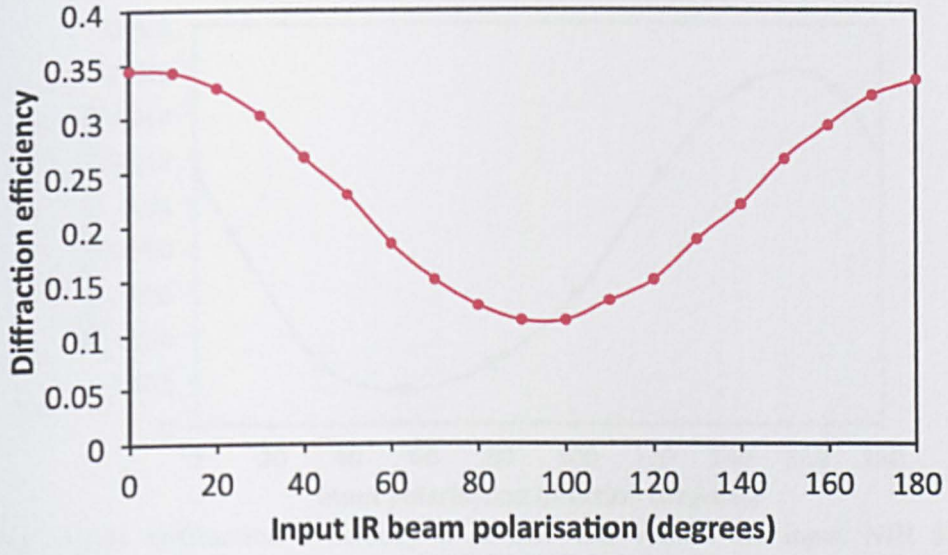

Fig. 6.3-1: Diffraction efficiency η of SLM at 775 nm versus the input NIR laser polarisation direction ϕ_L, when the CGH generating 18 beams is applied. The input polarisation rotates from vertical ($\phi_L = 0°$) to horizontal ($\phi_L = 90°$) in clockwise direction.

6.4. Characterisation of the SLM/BBO combination

The intensity modulations and inferred polarisation behaviours of the SLM/BBO combination are shown in Appendix B. When the same CGH is applied and the extraordinary axis of the BBO crystal, ϕ_C, is vertical ($\phi_C = 0°$), the diffraction efficiency at 387 nm (after the crystal) versus the input linear polarisation direction is illustrated in Fig. 6.4-1. A rotation to $\phi_L = 155°$ was required to provide the highest diffraction efficiency η at 387 nm because the reflected polarisation state from the SLM is elliptical before passing through the BBO crystal, and the crystal can only resolve the vertical field component. So, in the

following NUV parallel processing, the input polarisation direction $\phi_L = 155°$ and the crystal orientation $\phi_C = 0°$ were employed.

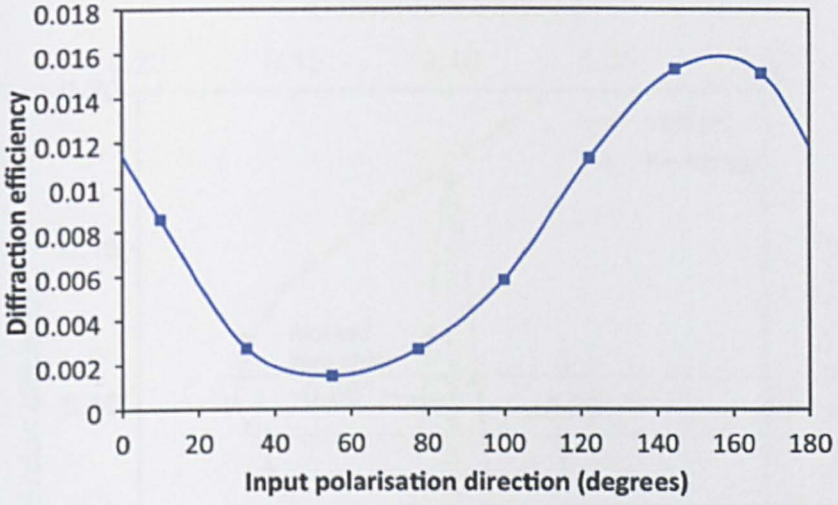

Fig. 6.4-1: Diffraction efficiency η at 387 nm versus the input NIR laser polarisation direction ϕ_L, when the CGH generating 18 beams is applied and $\phi_C = 90°$. The input polarisation rotates from vertical ($\phi_L = 0°$) to horizontal ($\phi_L = 90°$) in clockwise direction.

6.5. Phase matching technique

The conversion efficiency of the BBO crystal (with linear polarisation, $\phi_L = 0°$) and angular variation in the sensitive phase matching direction (horizontal) and azimuthal directions is shown in Fig. 6.5-1. As the FWHM (horizontal axis) $\approx$ 0.64° is much narrower than the FWHM (vertical axis) $\approx$ 2.36°, diffracted patterns with vertical symmetry are preferred in order to limit intensity modulation from phase angle mismatch. Hence, diffraction angles $< \pm 0.55°$ in azimuth are required to keep the intensity modulation between spots $\Delta I(2\omega)/I_0(2\omega)$ to < 5% below the optimum. By preferentially phase matching the diffracted spots of the vertical pattern rather than the zero order, the 387 nm remaining zero order was minimised

while simultaneously increasing the conversion efficiency of these first order beams.

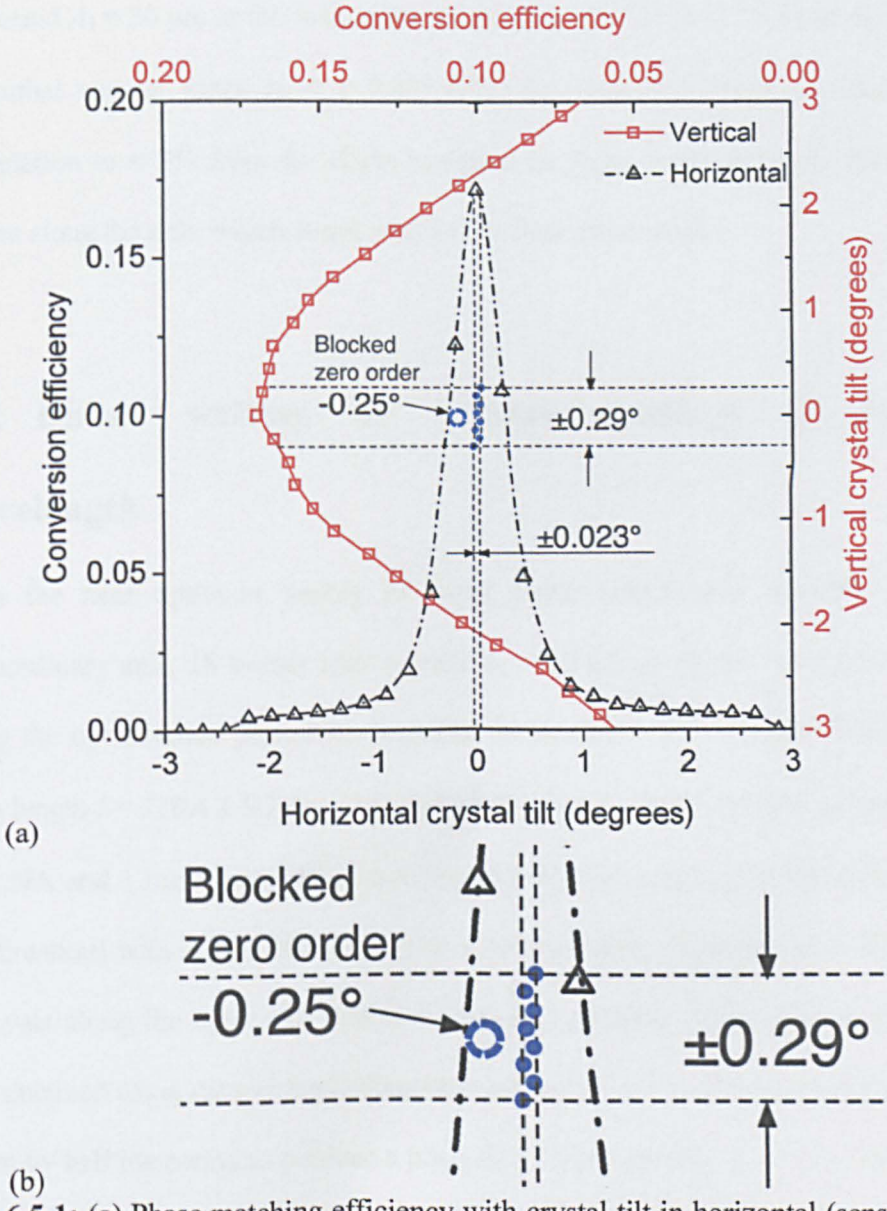

Fig. 6.5-1: (a) Phase matching efficiency with crystal tilt in horizontal (sensitive) and azimuthal (insensitive) axis, indicating that vertically diffracted spot patterns suffer much less intensity modulation. (b) Magnified view of the 18 spot phase matching. By tuning the crystal tilt, preferential phase matching minimised the zero order intensity, while maximising the 18 spots intensity and simultaneously avoiding intensity modulation.

A CGH, created within a Labview environment [233] (see Section 3.6) using the GS algorithm, generated 18 near uniform diffracted beams with a spot separation of around $\Lambda_1 = 30$ μm at the focal plane of the lens ($f = 50$ mm), limiting the total azimuthal angular range to $< \pm 0.29°$ (Fig. 6.5-1(b)) and hence the intensity modulation to < 3% from the slight variation in phase matching angle between beams along the axis, which is not sensitive to changes in angle.

6.6. Direct writing of volume gratings at NUV wavelength

With the near optimum setting of input linear polarisation and the BBO extraordinary axis, 18 beams with a pitch $\Lambda_1 = 30$ μm at 387nm were produced using the optimisation procedure described in Section 3.6.2. Modified filaments have length $l = 219.4 \pm 9.3$ μm (1σ) and width ~ 4 μm with $E_p = 0.21$ μJ/beam at 0.08 NA and 1 mm/s scan speed (see Fig. 6.6-1). By scanning in the horizontal (Y-direction) with offsets of 540 μm (18 × 30 μm) while offsetting $\Delta X = 200$ μm intervals along the optic axis (deepest first) a continuous, thick volume grating was obtained using the technique demonstrated in Fig. 3.4-5. The pattern was then offset by half the period to produce a pitch $\Lambda_2 = 15$ μm grating. A 5 × 5 × 2.0 mm^3 thick grating was fabricated in 18 minutes with the first order Bragg angle diffraction efficiency reaching $\eta_b \approx 70\%$ indicating $\Delta n \approx 8.4 \times 10^{-5}$, and the low scatter observed confirms that the quality of the grating is high (see Fig 6.6-2). The first order angular resolution, $\Delta\theta_{(FWHM)} \approx 0.63°$ is slightly higher than

expected, $\Delta\theta = \Lambda/L = 0.43°$ for a sinusoidal refractive index profile [160], while the second and third orders have $\Delta\theta \approx 0.33°$ and 0.23°, respectively.

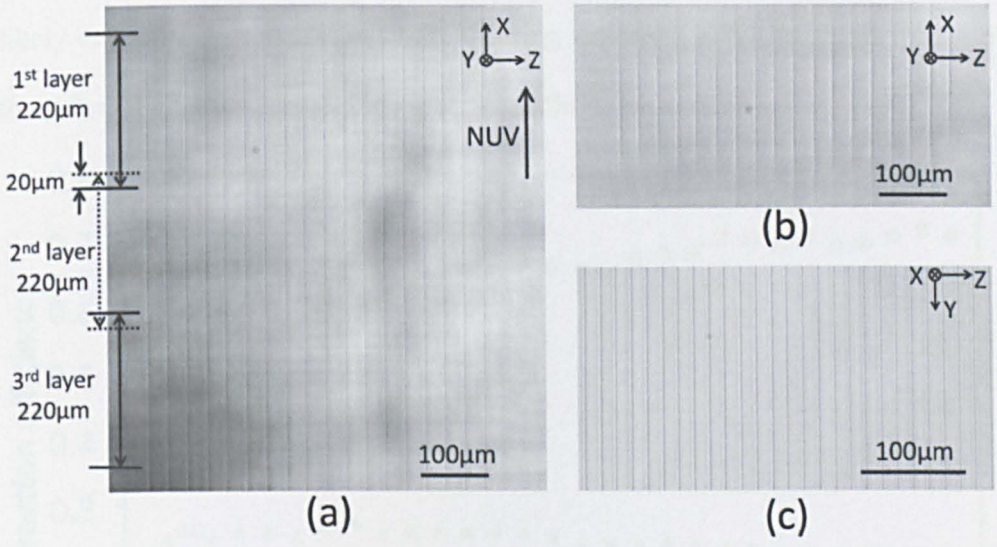

Fig. 6.6-1: (a) Continuously modified cross-section created by overlapping 3 layers each separated by $\Delta X = 200$ μm along optic axis. (b) Cross-section of 18 parallel beams modification of PMMA with $\Lambda_1 = 30$ μm. (c) Front view of a grating with $\Lambda_2 = 15$ μm pitch.

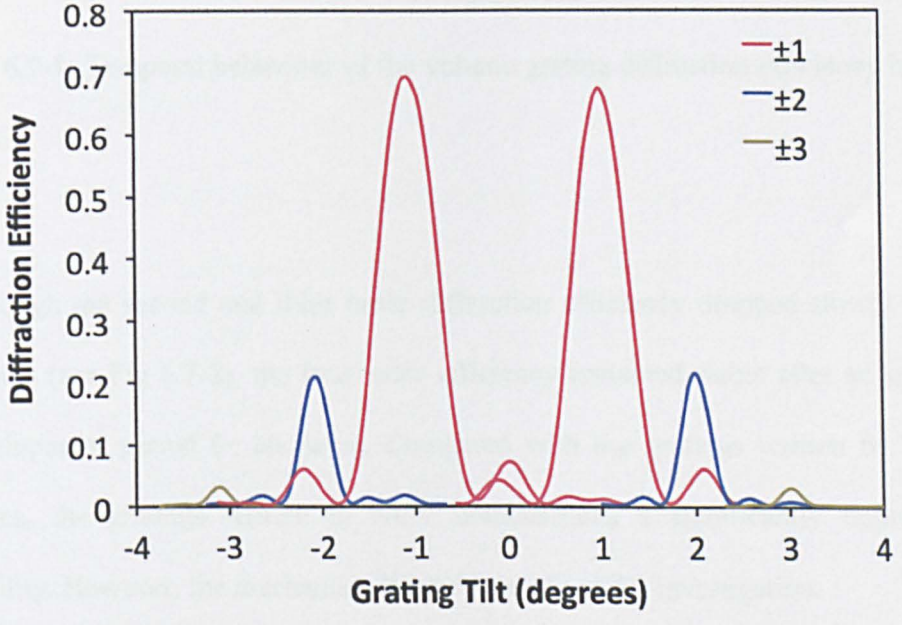

Fig. 6.6-2: Detailed measurements of the Bragg diffraction efficiency of ±1st, ±2nd and ±3rd orders after 30 days at 532 nm readout wavelength.

6.7. Time dependent analysis of volume gratings (NUV)

As shown in Fig 6.7-1, the temporal change, which stabilised after 20 days, is likely due to chain scission in PMMA during exposure, resulting in unzipping of the polymer chains to create the monomer, MMA, which diffuses out [230].

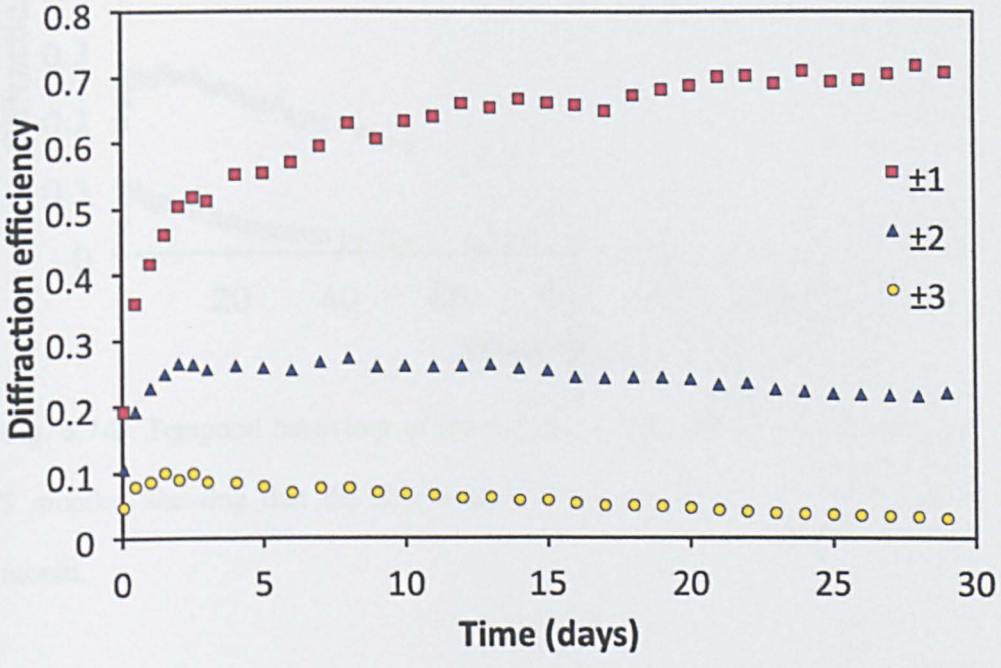

Fig. 6.7-1: Temporal behaviour of the volume grating diffraction efficiency in 30 days

Although the second and third order diffraction efficiency dropped slowly in 5 months (see Fig 6.7-2), the first order efficiency remained stable after an initial development period (~ 20 days). Compared with the gratings written by NIR beams, the gratings written in NUV demonstrated a significantly improved stability. However, the mechanism behind it is still under investigation.

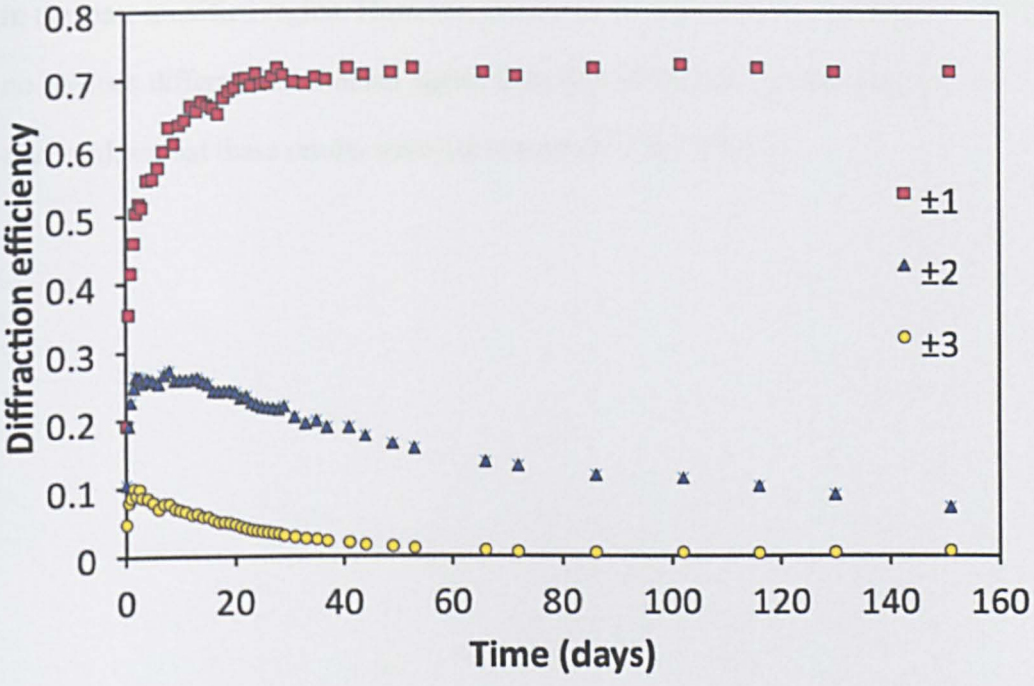

Fig. 6.7-2: Temporal behaviour of the volume grating diffraction efficiency over 5 months, showing that the first order diffraction efficiency is stable after 1 month.

6.8. Summary

Highly parallel NUV refractive index modification inside bulk PMMA was demonstrated at a wavelength of 387 nm and a pulse duration of 170 fs by placing the thin non-linear BBO crystal after the SLM addressed with CGHs to create parallel beams. An efficient Bragg grating with 15 μm pitch and dimensions 5 × 5 × 2.0 mm^3 with $\eta_b > 70\%$ at first order was created in 18 minutes with inferred $\Delta n \approx 8.4 \times 10^{-5}$. Optical measurements and long-term stability tests revealed the high quality and high stability of the volume gratings written by multiple NUV laser beamlets. Raman spectrometry was utilised to evaluate the photochemical changes

in the laser modified region. However, similar to the results shown in Section 5.7, no obvious difference in Raman signal from that of the unmodified material was observed, so that these results were not presented in this chapter.

Chapter 7 - Conclusions and recommendations for future work

7.1. Conclusions

This thesis is motivated by recent developments in femtosecond laser direct writing of high quality 3D photonic devices inside transparent materials. However, since most commercial femtosecond systems have pulse energy $E_p > 1$ mJ at 1 kHz, the light utilisation factor is < 0.1%. By using an SLM, addressed with appropriate CGHs to create a large number of diffracted beams of the requisite pulse energy, this efficiency was increased by more than an order of magnitude, reducing the fabrication time while allowing arbitrary parallel processing. A novel technique for rapid fabrication of volume gratings was established by focussing on control of filament length, optimisation of multi-beam uniformity, and elimination of pulse front tilt effect. This is the first study directly concerned with highly parallel femtosecond writing of high quality volume Bragg gratings in NIR and NUV, as a contributing step towards the high speed production of 3D optical photonic circuits. However, the main limitation of this technique at the present is that the line density is restricted to 125 lines/mm. The conclusions drawn from each of the investigations in this study are as follows.

7.1.1. Control of filament length

Long filaments and multiple foci generated in bulk PMMA by 1 kHz, NIR and NUV femtosecond laser pulses were investigated. Filaments developed towards the focussing lens with increasing pulse energy independent of wavelength. In the NUV, the periodic breakdown structures indicated more than ten times re-focussing occurred in PMMA when irradiated by femtosecond laser pulses at 1 μJ

pulse energy during 0.5 s exposure time. The dependence of filament length on laser pulse energy at both wavelengths were measured and compared to a theoretical model. The NUV modification was much more deterministic than that in the NIR.

7.1.2. Elimination of pulse front tilt effect

When a laser beam with pulse front tilt is used to write structures inside transparent materials in opposite directions, a change in material modification occurs as a result of anisotropic electron plasma trapping by a tilted pulse front along the writing direction. Pulse front tilt effect was investigated in PMMA. Since it is difficult to eliminate the pulse front tilt in the Clark-MXR system, direct writing in a single direction only was used to avoid the writing asymmetry. However, by doing so, the processing speed was affected, but was increased dramatically by introducing multi-beam parallel processing.

7.1.3. Improving multi-beam uniformity

The results in Section 4.3 demonstrated that the cross sections of modified structures written with a symmetric beam pattern showed a large variation in filament length $l = 106.2 \pm 26.3$ μm (1σ) emphasising the intensity non-uniformity generated with this geometry. Adding a slight random asymmetry in the spot pattern removed degeneracy and ghost beam overlap, reducing intensity modulation, hence structure quality improved markedly. The improved uniformity

of the induced structures with filament length l = 109.9 ± 6.1 μm (1σ) was obtained.

7.1.4. Direct writing of optical components

The results in Section 4.2.3 and Section 4.3.2-4.3.5 demonstrated a variety of refractive index structures generated using a single beam and multi-beam with 2D and 3D, static and dynamic direct writing techniques, which provided the basis for the fabrication of more complex photonic devices.

7.1.5. Direct writing of volume gratings using NIR multiple beams

Highly parallel diffractive writing of uniform Δn structures in PMMA was demonstrated by combining kilohertz femtosecond pulses with an SLM addressed with CGHs giving a throughput gain G = 16. The uniformity of filamentary modification was achieved by minimizing diffractive intensity variation through CGH optimisation while limiting filamentary modifications to ~ 110 μm lengths at NA = 0.1, then carefully overlapping axial filaments to produce a continuous modification. Consequently, thick, high quality volume phase gratings (5 × 5 mm^2, 53 lines/mm) with up to 4 mm thickness and η_b = 75% first order diffraction efficiency have been produced at high speed. The measured Bragg angular envelope is similar but wider by a factor of 1.5 when compared to first order theory while the diffraction efficiency with grating thickness increases with the expected $\sin^2\varphi$ function, consistent with a uniform modification with depth and a refractive index modulation $\Delta n \approx 4.6 \times 10^{-5}$. Temporal changes in refractive index

are observed after material inscription, probably related to the primary photoreaction product, most likely monomer MMA which diffuses into the bulk over periods of days to weeks. Monomer present in the bulk reduces the refractive index there while exposed regions may also suffer cross-linking, increasing the refractive index. Unfortunately, no obvious difference between the modified and unmodified regions could be observed by Raman spectroscopy due to inadequate sensitivity. Although the volume gratings written in PMMA with NIR femtosecond beams showed instability over long-term, the fabrication technique demonstrated a new approach towards rapid fabrication of efficient volume gratings.

7.1.6. Direct writing of volume gratings using NUV multiple beams

By placing a thin nonlinear BBO crystal after the SLM to create parallel beams at NUV 387 nm wavelength, 18-beam parallel refractive index modification inside bulk PMMA was demonstrated. Computer generated holograms applied to the SLM create parallel diffracted beams at 775 nm which were then frequency doubled to 387 nm and focussed inside the substrate. The behaviour of the SLM, the BBO crystal and the combination of these two devices were analysed in detail so that optimised phase matching could be conducted. This procedure, demonstrated for the first time, opens up dynamic parallel processing at NUV wavelengths where nematic liquid crystal devices are more sensitive to optical damage. An efficient Bragg grating with 15 μm period, dimension of 5 × 5 × 2.0 mm^3 and $\eta_b > 70\%$ in first order was created in 18 minutes with inferred $\Delta n \approx 8.4$

$\times 10^{-5}$. Optical measurements and long-term stability tests revealed that the volume gratings written by multiple NUV beams had excellent optical quality and high stability.

7.2. Recommendations for future work

7.2.1. Further optimisation of volume grating fabrication using an SLM

The technique for volume grating fabrication provides great flexibility, so that high quality gratings with specific parameters can be produced to meet the requirements in various applications. For example, the grating diffraction angle and the angular selectivity can also be tuned by changing the period of the grating. The grating diffraction efficiency can be further increased by increasing grating thickness. The high quality volume gratings written in the NUV and its high diffraction efficiency with only 2 mm thickness indicate it is possible to obtain gratings with $\eta_b > 95\%$ using the NUV multi-beam parallel processing, where refractive index modification occurs via 2-photon absorption, and optical breakdown is much less prevalent.

When writing a thick volume grating with a higher NA (> 0.2) objective, dynamic wavefront correction can be utilised to ensure uniformity of the grating. By integrate a camera into the beam delivery system to monitor the intensity of the multiple beams, real-time correction can be realised, hence, improving CGH optimisation process.

In this study, due to the availability issue, a twisted nematic LC SLM, Holoeye LC-R2500, was combined with a BBO crystal to implement NUV multi-beam processing. The laser polarisation state after reflected from the SLM was elliptical, which is not ideal for the subsequent frequency-doubling process. While a parallel aligned LC SLM, such as the Hamamatsu X10468-02, can overcome this problem. Hence, a combination of the parallel aligned LC SLM with the BBO crystal can be employed to further increase the throughput of the whole system.

Although the general mechanism of refractive index change inside PMMA has been studied by Baum at el. [7, 230], the mechanism behind the temporal development of the various diffraction orders over several months (See Section 5.5 and 6.7) is still unclear. Hence, long term time dependent optical tests combined with chemical analysis are suggested. Furthermore, temperature dependent measurements of the diffraction efficiency are also recommended.

7.2.2. Beam shaping to extend modification length

The author has reported beam shaping using axicon CGH with an SLM to generate annular beams for surface processing. A lens-axicon doublet shown in Fig. 7.2-1 can form not only an annular shape at the focal plane of the lens, but also a line focus along the optical axis, which is a Bessel region. This line focus has a significantly larger depth of focus, which can increase the modification thickness in internal structuring.

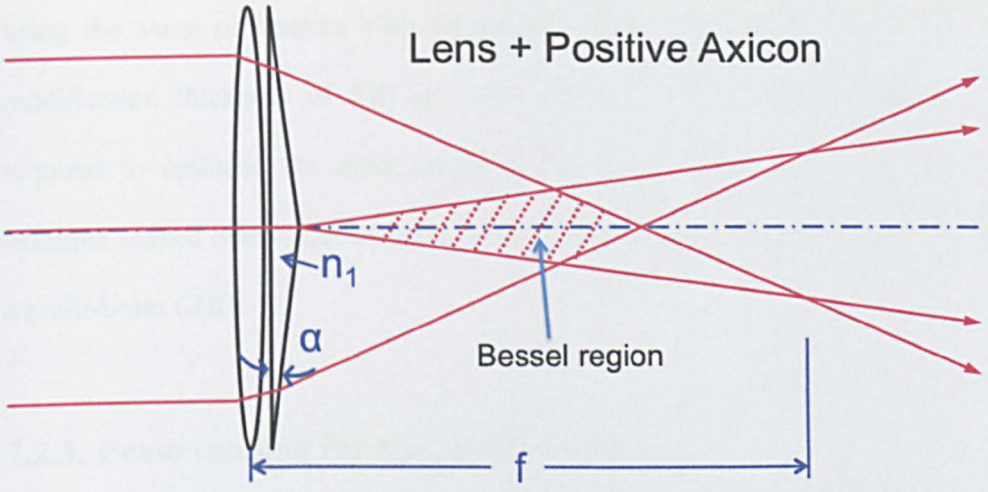

Fig. 7.2-1: Schematic of a lens-axicon doublet. An annular beam can be produced at the focal plane of the lens, and a line focus, Bessel region, can also be generated.

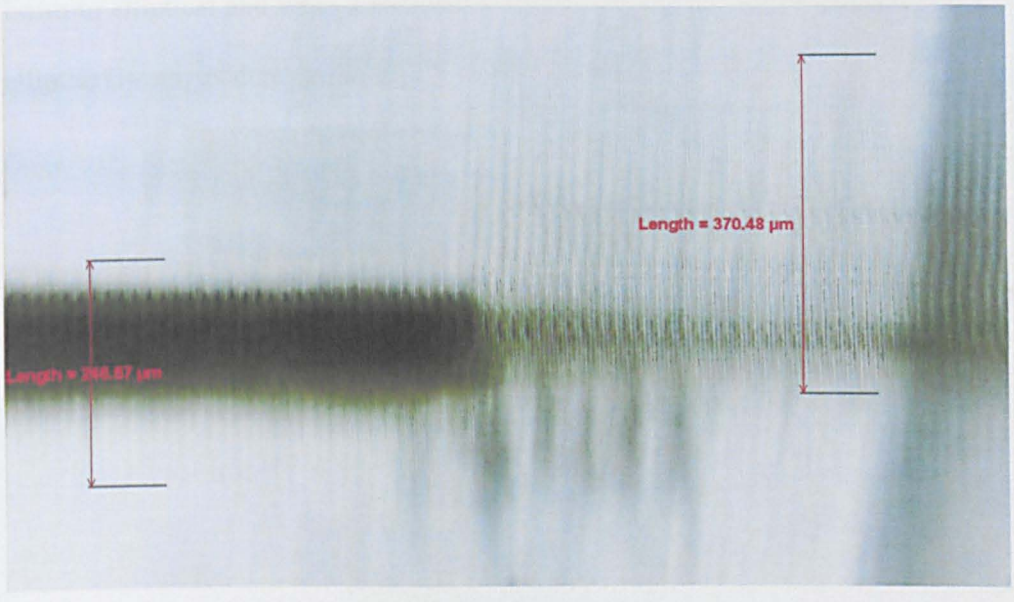

Fig. 7.2-2: A modification thickness of 247 µm (left) produced without beam shaping, and a modification thickness 370 µm (right) produced with beam shaping.

Preliminary test results (see Fig 7.2-2) show that a modification thickness of 247 µm was obtained (775 nm, E_p = 1 µJ, s =1 mm/s) with a 0.15 NA objective, while

using the same parameters with an axicon CGH displayed on the SLM, the modification thickness of 370 μm was achieved. Further improvements are required to optimise the axial intensity uniformity within the Bessel region. Multiple shaped beams can be generated by superimposing the axicon CGH with a multi-beam CGH.

7.2.3. Beam shaping for waveguide writing

Beam shaping to produce an elliptical beam (Fig 7.2-3(a)) for waveguide writing has been implemented with an SLM. A waveguide with a circular cross-section has been produced (Fig 7.2-3(b)). It is feasible to use an SLM to shape a laser beam to elliptical and write a waveguide with a curve by dynamically rotating the elliptical beam, as depicted in Fig 7.2-3(b).

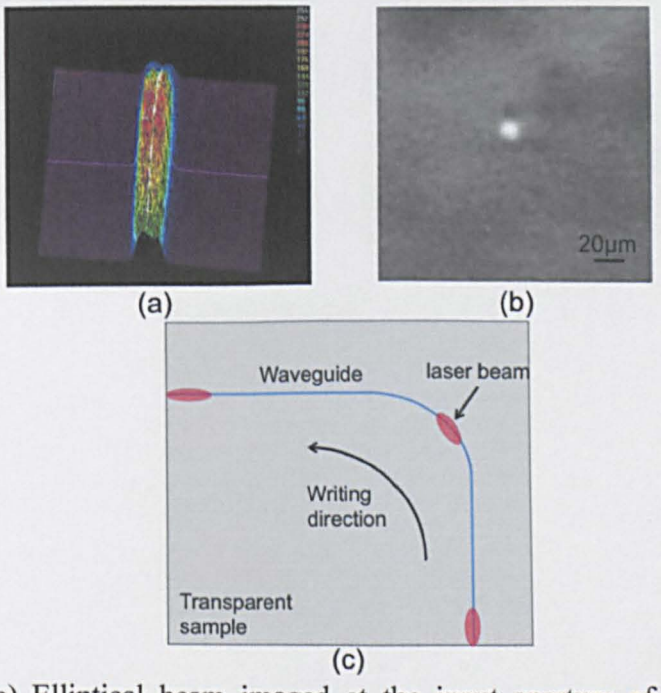

Fig. 7.2-3: (a) Elliptical beam imaged at the input aperture of the focussing objective. (b) Cross-section of a waveguide written with the elliptical beam shown in (a). (c) Schematic of dynamic writing a curved waveguide.

7.2.4. Beam shaping for material processing

As demonstrated in Fig. 7.2-4, laser beams with a variety of shapes has been produced with an SLM. A polarisation analyser was placed after the SLM to form an intensity mask setup. This beam shaping method can be employed in many laser processing applications.

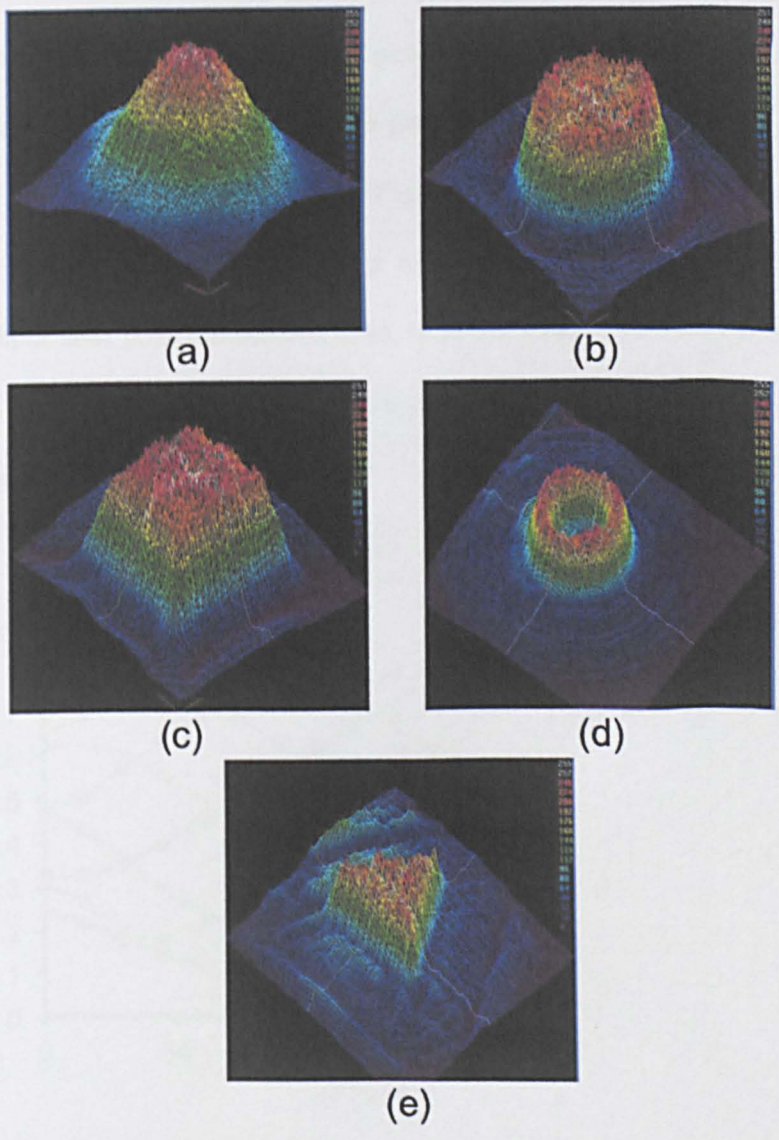

Fig. 7.2-4: (a) Original Gaussian beam and shaped laser beam profiles (b) Top-hat, (c) square Top-hat, (d) ring shape and (e) triangle shape.

Appendix A

Characterisation of the SLM with an analyser

As shown in Fig. 6.3-1, the Holoeye LC-R2500 SLM is sensitive to the polarisation direction of the input laser beam, and it provides the highest diffraction efficiency when the input polarisation is vertical. The polarisation behaviour of the SLM is analysed with a polarisation analyser placed directly after the SLM (without the BBO crystal). Fig. A-1, A-2 and A-3 demonstrate the intensity modulations of the SLM as a function of the addressed grey level at various input laser polarisation directions, indicating that slight depolarisation and elliptical polarisation were generated due to the 45° twisted nematic crystal structures.

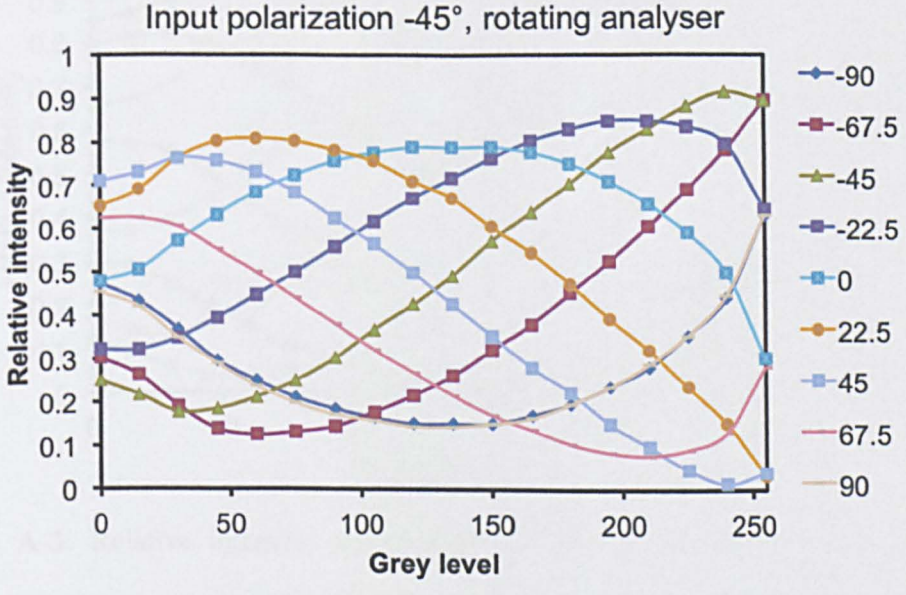

Fig. A-1: Relative intensity versus grey level (input laser polarisation -45°, different positions of the polarisation analyser).

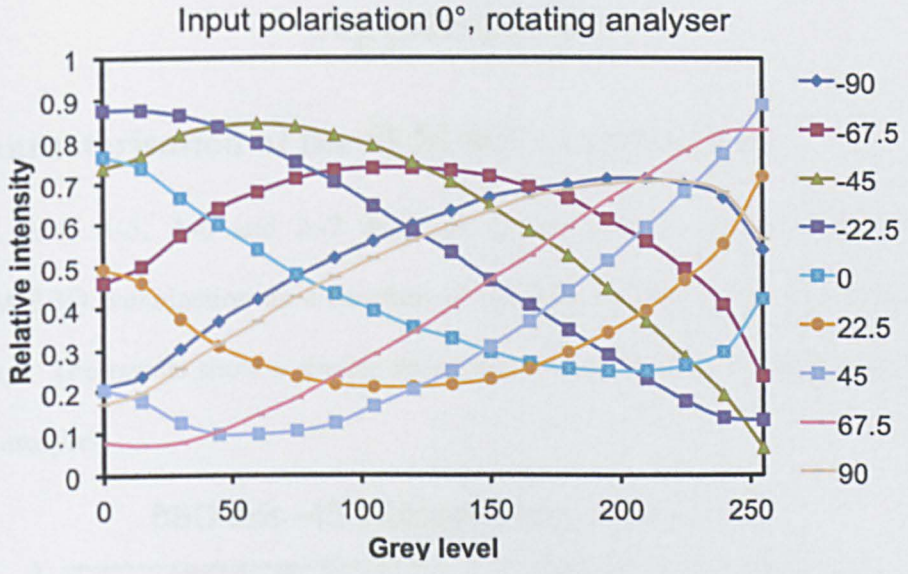

Fig. A-2: Relative intensity versus grey level (input laser polarisation 0°, different positions of the polarisation analyser).

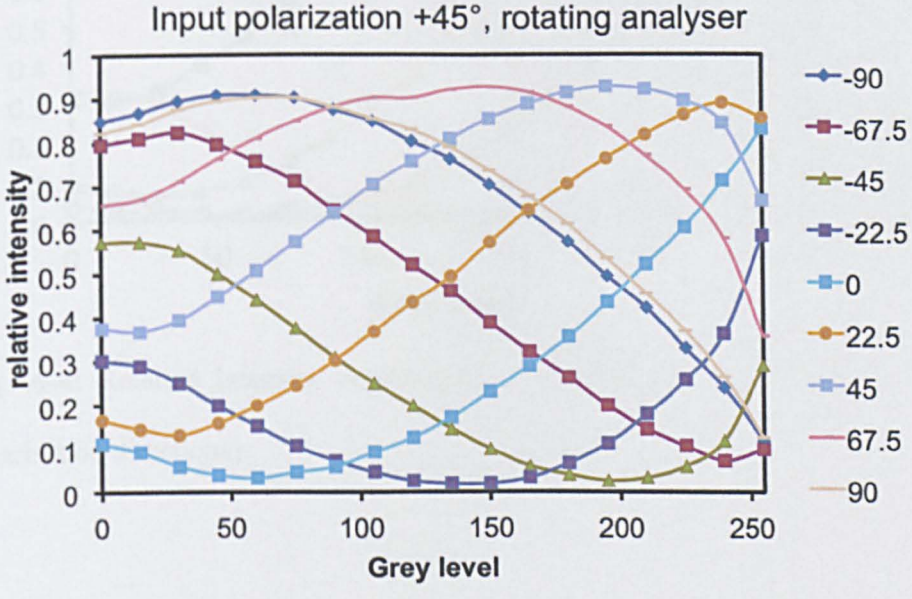

Fig. A-3: Relative intensity versus grey level (input laser polarisation +45°, different positions of the polarisation analyser).

Appendix B

Characterisation of the SLM/BBO combination

Fig. A-4, A-5, A-6 and A-7 demonstrate the intensity modulations of the SLM/BBO combination as a function of the addressed grey level with various setups. The results show a similar behaviour to that of the SLM combined with the analyser.

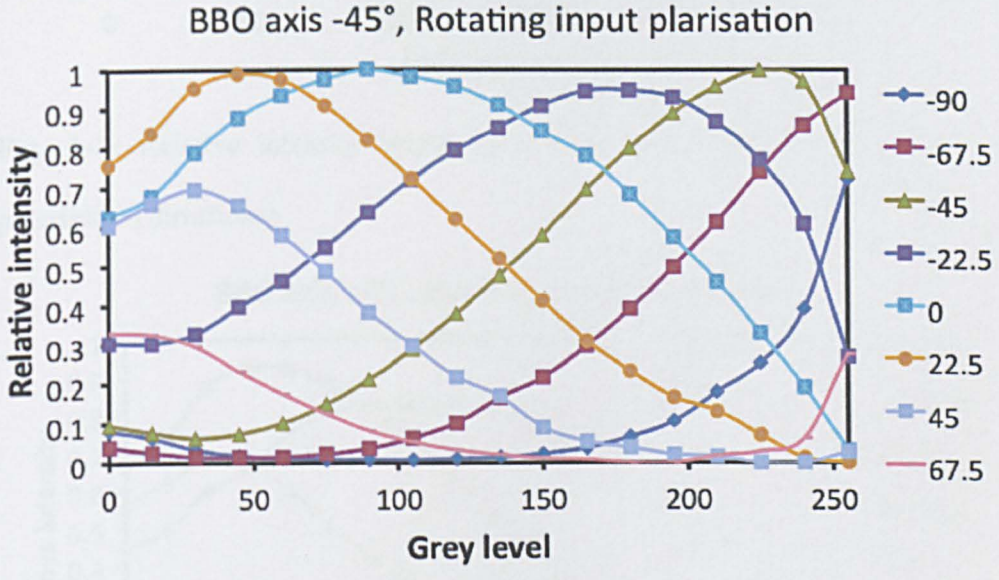

Fig. A-4: Relative intensity versus grey level (BBO axis -45°, various input polarisation directions).

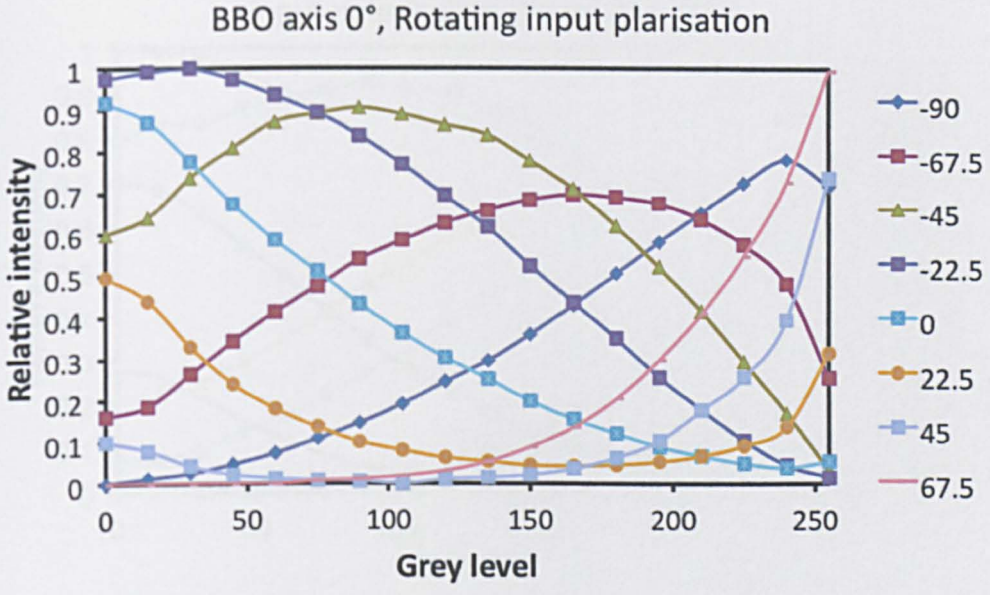

Fig. A-5: Relative intensity versus grey level (BBO axis 0°, various input polarisation directions).

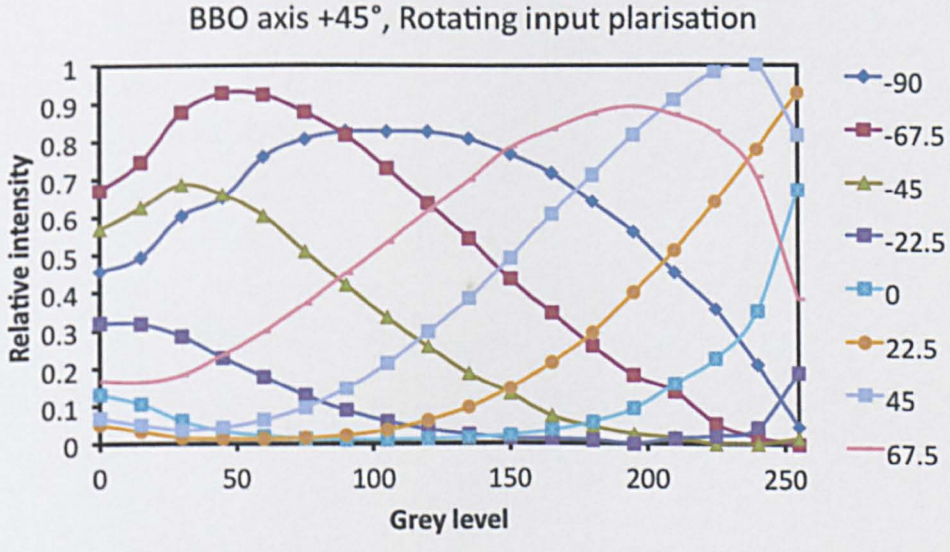

Fig. A-6: Relative intensity versus grey level (BBO axis +45°, various input polarisation directions).

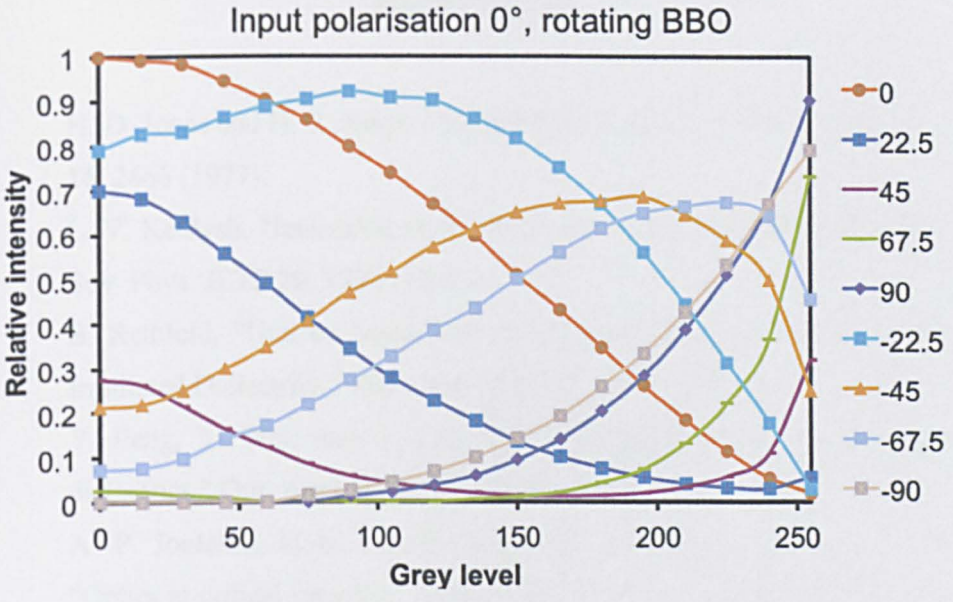

Fig. A-7: Relative intensity versus grey level (input polarisation directions 0°, rotating BBO axis).

References

1. H. D. Jones and H. R. Reiss, "Intense-field effects in solids," Phys. Rev. B **16**, 2466 (1977).
2. L. V. Keldysh, "Ionization in the field of a strong electromagnetic wave," Sov. Phys. JETP **20**, 1307 (1965).
3. B. Rethfeld, "Unified Model for the Free-Electron Avalanche in Laser-Irradiated Dielectrics," Phys. Rev. Lett **92**, 187401 (2004).
4. Y. Peng, Y. Wei, and Z. LV, "Femtosecond laser-induced damage in dielectrics," Opt. Appl. **XXXIV**(2004).
5. A. P. Joglekar, H.-h. Liu, E. Meyhofer, G. Mourou, and A. J. Hunt, "Optics at critical intensity: Applications to nanomorphing," P Natl. Acad. Sci. USA **101**, 5856 (2004).
6. E. Glezer and E. Mazur, "Ultrafast-laser driven micro-explosions in transparent materials," Appl. Phys. Lett. **71**, 882 (1997).
7. A. Baum, P. J. Scully, M. Basanta, C. L. Paul Thomas, P. R. Fielden, N. J. Goddard, W. Perrie, and P. R. Chalker, "Photochemistry of refractive index structures in poly(methyl methacrylate) by femtosecond laser irradiation," Opt. Lett. **32**, 190 (2007).
8. S. Sowa, W. Watanabe, T. Tamaki, J. Nishii, and K. Itoh, "Symmetric waveguides in poly(methyl methacrylate) fabricated by femtosecond laser pulses," Opt. Express **14**, 291 (2006).
9. A. Zoubir, C. Lopez, M. Richardson, and K. Richardson, "Femtosecond laser fabrication of tubular waveguides in poly(methyl methacrylate)," Opt. Lett. **29**, 1840 (2004).
10. T. Gorelik, M. Will, S. Nolte, A. Tuennermann, and U. Glatzel, "Transmission electron microscopy studies of femtosecond laser induced modifications in quartz," Appl. Phys. A **76**, 3090 (2003).
11. V. Apostolopoulos, L. Laversenne, T. Colomb, C. Depeursinge, R. P. Salathe, M. Pollnau, R. Osellame, G. Cerullo, and P. Laporta,

"Femtosecond-irradiation-induced refractive-index changes and channel waveguiding in bulk Ti^3+:Sapphire," Appl. Phys. Lett. **85**, 1122 (2004).

12. J. W. Chan, T. Huser, S. Risbud, and D. M. Krol, "Structural changes in fused silica after exposure to focused femtosecond laser pulses," Opt. Lett. **26**, 1726 (2001).
13. C. B. Schaffer, A. Brodeur, J. F. Garcìa, and E. Mazur, "Micromachining bulk glass by use of femtosecond laser pulses with nanojoule energy," Opt. Lett. **26**, 93 (2001).
14. A. M. Streltsov and N. F. Borrelli, "Study of femtosecond-laser-written waveguides in glasses," J. Opt. Soc. Am. B **19**, 2496 (2002).
15. W. J. Tomlinson, I. P. Kaminow, E. A. Chandross, R. L. Fork, and W. T. Silfvast, "Photoinduced refractive index increase in poly (methyl methacrylate) and its applications," Appl. Phys. Lett. **16**, 486 (1970).
16. A. Torikai, M. Ohno, and K. Fueki, "Photodegradation of poly(methyl methacrylate) by monochromatic light: Quantum yield, effect of wavelengths, and light intensity," J. Appl. Polym. Sci. **41**, 1023 (1990).
17. T. Mitsuoka, A. Torikai, and K. Fueki, "Wavelength sensitivity of the photodegradation of poly(methyl methacrylate)," J. Appl. Polym. Sci. **47**, 1027 (1993).
18. A. Torikai and T. Mitsuoka, "Electron spin resonance studies of poly(methyl methacrylate) irrdiated with monochromatic light," J. Appl. Polym. Sci. **55**, 1703 (1995).
19. J. M. Moran and I. P. Kaminow, "Properties of Holographic Gratings Photoinduced in Polymethyl Methacrylate," Appl. Opt. **12**, 1964 (1973).
20. G. Peng, Z. Xiong, and P. L. Chu, "Photosensitivity and Gratings in Dye-Doped Polymer Optical Fibers," Opt. Fiber Technol. **5**, 242 (1999).
21. J. Marotz, "Holographic storage in sensitized polymethyl methacrylate blocks," Appl. Phys. B **37**, 181 (1985).
22. S. Kuper and M. Stuke, "Ablation of uv-transparent materials with femtosecond uv excimer laser pulses," Microelectron. Eng. **9**, 475 (1989).

23. N. Bityurin, S. Muraviov, A. Alexandrov, and A. Malyshev, "UV laser modifications and etching of polymer films (PMMA) below the ablation threshold," Appl. Surf. Sci. **109-110**, 270 (1997).

24. A. K. Baker and P. E. Dyer, "Refractive-index modification of polymethylmethacrylate (PMMA) thin films by KrF-laser irradiation," Appl. Phys. A **57**, 543 (1993).

25. R. Gattass and E. Mazur, "Femtosecond laser micromachining in transparent materials," Nat. Photonics **2**, 219 (2008).

26. H. Misawa and S. Juodkazis, *3D laser microfabrication: principles and applications*, Wiley (2006).

27. S. Eaton, H. Zhang, P. Herman, F. Yoshino, L. Shah, J. Bovatsek, and A. Arai, "Heat accumulation effects in femtosecond laser-written waveguides with variable repetition rate," Opt. Express **13**, 4708 (2005).

28. K. Minoshima, A. M. Kowalevicz, I. Hartl, E. P. Ippen, and J. G. Fujimoto, "Photonic device fabrication in glass by use of nonlinear materials processing with a femtosecond laser oscillator," Opt. Lett. **26**, 1516 (2001).

29. G. Della Valle, R. Osellame, and P. Laporta, "Micromachining of photonic devices by femtosecond laser pulses," J. Opt. A: Pure Appl. Opt. **11**, 013001 (2009).

30. P. R. Herman, R. S. Marjoribanks, and A. Oettl, "Burst-ultrafast laser machining method," US Patent (6,552,301 B2).

31. R. Osellame, N. Chiodo, V. Maselli, A. Yin, M. Zavelani-Rossi, G. Cerullo, P. Laporta, L. Aiello, S. De Nicola, P. Ferraro, A. Finizio, and G. Pierattini, "Optical properties of waveguides written by a 26 MHz stretched cavity Ti:sapphire femtosecond oscillator," Opt. Express **13**, 612 (2005).

32. A. Killi, U. Morgner, M. J. Lederer, and D. Kopf, "Diode-pumped femtosecond laser oscillator with cavitydumping," Opt. Lett. **29**, 1288 (2004).

33. R. Osellame, N. Chiodo, G. Valle, S. Taccheo, R. Ramponi, G. Cerullo, A. Killi, U. Morgner, M. Lederer, and D. Kopf, "Optical waveguide writing with a diode-pumped femtosecondoscillator," Opt. Lett. **29**, 1900 (2004).

34. K. M. Davis, K. Miura, N. Sugimoto, and K. Hirao, "Writing waveguides in glass with a femtosecond laser," Opt. Lett. **21**, 1729 (1996).

35. J. Chan, T. Huser, S. Risbud, and D. Krol, "Waveguide fabrication in fused silica using tightly focused femtosecond laser pulses," Proc. SPIE **4640**, 129 (2002).

36. L. Sudrie, A. Couairon, M. Franco, B. Lamouroux, B. Prade, S. Tzortzakis, and A. Mysyrowicz, "Femtosecond laser-induced damage and filamentary propagation in fused silica.," Phys. Rev. Lett **89**, 186601 (2002).

37. N. Nguyen, A. Saliminia, W. Liu, S. Chin, and R. Vallee, "Optical breakdown versus filamentation in fused silica by use of femtosecond infrared laser pulses," Opt. Lett. **28**, 1591 (2003).

38. A. Saliminia, N. Nguyen, M. Nadeau, S. Petit, S. Chin, and R. Vallee, "Writing optical waveguides in fused silica using 1 kHz femtosecond infrared pulses," J. Appl. Phys. **93**, 3724 (2003).

39. H. Guo, H. Jiang, Y. Fang, C. Peng, H. Yang, Y. Li, and Q. Gong, "The pulse duration dependence of femtosecond laser induced refractive index modulation in fused silica," J. Opt. A: Pure Appl. Opt. **6**, 787 (2004).

40. A. Horn, E. Kreutz, and R. Poprawe, "Ultrafast time-resolved photography of femtosecond laser induced modifications in BK7 glass and fused silica," Appl. Phys. A **79**, 923 (2004).

41. C. Hnatovsky, R. Taylor, E. Simova, V. Bhardwaj, D. Rayner, and P. Corkum, "High-resolution study of photoinduced modification in fused silica produced by a tightly focused femtosecond laser beam in the presence of aberrations," J. Appl. Phys. **98**, 013517 (2005).

42. J. Liu, Z. Zhang, Z. Lu, G. Xiao, F. Sun, S. Chang, and C. Flueraru, "Fabrication and stitching of embedded multi-layer micro-gratings in fused silica glass by fs laser pulses," Appl. Phys. B **86**, 151 (2006).

43. T. Tamaki, W. Watanabe, H. Nagai, M. Yoshida, J. Nishii, and K. Itoh, "Structural modification in fused silica by a femtosecond fiber laser at 1558 nm," Opt. Express **14**, 6971 (2006).

44. I. Burakov, N. Bulgakova, R. Stoian, A. Mermillod-Blondin, E. Audouard, A. Rosenfeld, A. Husakou, and I. Hertel, "Spatial distribution of refractive index variations induced in bulk fused silica by single ultrashort and short laser pulses," J. Appl. Phys. **101**, 043506 (2007).

45. I. Zergioti, K. Kyrkis, D. Papazoglou, and S. Tzortzakis, "Structural modifications in fused silica induced by ultraviolet fs laser filaments," Appl. Surf. Sci. **253**, 7865 (2007).

46. H. Zhang, S. M. Eaton, and P. R. Herman, "Single-step writing of Bragg grating waveguides in fused silica with an externally modulated femtosecond fiber laser," Opt. Lett. **32**, 2559 (2007).

47. F. He, Y. Cheng, Z. Xu, Y. Liao, J. Xu, H. Sun, C. Wang, Z. Zhou, K. Sugioka, K. Midorikawa, Y. Xu, and X. Chen, "Direct fabrication of homogeneous microfluidic channels embedded in fused silica using a femtosecond laser," Opt. Lett. **35**, 282 (2010).

48. F. He, H. Xu, Y. Cheng, J. Ni, H. Xiong, Z. Xu, K. Sugioka, and K. Midorikawa, "Fabrication of microfluidic channels with a circular cross section using spatiotemporally focused femtosecond laser pulses," Opt. Lett. **35**, 1106 (2010).

49. D. Wortmann, J. Gottmann, N. Brandt, and H. Horn-Solle, "Micro- and Nanostructures inside Sapphire by FS-Laser Irradiation and Selective Etching," Opt. express **16**, 1517 (2008).

50. Y. Cheng, K. Sugioka, M. Masuda, K. Midorikawa, M. Kawachi, K. Shihoyama, and K. Toyoda, "3D microstructuring inside photosensitive glass by use of a femtosecond laser for lab-on-chip applications," Proc. SPIE **4977**, 314 (2003).

51. Y. Cheng, K. Sugioka, M. Masuda, K. Shihoyama, K. Toyoda, and K. Midonkawa, "Three-dimensional micro-optical components embedded in Foturan glass by a femtosecond laser," Proc. SPIE **5063**, 103 (2003).

52. Y. Cheng, K. Sugioka, M. Masuda, K. Toyoda, M. Kawachi, K. Shihoyama, and K. Midorikawa, "3D microstructuring inside Foturan glass by femtosecond laser," Riken Review, 101 (2003).

53. M. Masuda, K. Sugioka, Y. Cheng, N. Aoki, M. Kawachi, K. Shihoyama, K. Toyoda, H. Helvajian, and K. Midorikawa, "3-D microstructuring inside photosensitive glass by femtosecond laser excitation," Appl. Phys. A **76**, 857 (2003).

54. S. Ho, P. Herman, Y. Cheng, K. Sugioka, and K. Midorikawa, "Direct ultrafast laser writing of buried waveguides in Foturan glass," Lasers and Electro-Optics, (CLEO) **2**(2004).

55. M. Masuda, K. Sugioka, Y. Cheng, T. Hongo, K. Shihoyama, H. Takai, I. Miyamoto, and K. Midorikawa, "Direct fabrication of freely movable microplate inside photosensitive glass by femtosecond laser for lab-on-chip application," Appl. Phys. A **78**, 1029 (2004).

56. K. Sugioka, M. Masuda, T. Hongo, Y. Cheng, K. Shihoyama, and K. Midorikawa, "Three-dimensional microfluidic structure embedded in photostructurable glass by femtosecond laser for lab-on-chip applications," Appl. Phys. A **79**, 815 (2004).

57. V. Bhardwaj, E. Simova, P. Corkum, D. Rayner, C. Hnatovsky, R. Taylor, B. Schreder, M. Kluge, and J. Zimmer, "Femtosecond laser-induced refractive index modification in multicomponent glasses," J. Appl. Phys. **97**, 083102 (2005).

58. Y. Cheng, K. Sugioka, and K. Midorikawa, "Microfabrication of 3D hollow structures embedded in glass by femtosecond laser for Lab-on-a-chip applications," Appl. Surf. Sci. **248**, 172 (2005).

59. T. Hongo, K. Sugioka, H. Niino, Y. Cheng, M. Masuda, I. Miyamoto, H. Takai, and K. Midorikawa, "Investigation of photoreaction mechanism of photosensitive glass by femtosecond laser," J. Appl. Phys. **97**, 063517 (2005).

60. K. Sugioka, Y. Cheng, and K. Midorikawa, "Three-dimensional micromachining of glass using femtosecond laser for lab-on-a-chip device manufacture," Appl. Phys. A **81**, 1 (2005).

61. Y. Cheng, K. Sugioka, K. Midorikawa, and Z. Xu, "Integrating 3D photonics and microfluidics using ultrashort laser pulses," SPIE Newsroom 1-3 (2006).

62. Y. Cheng, H. Tsai, K. Sugioka, and K. Midorikawa, "Fabrication of 3D microoptical lenses in photosensitive glass using femtosecond laser micromachining," Appl. Phys. A **85**, 11 (2006).

63. Y. Cheng, Z. Xu, K. Sugioka, and K. Midorikawa, "Femtosecond laser microfabrication of 3D structures in Foturan glass," Proc. SPIE **6400**, 640001 (2006).

64. R. An, Y. Li, D. Liu, Y. P. Dou, F. Qi, H. Yang, and Q. Gong, "Optical waveguide writing inside Foturan glass with femtosecond laser pulses," Appl. Phys. A **86**, 343 (2007).

65. Z. Wang, K. Sugioka, and K. Midorikawa, "Three-dimensional integration of microoptical components buried inside photosensitive glass by femtosecond laser direct writing," Appl. Phys. A **89**, 951 (2007).

66. Y. Wu, C.-Y. Wang, W. Jia, M. Hu, X. Ni, and L. Chai, "Fundamental microstructures fabricated on FOTURAN glass using femtosecond laser," Proc. SPIE **6825**, 68250I (2007).

67. F. He, H. Sun, M. Huang, J. Xu, Y. Liao, Z. Zhou, Y. Cheng, Z. Xu, K. Sugioka, and K. Midorikawa, "Rapid fabrication of optical volume gratings in Foturan glass by femtosecond laser micromachining," Appl. Phys. A **97**, 853-857 (2009).

68. A. Heltzel, A. Battula, J. Howell, and S. Chen, "Nanostructuring borosilicate glass with near-field enhanced energy using a femtosecond laser pulse," ASME J. Heat Transfer **129**, 53 (2007).

69. O. M. Efimov, L. B. Glebov, and V. I. Smirnov, "High-frequency Bragg gratings in a photothermorefractive glass," Opt. Lett. **25**, 1693 (2000).

70. L. A. Siiman, J. Lumeau, L. Canioni, and L. B. Glebov, "Ultrashort laser pulse diffraction by transmitting volume Bragg gratings in photo-thermo-refractive glass," Opt. Lett. **34**, 2572 (2009).

71. N. Takeshima, Y. Narita, S. Tanaka, Y. Kuroiwa, and K. Hirao, "Fabrication of high-efficiency diffraction gratings in glass," Opt. Lett. **34**, 2572 (2005).

72. S. Mailis, A. Anderson, S. Barrington, W. Brocklesby, R. Greef, H. Rutt, R. Eason, N. Vainos, and C. Grivas, "Photosensitivity of lead germanate glass waveguides grown by pulsed laser deposition," Opt. Lett. **23**, 1751 (1998).

73. Y. Cheng, K. Sugioka, M. Masuda, K. Shihoyama, K. Toyoda, and K. Midorikawa, "Optical gratings embedded in photosensitive glass by photochemical reaction using a femtosecond laser," Opt. Express **11**, 1809 (2003).

74. D. Ehrt, T. Kittel, M. Will, S. Nolte, and A. Tünnermann, "Femtosecond-laser-writing in various glasses," J. of Non-Crystal. Solids **345**, 332 (2004).

75. J. Siegel, J. M. Fernández-Navarro, A. García-Navarro, V. Diez-Blanco, O. Sanz, J. Solis, F. Vega, and J. Armengol, "Waveguide structures in heavy metal oxide glass written with femtosecond laser pulses above the critical self-focusing threshold," Appl. Phys. Lett. **86**, 121109 (2005).

76. K. Paivasaari, V. Tikhomirov, and J. Turunen, "High refractive index chalcogenide glass for photonic crystal applications," Opt. Express **15**, 2336 (2007).

77. B. H. Cumpston, S. P. Ananthavel, S. Barlow, D. L. Dyer, J. E. Ehrlich, L. L. Erskine, A. A. Heikal, S. M. Kuebler, I. S. Lee, D. Mccord-Maughon, J. Qin, H. Rockel, M. Rumi, X. Wu, S. R. Marder, and J. W. Perry, "Two-photon polymerization initiators for three-dimensional optical data storage and microfabrication," Nature **398**, 51 (1999).

78. R. Inführ, J. Stampfl, S. Krivec, R. Liska, H. Lichtenegger, V. Satzinger, V. Schmidt, N. Matsko, and W. Grogger, "3D-structuring of optical waveguides with two photon polymerization," Mater. Res. Soc. Symp. Proc. **1179** (2009).

79. M. Malinauskas, A. Žukauskas, G. Bičkauskaitė, R. Gadonas, and S. Juodkazis, "Mechanisms of three-dimensional structuring of photo-

polymers by tightly focussed femtosecond laser pulses," Opt. Express **18**, 10209 (2010).

80. M. Miwa, S. Juodkazis, T. Kawakami, S. Matsuo, and H. Misawa, "Femtosecond two-photon stereo-lithography," Appl. Phys. A **73**, 561 (2001).

81. A. Ovsianikov and B. N. Chichkov, "Chapter 12 Two-Photon Polymerization – High Resolution 3D Laser Technology and Its Applications," in *Nanoelectronics and Photonics*, A. Korkin and F. Rosei, eds. (Springer, 2008).

82. M. Straub and M. Gu, "Near-infrared photonic crystals with higher-order bandgaps generated by two-photon photopolymerization," Opt. Lett. **27**, 1824 (2002).

83. D. L. N. Kallepalli, N. R. Desai, and V. R. Soma, "Fabrication and optical characterization of microstructures in poly(methylmethacrylate) and poly(dimethylsiloxane) using femtosecond pulses for photonic and microfluidic applications," Appl. Opt. **49**, 2475 (2010).

84. S.-H. Cho, W.-S. Chang, K.-R. Kim, and J. W. Hong, "Femtosecond laser embedded grating micromachining of flexible PDMS plates," Opt. Commun. **282**, 1317 (2009).

85. D. B. Wolfe, J. B. Ashcom, J. C. Hwang, C. B. Schaffer, E. Mazur, and G. M. Whitesides, "Customization of Poly(dimethylsiloxane) Stamps by Micromachining Using a Femtosecond-Pulsed Laser," Adv. Mater **15**, 62 (2003).

86. T. O. Yoon, H. J. Shin, S. C. Jeoung, and Y.-I. Park, "Formation of superhydrophobic poly(dimethysiloxane) by ultrafast laser-induced surface modification," Opt. Express **16**, 12715 (2008).

87. C. Wochnowski, Y. Cheng, K. Meteva, K. Sugioka, K. Midorikawa, and S. Metev, "Femtosecond-laser induced formation of grating structures in planar polymer substrates," J. Opt. A: Pure Appl. Opt. **7**, 493 (2005).

88. H. Mochizuki, W. Watanabe, R. Ezoe, T. Tamaki, Y. Ozeki, K. Itoh, M. Kasuya, K. Matsuda, and S. Hirono, "Density characterization of

femtosecond laser modification in polymers," Appl. Phys. Lett. **92**, 091120 (2008).

89. Z. Nie, H. Lee, H. Yoo, Y. Lee, Y. Kim, K.-S. Lim, and M. Lee, "Multilayered optical bit memory with a high signal-to-noise ratio in fluorescent polymethylmethacrylate," Appl. Phys. Lett. **94**, 111912 (2009).
90. H. Tang, H. Jiu, B. Jiang, J. Cai, H. Xing, Q. Zhang, W. Huang, A. Xia, Q. Liu, G. Cheng, and G. Chen, "Three-dimensional optical storage recording by microexplosion in a doped PMMA polymer," Proc. SPIE **5643**, 258 (2005).
91. A. Baum, P. Scully, W. Perrie, M. Sharp, K. Watkins, D. Jones, R. Issac, and D. Jaroszynski, "NUV and NIR Femtosecond Laser Modification of PMMA," in *LPM2007-the 8th International Symposium on Laser Precision Microfabrication*, 2007),
92. D. Liu, J. Cheng, W. Perrie, A. Baum, P. Scully, M. Sharp, S. Edwardson, Z. Kuang, N. Semaltianos, and P. French, "Femtosecond laser micro-structuring of materials in the nir and uv regime," ICALEO 2007 (2007).
93. A. Baum, P. J. Scully, W. Perrie, D. Jones, R. Issac, and D. A. Jaroszynski, "Pulse-duration dependency of femtosecond laser refractive index modification in poly(methyl methacrylate)," Opt. Lett. **33**, 651 (2008).
94. P. Scully, D. Jones, and D. Jaroszynski, "Femtosecond laser irradiation of polymethylmethacrylate for refractive index gratings," J. Opt. A: Pure Appl. Opt. **5**, 92 (2003).
95. P. J. Scully, R. Bartlett, S. Caulder, P. Eldridge, R. Chandy, J. McTavish, V. Alexiou, I. P. Clarke, M. Towrie, and A.W.Parker., "UV laser photo-induced refractive index changes in poly methyl methacrylate and plastic optical fibres for application as sensors and devices," 14th International Conference on Optical Fiber Sensors **4185**, 854 (2000).
96. P. J. Scully, D. Jones, and D. A. Jaroszynski, "Writing refractive index gratings in perspex and polymer optical fibre using femtosecond laser irradiation," in *Photon 02,* (IOP, Cardiff, 2002).

97. N. Uppal, P. S. Shiakolas, and M. Rizwan, "Three dimensional waveguide fabrication in PMMA using femtosecond laser micromachining system," Proc. SPIE **6882**, 68820I (2008).

98. C. R. Mendonca, L. R. Cerami, T. Shih, R. W. Tilghman, T. Baldacchini, and E. Mazur, "Femtosecond laser waveguide micromachining of PMMA films with azoaromatic chromophores," Opt. Express **16**, 200 (2008).

99. G. Zhou, M. J. Ventura, M. R. Vanner, and M. Gu, "Use of ultrafast-laser-driven microexplosion for fabricatingthree-dimensional void-based diamond-lattice photonic crystalsin a solid polymer material," Opt. Lett. **29**, 2240 (2004).

100. D. Day and M. Gu, "Microchannel fabrication in PMMA based on localized heating by nanojoule high repetition rate femtosecond pulses," Opt. Express **13**, 5939 (2005).

101. D. F. Farson, H. W. Choi, C. Lu, and L. J. Lee, "Femtosecond laser bulk micromachining of microfluid channels in poly(methylmethacrylate)," J Laser Appl. **18**, 210 (2006).

102. D. Gomez, I. Goenaga, I. Lizuain, and M. Ozaita, "Femtosecond laser ablation for microfluidics," Opt. Eng. **44**, 051105 (2005).

103. M. Haiducu and et al., "Deep-UV patterning of commercial grade PMMA for low-cost, large-scale microfluidics," J Micromech. Microeng. **18**, 115029 (2008).

104. N. M. Bityurin, A. I. Korytina, S. V. Muraviova, and A. M. Yurkin, "Second harmonic of Ti:sapphire femtosecond laser as a possible tool for pointlike 3D optical information recording," in *SPIE Conference on Laser Applications in Microelectronic and Optoelectronic Manufacturing IV*, 122 (1999).

105. A. Baum, P. J. Scully, W. Perrie, D. Liu, and V. Lucarini, "Mechanisms of femtosecond laser-induced refractive index modification of poly(methyl methacrylate)," J. Opt. Soc. Am. B **27**, 107 (2010).

106. Y. Li, K. Yamada, T. Ishizuka, W. Watanabe, K. Itoh, and Z. Zhou, "Single femtosecond pulse holography using polymethyl methacrylate," Opt. Express **10**, 1173 (2002).

107. R. Osellame, S. Taccheo, M. Marangoni, R. Ramponi, P. Laporta, D. Polli, S. De Silvestri, and G. Cerullo, "Femtosecond writing of active optical waveguides with astigmatically shaped beams," J. Opt. Soc. Am. B **20**, 1559 (2003).

108. C. Mauclair, A. Mermillod-Blondin, N. Huot, E. Audouard, and R. Stoian, "Ultrafast laser writing of homogeneous longitudinal waveguides in glasses using dynamic wavefront correction," Opt. Express **16**, 5481 (2008).

109. R. Thomson, A. Bockelt, E. Ramsay, S. Beecher, A. Greenaway, A. Kar, and D. Reid, "Shaping ultrafast laser inscribed optical waveguides using a deformable mirror," Opt. Express **16**, 12786 (2008).

110. M. Ams, G. Marshall, D. Spence, and M. Withford, "Slit beam shaping method for femtosecond laser direct-write fabrication of symmetric waveguides in bulk glasses," Opt. Express **13**, 5676 (2005).

111. G. Cerullo, R. Osellame, S. Taccheo, M. Marangoni, D. Polli, R. Ramponi, P. Laporta, and S. De Silvestri, "Femtosecond micromachining of symmetric waveguides at 1.5 μm by astigmatic beam focusing," Opt. Lett. **27**, 1938 (2002).

112. M. Will, S. Nolte, B. N. Chichkov, and A. T¸nnermann, "Optical Properties of Waveguides Fabricated in Fused Silica by Femtosecond Laser Pulses," Appl. Opt. **41**, 4360 (2002).

113. J. Zhai, Y. Shen, J. Si, J. Qiu, and K. Hirao, "The fabrication of permanent holographic gratings in bulk polymer medium by a femtosecond laser," J Phys. D Appl. Phys. **34**, 3466 (2001).

114. B. Tan, N. Sivakumar, and K. Venkatakrishnan, "Direct grating writing using femtosecond laser interference fringes formed at the focal point," J. Opt. A-Pure Appl. Opt. **7**, 169 (2005).

115. C. Smelser, D. Grobnic, and S. Mihailov, "Fabrication of femtosecond laser-induced Bragg gratings in amorphous and crystalline dielectric waveguides," Proc. SPIE **6796**, 67961E (2007).

116. S. Hirono, M. Kasuya, K. Matsuda, Y. Ozeki, K. Itoh, H. Mochizuki, and W. Watanabe, "Increasing diffraction efficiency by heating phase gratings

formed by femtosecond laser irradiation in poly(methyl methacrylate)," Appl. Phys. Lett. **94**, 241122 (2009).

117. C. Yang, X. Yan, R. Zhu, H. Zou, and F. Han, "Diffraction study of volume holographic gratings in dispersive photorefractive material for femtosecond pulse readout," Optik **121**, 1138 (2009).
118. S. C. Barden, J. A. Arns, W. S. Colburn, and J. B. Williams, "Volume phase holographic grating and efficiency of three simple VPH gratings," Publ. Astron. Soc. Pac, 1-33 (2000).
119. V. Passaro and F. Magno, "Holographic gratings in photorefractive materials: A review," Laser Phys. **17**, 231 (2007).
120. K. Zhou, Z. Guo, W. Ding, and S. Liu, "Analysis on volume grating induced by femtosecond laser pulses," Opt. Express **18**, 13640 (2010).
121. K. Yamada, W. Watanabe, K. Kintaka, J. Nishii, and K. Itoh, "Volume Grating Induced by a Self-Trapped Long Filament of Femtosecond Laser Pulses in Silica Glass," Jpn. J. Appl. Phys. **42**, 6916 (2003).
122. D. Liu, Z. Kuang, W. Perrie, P. J. Scully, A. Baum, S. P. Edwardson, E. Fearon, G. Dearden, and K. G. Watkins, "High-speed uniform parallel 3D refractive index micro-structuring of poly(methyl methacrylate) for volume phase gratings," Appl. Phys. B **101**, 817 (2010).
123. K.-i. Kawamura, N. Sarukura, M. Hirano, and H. Hosono, "Holographic Encoding of Permanent Gratings Embedded in Diamond by Two Beam Interference of a Single Femtosecond Near-Infrared Laser Pulse," Jpn. J. Appl. Phys. **39**, L767 (2000).
124. C. Voigtländer, D. Richter, J. Thomas, A. Tünnermann, and S. Nolte, "Inscription of high contrast volume Bragg gratings in fused silica with femtosecond laser pulses," Appl. Phys. A **102,** 35 (2011).
125. K. Ohta, M. Kamata, M. Obara, and N. Sawanobori, "Optical waveguide fabrication in new glasses and PMMA with temporally tailored ultrashort laser," Proc. SPIE **5340**, 172 (2004).
126. L. Sudrie, M. Franco, B. Prade, and A. Mysyrowicz, "Study of damage in fused silica induced by ultra-short IR laser pulses," Opt. Commun. **191**, 333 (2001).

127. A. Saliminia, N. Nguyen, S. Chin, and R. Vallée, "The influence of self-focusing and filamentation on refractive index modifications in fused silica using intense femtosecond pulses," Opt. Commun. **241**, 529 (2004).

128. K. Itoh, "Nano-and microprocessing in glass using fs laser," Proc. of SPIE **4830**, 550 (2003).

129. K. Yamada, W. Watanabe, T. Toma, K. Itoh, and J. Nishii, "In situ observation of photoinduced refractive-index changes in filaments formed in glasses by femtosecond laser pulses," Opt. Lett. **26**, 19 (2001).

130. W. Yang, P. Kazansky, and Y. Svirko, "Non-reciprocal ultrafast laser writing," Nat. Photonics **2**, 99 (2008).

131. D. Ehrt, T. Kittel, M. Will, S. Nolte, and A. Tünnermann, "Femtosecond-laser-writing in various glasses," J Non-Cryst. Solids **345**, 332 (2004).

132. W. Kautek, J. Kruger, M. Lenzner, S. Sartania, C. Spielmann, and F. Krausz, "Laser ablation of dielectrics with pulse durations between 20 fs and 3 ps," Appl. Phys. Lett. **69**, 3146 (1996).

133. K. Yamada, W. Watanabe, T. Asano, J. Nishii, and K. Itoh, "Polarization dependence of refractive-index change in silica glass induced by self-trapped filament of femtosecond laser pulses," Proc. SPIE **4830**, 581 (2003).

134. K. Yamada, W. Watanabe, K. Itoh, and J. Nishii, "Dependence of refractive index charge in silica glass on polarization of incident ultrashort laser pulses," Proc. SPIE **4416**, 344 (2001).

135. K. Yamada, W. Watanabe, J. Nishii, and K. Itoh, "Anisotropic refractive-index change in silica glass induced by self-trapped filament of linearly polarized femtosecond laser pulses," J. Appl. Phys. **93**, 1889 (2003).

136. M. Ams, G. D. Marshall, and M. J. Withford, "Study of the influence of femtosecondlaser polarisation on direct writing ofwaveguides," Opt. Express **14**, 13158 (2006).

137. S. Akturk, X. Gu, E. Zeek, and R. Trebino, "Pulse-front tilt caused by spatial and temporal chirp," Opt. Express **12**, 4399 (2004).

138. G. Pretzler, A. Kasper, and K. Witte, "Angular chirp and tilted light pulses in CPA lasers," Appl. Phys. B **70**, 1 (2000).

139. P. G. Kazansky, W. Yang, E. Bricchi, J. Bovatsek, A. Arai, Y. Shimotsuma, K. Miura, and K. Hirao, ""Quill" writing with ultrashort light pulses in transparent materials," Appl. Phys. Lett. **90**, 151120 (2007).

140. Z. Sacks, G. Mourou, and R. Danielius, "Adjusting pulse-front tilt and pulse duration by use of a single-shot autocorrelator," Opt. Lett. **26**, 462 (2001).

141. S. Akturk, M. Kimmel, P. O'Shea, and R. Trebino, "Measuring pulse-front tilt in ultrashort pulses using GRENOUILLE," Opt. Express **11**, 491 (2003).

142. S. Akturk, M. Kimmel, and R. Trebino, "Extremely simple device for measuring 1.5-μm ultrashort laser pulses," Opt. Express **12**, 4483 (2004).

143. J. B. Ashcom, R. R. Gattass, C. B. Schaffer, and E. Mazur, "Numerical aperture dependence of damage and supercontinuum generation from femtosecond laser pulses in bulk fused silica," J. Opt. Soc. Am. B **23**, 2317 (2006).

144. D. Homoelle, S. Wielandy, A. L. Gaeta, N. F. Borrelli, and C. Smith, "Infrared photosensitivity in silica glasses exposed to femtosecond laser pulses," Opt. Lett. **24**, 1311 (1999).

145. M. Kamata and M. Obara, "Control of the refractive index change in fused silica glasses induced by a loosely focused femtosecond laser," Appl. Phys. A **78**, 85 (2004).

146. D. Liu, Y. Li, M. Liu, H. Yang, and Q. Gong, "The polarization-dependence of femtosecond laser damage threshold inside fused silica," Appl. Phys. B **91**, 597 (2008).

147. D. Liu, Y. Li, R. An, Y. P. Dou, H. Yang, and Q. Gong, "Influence of focusing depth on the microfabrication of waveguides inside silica glass by femtosecond laser direct writing," Appl. Phys. A **84**, 257 (2006).

148. C. Mauclair, G. Cheng, N. Huot, E. Audouard, A. Rosenfeld, I. V. Hertel, and R. Stoian, "Dynamic ultrafast laser spatial tailoring for parallel micromachining of photonic devices in transparent materials," Opt. Express **17**, 3531 (2009).

149. A. Jesacher and M. J. Booth, "Parallel direct laser writing in three dimensions with spatially dependent aberration correction," Opt. Express **18**, 21090 (2010).

150. L. Sudrie, A. Couairon, M. Franco, B. Lamouroux, B. Prade, S. Tzortzakis, and A. Mysyrowicz, "Femtosecond laser-induced damage and filamentary propagation in fused silica.," Phys Rev Lett **89**, 186601 (2002).

151. S. Tzortzakis, L. Sudrie, M. Franco, B. Prade, A. Mysyrowicz, A. Couairon, Berg, eacute, and L., "Self-Guided Propagation of Ultrashort IR Laser Pulses in Fused Silica," Phys. Rev. Lett **87**, 213902 (2001).

152. W. Watanabe, "Femtosecond filamentary modifications in bulk polymer materials," Laser Phys. **19**, 342 (2009).

153. F. Korte, S. Adams, A. Egbert, C. Fallnich, A. Ostendorf, S. Nolte, M. Will, J. P. Ruske, B. Chichkov, and A. Tuennermann, "Sub-diffraction limited structuring of solid targets with femtosecond laser pulses," Opt. Express **7**, 41 (2000).

154. J. W. Chan, T. R. Huser, S. H. Risbud, J. S. Hayden, and D. M. Krol, "Waveguide fabrication in phosphate glasses using femtosecond laser pulses," Appl. Phys. Lett. **82**, 2371 (2003).

155. D. M. Krol, J. W. Chan, T. R. Huser, S. H. Risbud, and J. S. Hayden, "Fs-laser fabrication of photonic structures in glass: the role of glass composition," Proc. SPIE **5662**, 30 (2004).

156. W. J. Reichman, D. M. Krol, L. Shah, F. Yoshino, A. Arai, S. M. Eaton, and P. R. Herman, "A spectroscopic comparison of femtosecond-laser-modified fused silica using kilohertz and megahertz laser systems," J. Appl. Phys. **99**, 123112 (2006).

157. J. Dechant, "Refraction and Extinction of polymers," in *Optical properties of polymers*, H. v. G. H. Meeten, ed. (Elsveier, London/New York, 1986).

158. D. Marcuse, "Refractive index determination by the focusing method," Appl Opt **18**, 9 (1979).

159. Z. Liu, X. Dong, Q. Chen, C. Yin, Y. Xu, and Y. Zheng, "Nondestructive Measurement of an Optical Fiber Refractive-Index Profile by a

Transmitted-Light Differential Interference Contact Microscope," Appl. Opt. **43**, 1485 (2004).

160. H. Kogelnik, "Coupled wave theory for thick hologram gratings," Bell Syst. Tech. J. **48**, 2909 (1969).
161. C. V. Raman and N. S. Nagendra Nathe, "The diffraction of light by high frequency sound waves: Part I & II," P. Indian AS - Section A **2**, 406 (1935).
162. M. G. Moharam, E. B. Grann, D. A. Pommet, and T. K. Gaylord, "Formulation for stable and efficient implementation of the rigorous coupled-wave analysis of binary gratings," J. Opt. Soc. Am. A **12**, 1068 (1995).
163. M. G. Moharam, T. K. Gaylord, and R. Magnusson, "Criteria for Raman-Nath regime diffraction by phase gratings," Opt. Commun. **32**, 19 (1980).
164. C. Neipp, I. Pascual, and A. Belendez, "Experimental evidence of mixed gratings with a phase difference between the phase and amplitude grating in volume holograms," Opt. Express **10**, 1374 (2002).
165. T. Gaylord and M. Moharam, "Analysis and applications of optical diffraction by gratings," P. IEEE **73**, 894 (1985).
166. K.-i. Kawamura, M. Hirano, T. Kamiya, and H. Hosono, "Holographic writing of volume-type microgratings in silica glass by a single chirped laser pulse," Appl. Phys. Lett. **81**, 1137 (2002).
167. Y. Li, W. Watanabe, K. Yamada, T. Shinagawa, K. Itoh, J. Nishii, and Y. Jiang, "Holographic fabrication of multiple layers of grating inside soda-lime glass with femtosecond laser pulses," Appl. Phys. Lett. **80**, 1508 (2002).
168. Y. Kuroiwa, N. Takeshima, Y. Narita, S. Tanaka, and K. Hirao, "Arbitrary micropatterning method in femtosecond laser microprocessing using diffractive optical elements," Opt. Express **12**, 1908 (2004).
169. Z. Kuang, D. Liu, W. Perrie, J. Cheng, S. Shang, S. P. Edwardson, E. Fearon, G. Dearden, and K. G. Watkins, "Diffractive multi-beam ultra-fast laser micro-processing using a spatial light modulator," Chinese Journal of Lasers **36**, 3093 (2009).

170. M. Sakakura, T. Sawano, Y. Shimotsuma, K. Miura, and K. Hirao, "Fabrication of three-dimensional 1x4 splitter waveguides inside a glass substrate with spatially phase modulated laser beam," Opt. Express **18**, 12136 (2010).

171. T. Akihiro, Y. Hirotsugu, H. Yoshio, N. Nobuo, and M. Hiroaki, "Three-Dimensional Optical Recording in a Human Fingernail," in *Information Photonics, 2005*, (Optical Society of America, 2005), 1-3.

172. A. Takita, H. Yamamoto, Y. Hayasaki, N. Nishida, and H. Misawa, "Three-dimensional optical memory using a human fingernail," Opt. Express **13**, 4560 (2005).

173. S. Hasegawa, Y. Hayasaki, and N. Nishida, "Holographic femtosecond laser processing with multiplexed phase Fresnel lenses," Opt. Lett. **31**, 1705 (2006).

174. Y. Hayasaki, "Holographic femtosecond laser processing and three-dimensional recording in biological tissue," Progress In Electromagnetics Research Letters **2**, 115 (2008).

175. A. Mermillod-Blondin, C. Mauclair, A. Rosenfeld, J. Bonse, I. Hertel, E. Audouard, and R. Stoian, "Size correction in ultrafast laser processing of fused silica by temporal pulse shaping," Appl. Phys. Lett. **93**, 021921 (2008).

176. M. Pospiech, M. Emons, A. Steinmann, G. Palmer, R. Osellame, N. Bellini, G. Cerullo, and U. Morgner, "Double waveguide couplers produced by simultaneous femtosecond writing," Opt. Express **17**, 3555 (2009).

177. A. Ruiz de la Cruz, A. Ferrer, W. Gawelda, D. Puerto, M. G. n. Sosa, J. Siegel, and J. Solis, "Independent control of beam astigmatism and ellipticity using a SLM for fs-laser waveguide writing," Opt. Express **17**, 20853 (2009).

178. M. Sakakura, T. Sawano, Y. Shimotsuma, K. Miura, and K. Hirao, "Parallel Drawing of Multiple Bent Optical Waveguides Using a Spatial Light Modulator," Jpn. J. Appl. Phys. **48**, 126507 (2009).

179. D. Liu, Z. Kuang, W. Perrie, P. J. Scully, A. Baum, S. Liang, A. Taranu, S. P. Edwardson, E. Fearon, G. Dearden, and K. G. Watkins, "Femtosecond laser internal structuring of materials using a spatial light modulator," in *PICALO*, 2010), 1-5.

180. D. Liu, W. Perrie, Z. Kuang, P. J. Scully, A. Baum, S. Liang, A. Taranu, S. P. Edwardson, E. Fearon, G. Dearden, and K. G. Watkins, "Multiple Beam Internal Structuring of PMMA," in *LPM2010*, 1-4 (2010).

181. M. Pospiech, M. Emons, B. V‰ckenstedt, G. Palmer, and U. Morgner, "Single-sweep laser writing of 3D-waveguide devices," Opt. Express **18**, 6994 (2010).

182. U. Efron, "Spatial light modulators for optical computing and information processing," System Sciences **1**, 416 (1989).

183. Y. Kozawa and S. Sato, "Optical trapping of micrometer-sized dielectric particles by cylindrical vector beams," Opt. Express **18**, 10828 (2010).

184. J. Leach, G. Sinclair, P. Jordan, J. Courtial, M. Padgett, J. Cooper, and Z. Laczik, "3D manipulation of particles into crystal structures using holographic optical tweezers," Opt. Express **12**, 220 (2004).

185. G. Sinclair, J. Leach, P. Jordan, G. Gibson, E. Yao, Z. Laczik, M. Padgett, and J. Courtial, "Interactive application in holographic optical tweezers of a multi-plane Gerchberg-Saxton algorithm for three-dimensional light shaping," Opt. Express, **12**, 1665 (2004).

186. B. Sun, Y. Roichman, and D. Grier, "Theory of holographic optical trapping," Opt. Express **16**, 15765 (2008).

187. J. Grieve, A. Ulcinas, S. Subramanian, G. Gibson, M. Padgett, D. Carberry, and M. Miles, "Hands-on with optical tweezers: a multitouch interface for holographic optical trapping," Opt. Express **17**, 3595 (2009).

188. N. Huot, N. Sanner, and E. Audouard, "Programmable focal spot shaping of amplified femtosecond laser pulses and their application to micromachining," Proc. SPIE **6400**, 64000K (2006).

189. N. Sanner, N. Huot, E. Audouard, C. Larat, and J. Huignard, "Spatial beam shaping of femtosecond laser pulses application to micromachining

and photowriting," Lasers and Electro-Optics, 2005.(CLEO). Conference on **3** (2005).

190. N. Sanner, N. Huot, E. Audouard, C. Larat, and J. Huignard, "Direct ultrafast laser micro-structuring of materials using programmable beam shaping," Opt. Lasers Eng. **45**, 737 (2007).

191. N. Sanner, N. Huot, E. Audouard, C. Larat, J. Huignard, and B. Loiseaux, "Programmable focal spot shaping of amplified femtosecond laser pulses," Opt. Lett. **30**, 1479 (2005).

192. O. Samek, V. Hommes, R. Hergenröder, and S. Kukhlevsky, "Femtosecond pulse shaping using a liquid–crystal display: Applications to depth profiling analysis," Rev. Sci. Instrum. **76**, 086104 (2005).

193. Z. Kuang, W. Perrie, J. Leach, M. Sharp, S. Edwardson, M. Padgett, G. Dearden, and K. Watkins, "High throughput diffractive multi-beam femtosecond laser processing using a spatial light modulator," Appl. Surf. Sci. **255**, 2284 (2008).

194. Z. Kuang, D. Liu, W. Perrie, S. Edwardson, M. Sharp, E. Fearon, G. Dearden, and K. Watkins, "Fast parallel diffractive multi-beam femtosecond laser surface micro-structuring," Appl. Surf. Sci **255**, 6582 (2009).

195. D. Liu, Z. Kuang, S. Shang, W. Perrie, D. Karnakis, A. Kearsley, M. Knowles, S. Edwardson, G. Dearden, and K. Watkins, "Ultrafast parallel laser processing of materials for high throughput manufacturing," in *LAMP2009 - the 5th International Congress on Laser Advanced Materials Processing*, 2009),

196. Z. Kuang, W. Perrie, D. Liu, S. Edwardson, J. Cheng, G. Dearden, and K. Watkins, "Diffractive multi-beam surface micro-processing using 10ps laser pulses," Appl. Surf. Sci. **255**, 9040 (2009).

197. R. W. Gerchberg and O. Saxton, "A practical algorithm for the determination of the phase from image and diffraction plane pictures," Optik **35**, 237 (1972).

198. J. Liesener, M. Reicherter, T. Haist, and H. J. Tiziani, "Multi-functional optical tweezers using computer-generated holograms," Opt. Commun. **185**, 77 (2000).

199. R. Di Leonardo, F. Ianni, and G. Ruocco, "Computer generation of optimal holograms for optical trap arrays," Opt. Express **15**, 1913 (2007).

200. J. E. Curtis, B. A. Koss, and D. G. Grier, "Dynamic holographic optical tweezers," Opt. Commun. **207**, 169 (2002).

201. J. Bengtsson, "Kinoform design with an optimal-rotation-angle method," Appl. Opt. **33**, 6879 (1994).

202. S. Hasegawa and Y. Hayasaki, "Holographic Femtosecond Laser Processing with Multiplexed Phase Fresnel Lenses Displayed on a Liquid Crystal Spatial Light Modulator," Opt. Rev. **14**, 208 (2007).

203. M. Pasienski and B. Demarco, "A high-accuracy algorithm for designing arbitrary holographic atom traps," Opt. Express **16**, 2176 (2008).

204. J. Liu and M. Taghizadeh, "Iterative algorithm for the design of diffractive phase elements for laser beam shaping," Opt. Lett. **27**, 1463 (2002).

205. J. Courtial, G. Whyte, Z. Bouchal, and J. Wagner, "Iterative algorithms for holographic shaping of non-diffracting and self-imaging light beams," Opt. Express **14**, 2108 (2006).

206. T. Haist, M. Schonleber, and H. J. Tiziani, "Computer-generated holograms from 3D-objects written on twisted-nematic liquid crystal displays," Opt. Commun. **140**, 299 (1997).

207. C. Liu, G. Zhu, and D. Liu, "Patterning cathode for organic light-emitting diode by pulsed laser ablation," Displays **29**, 117 (2008).

208. Y. Hayasaki, T. Sugimoto, A. Takita, and N. Nishida, "Variable holographic femtosecond laser processing by use of a spatial light modulator," Appl. Phys. Lett. **87**, 031101 (2005).

209. K. Chaen, H. Takahashi, S. Hasegawa, and Y. Hayasaki, "Display method with compensation of the spatial frequency response of a liquid crystal spatial light modulator for holographic femtosecond laser processing," Opt. Commun. **280**, 165 (2007).

210. H. Takahashi, S. Hasegawa, and Y. Hayasaki, "Holographic femtosecond laser processing using optimal-rotation-angle method with compensation of spatial frequency response of liquid crystal spatial light modulator," Appl. Opt. **46**, 5917 (2007).

211. S. Hasegawa and Y. Hayasaki, "Adaptive optimization of a hologram in holographic femtosecond laser processing system," Opt. Lett. **34**, 22 (2009).

212. S. Hasegawa and Y. Hayasaki, "Parallel femtosecond laser processing with a computer-generated hologram," Proc. of SPIE **7201**(2009).

213. Y. Hayasaki, "Optimization methods improve holographic laser performance," SPIE Newsroom, 1-3 (2009).

214. K. Kimura, S. Hasegawa, and Y. Hayasaki, "Diffractive spatiotemporal lens with wavelength dispersion compensation," Opt. Lett. **35**, 139 (2010).

215. "Vistacryl CQ" (Vista Optics, 2011), retrieved Feb 2011, http://www.vista-optics.com/.

216. "UV Fused Silica" (UQG Optics), retrieved Feb 2011, http://www.uqgoptics.com/catalogue/Windows/FUSED_SILICA_PLATES.aspx.

217. "LC-R 2500 - Allround Spatial Light Modulators" (Holoeye, 2011), retrieved Feb 2011, http://www.holoeye.com/spatial_light_modulator_lc_r_2500.html.

218. "LCOS-SLM (Optical Phase Modulator) " (Hamamatsu Photonics, 2011), retrieved Feb 2011, http://jp.hamamatsu.com/products/other/1013/X10468/index_en.html.

219. J. Curtis, C. Schmitz, and J. Spatz, "Symmetry dependence of holograms for optical trapping," Opt. Lett. **30**, 2086 (2005).

220. A. L. Gaeta, "Catastrophic Collapse of Ultrashort Pulses," Phys. Rev. Lett **84**, 3582 (2000).

221. J. Marburger, "Self-focusing: theory," Prog. Quant. Electr. **4**, 35 (1975).

222. N. Boling, A. Glass, and A. Owyoung, "Empirical relationships for predicting nonlinear refractive index changes in optical solids," IEEE J. Quantum Electron. **14**, 601 (1978).

223. G. M. Zverev and V. A. Pashkov, "Self-focusing of laser radiation in solid dielectrics," Sov. Phys. JETP **30**, 616 (1970).

224. Y. Kondo, K. Miura, T. Suzuki, H. Inouye, T. Mitsuyu, and K. Hirao, "Three-dimensional arrays of crystallites within glass by using non-resonant femtosecond pulses," J. of Non-Crystal. Solids **253**, 143 (1999).

225. Y. Shimotsuma, K. Hirao, J. Qiu, and K. Miura, "Nanofabrication in transparent materials with a femtosecond pulse laser," J. Non-Crystal. Solids **352**, 646 (2006).

226. Z. Bor, B. Racz, G. Szabo, M. Hilbert, and H. Hazim, "Femtosecond pulse front tilt caused by angular dispersion," Opt. Eng. **32**, 2501 (1993).

227. J. Hebling, "Derivation of the pulse front tilt caused by angular dispersion," Opt Quant Electron **28**, 1759 (1996).

228. W. Watanabe, S. Sowa, T. Tamaki, K. Itoh, and J. Nishii, "Three-Dimensional Waveguides Fabricated in Poly(methyl methacrylate) by a Femtosecond Laser," Jpn. J. Appl. Phys **45**, L765 (2006).

229. I. V. Ciapurin, L. B. Glebov, and V. I. Smirnov, "Modeling of Gaussian beam diffraction on volume Bragg gratings in PTR glass," Proc. of SPIE **5742**, 183 (2005).

230. A. Baum, P. J. Scully, W. Perrie, D. Liu, and V. Lucarini, "Mechanisms of femtosecond laser-induced refractive index modification of poly(methyl methacrylate)," JOSA B **27**, 107 (2010).

231. B. P. Boczar, N. W. Reese, and M. J. Shoup iii, "Effect of crystal orientation on the insensitive axis bandwidth for second harmonic generation," Appl. Opt. **25**, 170 (1986).

232. A. Marquez, I. Moreno, C. Iemmi, A. Lizana, J. Campos, and M. J. Yzuel, "Mueller-Stokes characterization and optimization of a liquid crystal on silicon display showing depolarization," Opt. Express **16**, 1669 (2008).

233. J. Leach, K. Wulff, G. Sinclair, P. Jordan, J. Courtial, L. Thomson, G. Gibson, K. Karunwi, J. Cooper, Z. J. Laczik, and M. Padgett, "Interactive approach to optical tweezers control," Appl. Opt. **45**, 897 (2006).

Appl Phys B (2010) 101: 817–823
DOI 10.1007/s00340-010-4205-5

Applied Physics B
Lasers and Optics

High-speed uniform parallel 3D refractive index micro-structuring of poly(methyl methacrylate) for volume phase gratings

D. Liu · Z. Kuang · W. Perrie · P.J. Scully · A. Baum · S.P. Edwardson · E. Fearon · G. Dearden · K.G. Watkins

Received: 9 March 2010 / Revised version: 1 June 2010 / Published online: 15 September 2010
© Springer-Verlag 2010

Abstract Parallel femtosecond refractive index laser inscription of clinical grade poly(methyl methacrylate) (PMMA) at 775 nm, 170 fs pulselength is demonstrated with multiple low fluence beams generated with the aid of a spatial light modulator. Using optimised computer-generated holograms (CGHs), 16 diffracted near identical beams were focused simultaneously within bulk PMMA to create a series of 19 μm pitch, 5 mm × 5 mm × 1–4 mm thick volume phase gratings at high speed. First order diffraction efficiency rises with grating thickness in accord with diffraction theory, reaching 75% at the first Bragg angle (4 mm thick) with fabrication time around 1 hour. By carefully stitching filamentary modifications while eliminating effects such as pulse front tilt during inscription, gratings exhibit high uniformity, which has not been achieved previously using femtosecond inscription. Highly uniform modification is exhibited throughout the material consistent with the observed excellent angular selectivity and low background scatter and quantitative comparison with first order diffraction theory is satisfactory. The diffraction efficiency and hence refractive index profile shows a temporal behaviour related to the material response after exposure. Simultaneous 3D modification at different depths is also demonstrated, highlighting the potential of creating complex 3D integrated optical circuits at high speed through the application of CGHs.

D. Liu · Z. Kuang · W. Perrie (✉) · S.P. Edwardson · E. Fearon · G. Dearden · K.G. Watkins
Laser Group, Department of Engineering, University of Liverpool, Liverpool L69 3GQ, UK
e-mail: wpfemto1@liverpool.ac.uk
Fax: +44-151-650-2304

P.J. Scully · A. Baum
Photon Science Institute, University of Manchester, Manchester M13 9PL, UK

1 Introduction

Femtosecond laser refractive index modulation (Δn) of optical materials is a route to the creation of complex 3D photonic circuits. Non-linear absorption induced at the focus leads to highly localised modification while translation of the focal spot within the solid creates desired 3D structures. Clinical grade poly(methyl methacrylate) (PMMA), in particular, is attractive due to favourable characteristics such as optical transparency, processability and low cost. Bulk Δn modification of pure PMMA is of interest because of the potential of creating useful devices for clinical, biological and chemical applications which can be integrated with lab-on-chip micro-fluidic devices.

In the NIR, temporal pulse duration $\tau < 100$ fs generates highest Δn in PMMA by reducing avalanche ionisation relative to multi-photon ionisation [1]. For pulse duration $\tau > 150$ fs, where optical breakdown is increasingly more likely, effective Δn modification of PMMA was shown at shorter wavelength $\lambda = 387$ nm, 170 fs by reducing the order of non-linear absorption from three to two-photon [2].

Similarly, the measured Δn inscribed in fused silica in the NIR (800 nm, 1 kHz, $E_p \approx 1$ μJ, NA = 0.1) decreased as the temporal pulselength was increased above 130 fs with the appearance of optical breakdown at $\tau > 230$ fs [3]. At 1 kHz, (170 fs, 387 nm, $E_p \approx 1$ μJ, NA = 0.03) the resulting Δn in PMMA has been shown to be positive [2], essential for single mode waveguides, whereas a 25 MHz laser (30 fs, 800 nm, 20 nJ, NA = 0.25) generated tubular longitudinal waveguides probably due to increased thermal effects [4].

Optical memory [5], phase gratings [1], symmetric waveguides [6] and 3D couplers [7] have been demonstrated with single point femtosecond processing in PMMA. However, the extension to complex 3D optical circuits with a range of embedded components may be significantly hampered, due to the long inscription times required. In addition,

spherical aberration introduced at the air/dielectric interface, increasing with NA, reduces on-axis intensity severely, constraining the useful modification depths [8]. The use of a low NA < 0.2 objective here, which encourages filamentation is ideal for thick volume grating manufacture, since spherical aberration from the interface is expected to be negligible, allowing uniform modification up to depths >5 mm below the interface, whereas with a high NA = 0.75 objective, spherical aberration would limit modification depth to <30 μm from the interface unless pre-compensated on the objective [8] or on the SLM.

At 1 kHz, femtosecond pulses with energy E_p < 1 μJ are typically focused within an optical substrate with a single beam while carefully scanning the substrate longitudinally or transversely to generate the required Δn. However, since pulse energy E_p > 1 mJ is generally available at 1 kHz, the light utilisation factor is <0.1%. By using a Spatial Light Modulator (SLM), addressed with appropriate CGH's to create a large number of diffracted beams of the requisite pulse energy, this efficiency is increased by more than an order of magnitude, reducing the fabrication time while allowing arbitrary parallel processing [9–11]. Recently, in fused silica, by using a dynamic binary phase mask created by an SLM combined with a low NA optic, 2-beam 3D parallel writing of efficient waveguide couplers was demonstrated [12]. One approach to rapid fabrication of volume phase gratings in Foturan photosensitive glass uses a line focus (2 μm × 1800 μm) with energetic 80 μJ, 40 fs, 800 nm pulses at 1 kHz. However, the modification was quite non-uniform due to filamentation during exposure [13].

In this paper, uniform modification with depth is achieved by paying particular attention to control of filamentation, limiting filament length by controlling pulse energy thus avoiding re-focussing, which would otherwise create width variations in longer filaments. In addition, intensity variations between spots are minimised through optimising CGH's while eliminating possible asymmetry from writing direction due to pulse front tilt. Consequently, highly parallel, uniform Δn structuring inside PMMA is achieved to produce large, high-quality, efficient volume phase gratings in minutes rather than hours, thus speeding refractive index engineering.

2 Experimental

The output from a Clark-MXR CPA-2010 fs laser system (775 nm, 170 fs pulse duration, 1 kHz repetition rate, 1 mJ) was attenuated and expanded to 8 mm diameter onto a phase only reflective liquid crystal on silicon SLM (Hamamatsu X10468-01, AOI <10°) which has 800 × 600 pixels (16 mm × 12 mm) with reflectivity >95% and diffraction efficiency η > 60%. As shown in Fig. 1, a 4f optical system

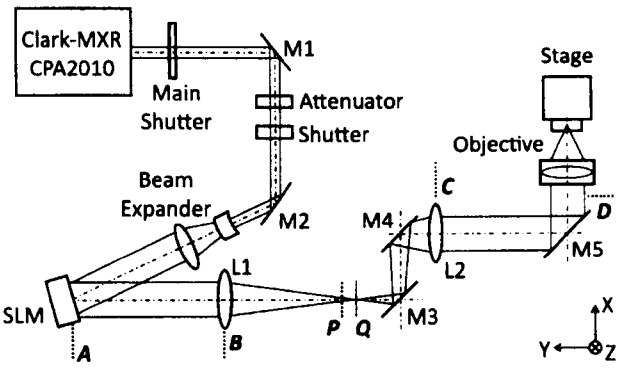

Fig. 1 Schematic of experimental system for parallel 3D Δn structuring of PMMA. A 4f optical system (L1, L2) with unity magnification helps to remove the residual zero order beam at plane P while re-constructing the complex field at plane D

was introduced to remove the remaining energetic zero order reflection at Plane P, near the Fourier plane of lens L1 (plane Q) using a small absorbing target on axis [14]. First order diffracted beams, however, focus off axis and so are transmitted through the 4f system consisting of two plano-convex lenses L1 and L2 ($f_1 = f_2 = 200$ mm) which essentially re-image the surface of the SLM to the back focal plane (D) of a long working distance microscope objective (Nikon, type CFI LU Plan Fluor BD 5×, 0.15 NA, $f = 40$ mm, $WD = 18$ mm). Distance $AD = 4f$ while distance $AB = BQ = QC = CD = f$. The complex optical field at plane D was therefore identical with that at plane A after reflection from the SLM. PMMA substrates were obtained from Vista Optics, UK, (Vistacryl CQ non UV) which has $n = 1.492 \pm 0.002$, T > 90% visible transmission (350–900 nm) and residual monomer MMA <1%. These were optically polished on all sides, mounted on a precision 3-axis motion control system (Aerotech), and diffracted beams were carefully focused >0.5 mm below the substrate to keep the fluence at the interface below the damage threshold. An effective value of $NA_{eff} = 0.1$ was used here.

From the desired intensity distribution at the focal plane of the objective, the corresponding CGH was calculated using the Gerchberg-Saxton algorithm within an interactive LabView environment was applied to the SLM and the calculated phase pattern (8-bit greyscale) was observed on a separate monitor [14]. As spots can be focussed at different planes by effectively adding phase Fresnel lenses, simultaneous modification at separate planes was also possible as illustrated in Fig. 2(b).

Periodic spot patterns with a high degree of symmetry (Fig. 2(c)) creates degeneracy, leading to non-uniform intensity in diffracted beams from overlapping ghosts, resulting in significant intensity modulation [15]. Uniformity is improved greatly by breaking symmetry, for example, by introducing slight random displacements of the required spot pattern (Fig. 2(d)) If N is a random number chosen between

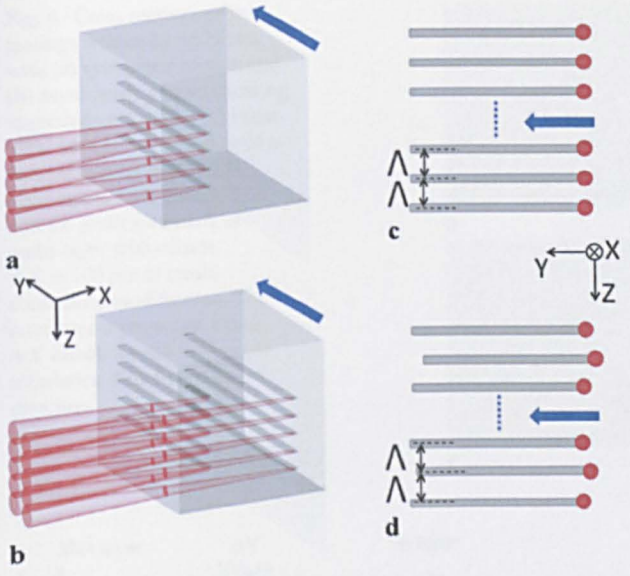

Fig. 2 Parallel writing inside PMMA. Transverse geometry for writing gratings in (**a**) single layer and (**b**) double layer. Parallel spots in (**c**) symmetric and (**d**) asymmetric pattern which improves intensity uniformity in diffracted beams. The *arrows* denote the translation direction ($+Y$) of the sample

-1 and $+1$ and shift range $S = 20$ μm, the spots were offset randomly by a distance $N \times S$ in the Y axis (scan direction) while maintaining fixed pitch Λ (Fig. 2(d)).

3 Results and discussion

An important parameter along with pulse energy, temporal pulselength, wavelength and scan speed in Δn structuring is also scan direction, which can lead to a variation in modified region dimensions due to the effect of pulse front tilt exhibited by many ultrafast laser systems [16]. We have observed this effect while modifying PMMA, Fig. 3, which demonstrates the difference in structuring width obtained when reversing scan direction during single beam Δn structuring at low NA. This effect was also accompanied by the observation of a significant change in the intensity of the plasma emission while writing in opposite directions. To eliminate this non-uniformity the substrates were scanned in a single direction only, essentially increasing the fabrication time.

Δn modification of PMMA without optical breakdown at 775 nm, 170 fs with 16 parallel beams with a period $\Lambda = 19$ μm is shown in the optical micrographs of Fig. 4(a–d). Pulse energy $E_p = 0.6$ μJ/beam and transverse scan speed $s = 1$ mm/s were used and each modified region was scanned once only. The cross section of modified structures written with a symmetric beam pattern, depicted in Fig. 4(a), show a large variation in filament length $l = 106.2 \pm 26.3$ μm (1σ), emphasising the intensity non-uniformity generated with this geometry.

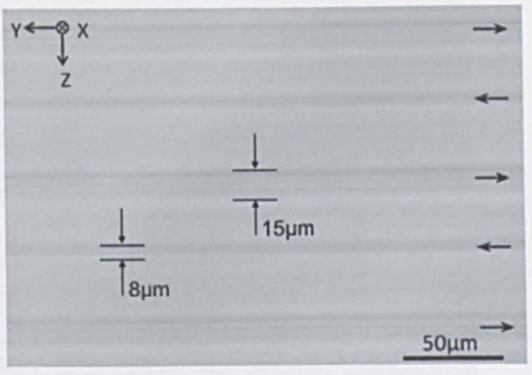

Fig. 3 Optical image showing modification asymmetry observed in single beam writing with scan direction due to pulse front tilt ($E_P = 0.6$ μJ, $s = 0.8$ mm/s, NA $= 0.04$)

Adding a slight random asymmetry in the spot pattern, as discussed above in Sect. 2, Fig. 2(d), removes degeneracy and ghost beam overlap, reducing intensity modulation, hence structure quality improved markedly, Fig. 4(b) with measured filament length $l = 109.9 \pm 6.1$ μm (1σ). With this optimisation, Fig. 4(c) shows a front view of 16 near-uniform lines written simultaneously within PMMA while the cross section of a thick volume grating structure is shown in Fig. 4(d), generated by offsetting the parallel written structures along the optical axis in the X direction so as to create a continuous modification. An overlap of filaments by a distance of 10 μm (~10% overlap) was found to be satisfactory to achieve continuity and uniformity and is shown schematically in Fig. 5.

The modified regions (4 μm wide) are $l = 110$ μm in depth, while the calculated depth of focus is $DOF \approx 0.71 M^2 n\lambda/(\pi \mathrm{NA}^2) \approx 34$ μm ($n = 1.49$, $M^2 = 1.3$) so that the effect of self-focussing and filamentation is significant. This is not surprising as the peak power $P = 4$ MW $\gg P_c =$ 23 kW, the critical power for self-focussing in PMMA [17]. The relatively long modification depth is due to the dynamic balance between Kerr self-focussing and the defocussing effects of the electron plasma generated during the ionisation process. A recent study of refractive index filaments created in PMMA with 100 fs, NIR, 1 kHz pulses with 0.1 NA had length $l = 200$ μm at 0.8 μJ pulse energy [18].

By scanning this 16 beam optimised intensity distribution in the transverse ($+Y$) direction with Z-axis increments ΔZ of 304 μm (16 × 19.0 μm), then offsetting in the axial (X) direction with ΔX of ~ 100 μm (deepest first), a thick grating (35 layers) with dimensions of 5 mm × 5 mm × 3.5 mm thick was created in about 50 minutes. A synchronised fast mechanical shutter ($\tau_r \approx 3$ ms) controlled from within the motion control software avoided unwanted exposure of material.

The grating efficiency at the Bragg angle of the first three orders shows a remarkable time dependence, Fig. 6, developing over periods of days and saturating, in the case of first

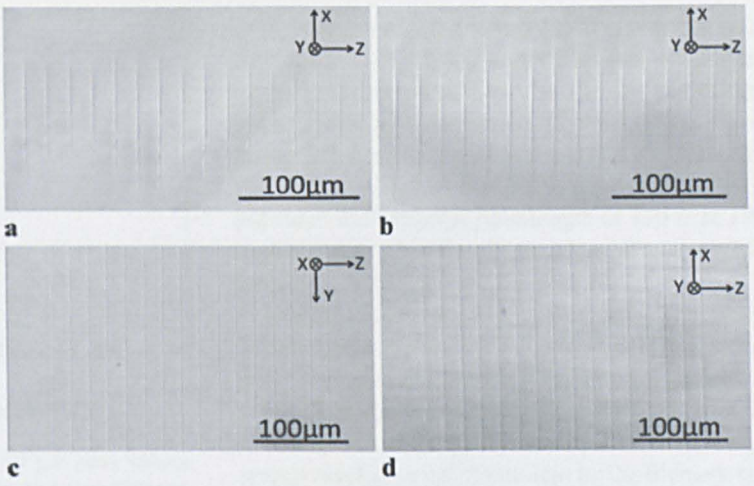

Fig. 4 Cross sections of the gratings written by 16 beams with (**a**) symmetric pattern and (**b**) asymmetric pattern showing improved uniformity. (**c**) Front view and (**d**) cross section of a volume grating written by asymmetric spot pattern. The volume grating consists of multi-layer with offsets $\Delta X = 100$ μm to create continuous modification. The laser beams propagate along $+X$ direction, and the sample translation direction is in $+Y$ direction

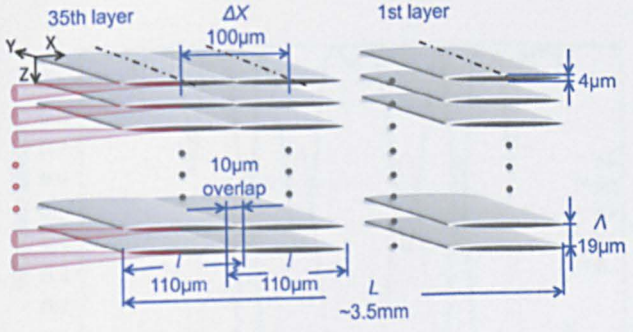

Fig. 5 Schematic of multi-beam modification to create continuous volume phase grating by stitching filamentary modifications with offsets $\Delta X = 100$ μm and hence 10 μm overlaps

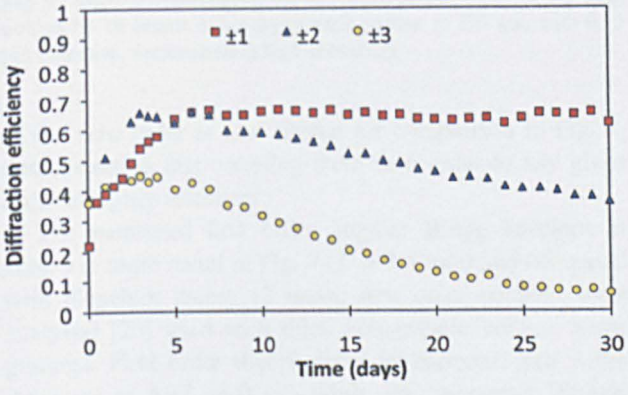

Fig. 6 Diffraction efficiency at the Bragg angles for first to third orders showing temporal behaviour

order to $\eta_{max} = 66\%$ after one week for a grating thickness of 3.5 mm. This suggests that the material modifies and relaxes after exposure due to the diffusion of monomer MMA molecules, the most likely breakdown photo product, combined with cross linking [3]. Even after 30 days, where first and third orders have essentially stabilised, the second order diffraction efficiency is still changing. The inference is that the Δn modulation is altering both temporally and spatially as the MMA molecules diffuse out into the unexposed regions between the grating lines. More stable structures may be expected at shorter pulselength $\tau = 100$ fs in the NIR where multi-photon ionisation increases relative to impact ionisation or at shorter NUV wavelengths [1, 2].

Watanabe [7], while creating 3D directional couplers in PMMA using 1 kHz, 85 fs pulses at 800 nm, observed temporal changes in waveguide cross sections, indicating that refractive index profile in the central region altered over a period of ~ 20 minutes after irradiation, with the RI change Δn going from negative to positive and reaching a maximum value of $\sim 4.6 \times 10^{-4}$.

The grating thickness parameter is given by $Q = 2\pi\lambda L/(n\Lambda^2)$, where L is the grating thickness and $n = 1.49$ is the refractive index of the bulk PMMA hence $6.3 < Q < 21.9$ ($1 < L < 4$ mm) so that gratings ($Q > 10$) are thick volume gratings [19], and hence should show a high angular selectivity.

The measured angular diffraction efficiency $\eta(\theta)$ at $\lambda = 532$ nm (Coherent Verdi 2, $M^2 = 1.01$) one week after exposure is shown in Fig. 7 ($L = 3.5$ mm, first order) and Fig. 8 (1^{st}–4^{th} orders). For measurements, the laser output was attenuated while substrates were attached to a mirror mount and translation stage mounted on a high-resolution rotation stage so that gratings could first be brought carefully to normal incidence. The peaks appear close to the calculated Bragg angles $\theta_B = \arcsin(m\lambda/2\Lambda) = 0.80°$ ($m = 1$, experimental Bragg angle $\theta_{B(exp)} = 0.81°$), 1.60° ($m = 2$), 2.41° ($m = 3$) and 3.21° ($m = 4$), where m is the order of diffraction.

A silicon detector with power meter (Coherent LM1/Fieldmaster) was used to measure the transmitted power into each order. The curves were measured by placing the detector in turn at the location of each diffracted order and rotating the grating from normal incidence. The symmetrical response is very satisfactory. The intensity drop measured

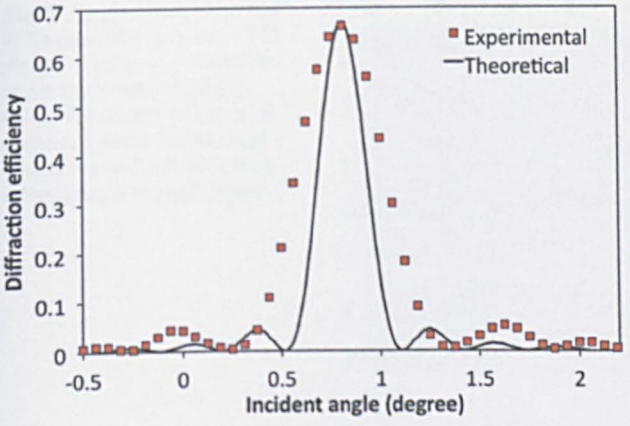

Fig. 7 First order Bragg angular envelope of 19 μm pitch volume phase grating (5 × 5 × 3.5 mm) written by 16 uniform beams and comparison with first order theory [20]

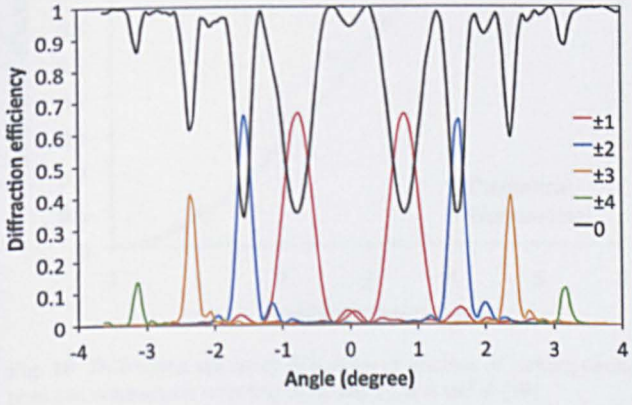

Fig. 8 Angular selectivity of volume phase grating (5 × 5 × 3.5 mm) written by 16 beams using asymmetric pattern at 775 nm, with 0.15 NA objective, demonstrating high selectivity

in the zero order is also shown for comparison in Fig. 8, demonstrating that coupling from zero order to any given order is highly selective.

The measured first order angular Bragg envelope is shown in more detail in Fig. 7 ($L = 3.5$ mm) and compared with Kogelnik theory (2 wave, first order coupled wave analysis) [20] used with thick holographic volume phase gratings. First order theory gives an expected half width $\Delta\theta_{\mathrm{FWHM}} = \Lambda/L = 0.31°$ while the measured FWHM $\Delta\theta_{\mathrm{FWHM(exp)}} = 0.47 \pm 0.02°$, a factor of 1.5 wider, however, the general curve with side lobes is well reproduced. Holographic gratings have a harmonic refractive index modulation $\Delta n = \Delta n_0 \cos(2\pi z/\Lambda)$ while the index modulation profile here must be quite different from sinusoidal.

The second order, as expected gives higher resolution with $\Delta\theta_{\mathrm{FWHM(exp)}} = 0.24 \pm 0.01°$. The expected first order diffraction efficiency can be estimated from $\eta_{\pm 1} = \sin^2(\pi \Delta n_0 L/\lambda \cos\theta_b) = \sin^2\phi$ where Δn_0 is the amplitude of modulation and θ_b is the first order Bragg angle [19]. A graph of the measured diffraction efficiency of a series of gratings written under identical conditions with increasing thickness is shown in Fig. 10 and compared with the expected $\sin^2\phi$ function. Highest diffraction efficiency, $\eta_b = 75\%$ is observed at 4 mm thickness. The fit is consistent with a $\Delta n_0 = 4.6 \times 10^{-5}$, quite modest but not unexpected at the temporal pulselength of 170 fs at 775 nm. The high efficiency here has been achieved as a result of the uniformity and thickness of the gratings.

Figure 9(a–g) shows a photographic image of the diffracted spots when projected on a distant screen as the volume grating was rotated while Fig. 9(h–n) shows the measured intensity in a given order, normalised to scale.

Using the technique demonstrated here, the maximum spatial resolution will be limited by the filament widths, here measured to be ~ 4 μm so that a pitch below $\Lambda < 8$ μm (i.e. > 125 lines/mm) is unlikely with this material and geometry. We have diffracted up to 30 beams simultaneously, however, at a cost of intensity uniformity with the calculated CGH's. While grating thicknesses (through stitching filaments) of up to 4 mm have been demonstrated (40 layers) a slight reduction in the filament length (~ 10%) was observed with thickness greater than 3.5 mm in PMMA. This factor may well limit the maximum thickness, uniformity and efficiency achievable using this technique. The development of the first order efficiency over ~ 7 days infers a $(\Delta n/\Delta t) \approx 0.66 \times 10^{-5}$/day. As pitch decreases, MMA diffusion might well be restricted so that Δn contrast between exposed and unexposed might drop so limiting the grating efficiency. More stable structures may be expected at shorter pulselength $\tau = 100$ fs in the NIR where multi-photon ionisation increases relative to impact ionisation or at shorter NUV wavelengths, [1, 2]. Accelerated development of the modulation might be achieved through thermal treatment of the polymer after exposure [21].

By re-calculating CGHs to offset the focal planes of particular spots, simultaneous parallel 3D writing at different depths using 16 (2 × 8) beams in a double layer and 15 (3 × 5) beams in triple layer were demonstrated, as shown in the cross sections of Fig. 11(a, b). At this stage, CGHs have not been optimised.

4 Conclusions

Highly parallel diffractive writing of uniform Δn structures in PMMA was demonstrated by combining 775 nm, 1 kHz, 170 fs pulses with an phase only SLM addressed with CGH's giving a throughput gain $G = 16$, a potentially useful step in the high-speed production of 3D optical photonic components. The uniformity of filamentary modification is achieved by minimising diffractive intensity modulation through CGH optimisation while limiting filamentary modifications to ~ 110 μm lengths at NA = 0.1, then carefully

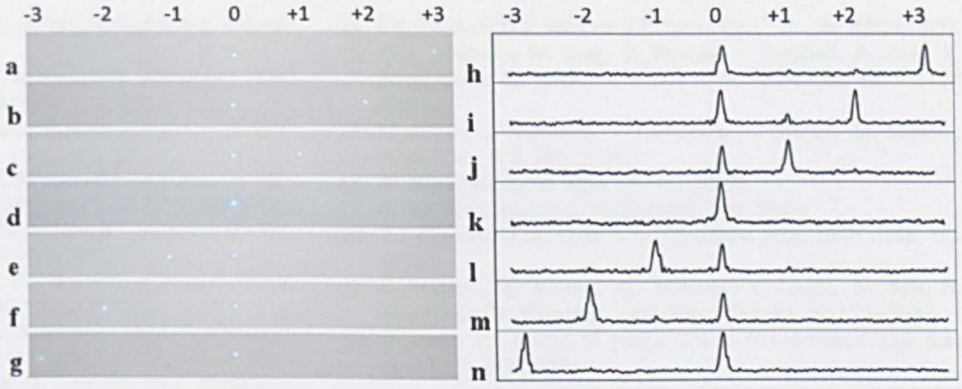

Fig. 9 (**a**–**g**) Composite image of Bragg diffraction at $\lambda = 532$ nm (**a**) +3rd to (**g**) −3rd order of the thick volume grating. (**h**–**n**) The relative intensity of measured peaks. Background scatter is low. Note the fidelity of coupling into given orders

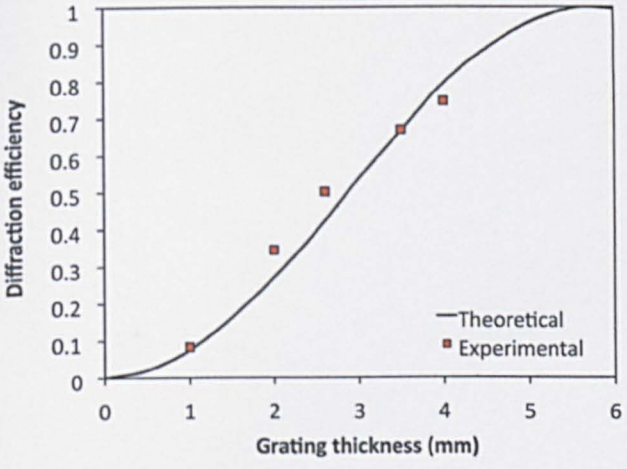

Fig. 10 Diffraction efficiency of a series of gratings of varying thickness and comparison with first order theory, $\eta = \sin^2 \phi$ [19]

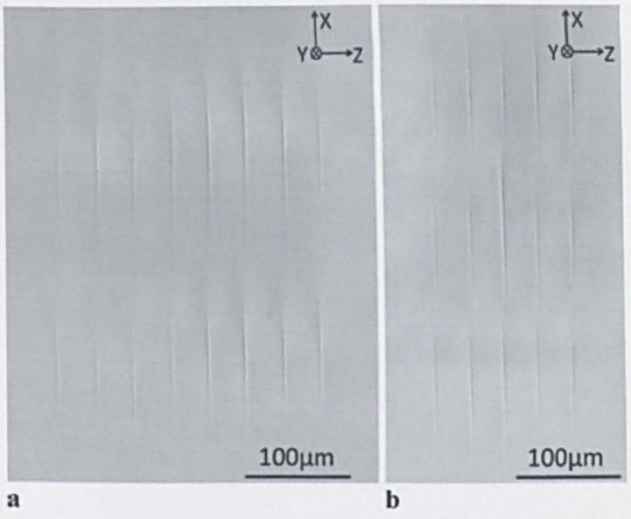

Fig. 11 Optical micrographs of 3D modified cross sections in PMMA written in parallel by (**a**) 16 (2 × 8) beams in double layer and (**b**) 15 (3 × 5) beams in a triple layer

overlapping axial filaments to produce a continuous modification. In addition, the asymmetry due to pulse front tilt was eliminated by inscribing in a single direction only. Consequently, thick, high-quality volume phase gratings (5 × 5 mm, 53 lines/mm) with up to 4 mm thickness and $\eta_b = 75\%$ first order diffraction efficiency have been produced at high speed. The measured Bragg angular envelope is similar but wider by a factor of 1.5 when compared to first order theory [20] while the diffraction efficiency with grating thickness increases with the expected $\sin^2 \phi$ function [19], consistent with a refractive index modulation $\Delta n_0 = 4.6 \times 10^{-5}$. Temporal changes in refractive index are observed after material inscription, probably related to the primary photoreaction product, most likely monomer MMA which diffuses into the bulk over periods of days to weeks since monomer MMA is soluble in PMMA. Monomer present in the bulk reduces the refractive index there, while exposed regions may also suffer from cross linking, increasing the refractive index [22].

Simultaneous 3D modification at different depths within the bulk is also demonstrated here through the application of phase Fresnel lenses. Future work including long term volume grating stability test and further chemical analysis will be carried out.

Acknowledgements This work was supported by the UK North West Development Agency under grant N0003200. The authors are grateful to Prof. Miles Padgett and Dr. Jonathan Leach of the University of Glasgow for providing the SLM control software and Hamamatsu Photonics for supplying the SLM.

References

1. A. Baum, P.J. Scully, W. Perrie, D. Jones, R. Issac, D.A. Jaroszynski, Opt. Lett. **33**, 651 (2008)
2. A. Baum, P.J. Scully, M. Basanta, C.L. Paul Thomas, P.R. Fielden, N.J. Goddard, W. Perrie, P.R. Chalker, Opt. Lett. **32**, 190 (2007)
3. H. Guo, H. Jiang, Y. Fang, C. Peng, H. Yang, Y. Li, Q. Gong, J. Opt. A, Pure Appl. Opt. **6**, 787 (2004)
4. A. Zoubir, C. Lopez, M. Richardson, K. Richardson, Opt. Lett. **29**, 1840 (2004)
5. K. Yamasaki, S. Juodkazis, M. Watanabe, H.B. Sun, S. Matsuo, H. Misawa, Appl. Phys. Lett. **76**, 1000 (2000)
6. S. Sowa, W. Watanabe, T. Tamaki, J. Nishii, K. Itoh, Opt. Express **14**, 291 (2006)

7. W. Watanabe, S. Sowa, T. Tamaki, K. Itoh, J. Nishii, Jpn. J. Appl. Phys. **45**, L765 (2006)
8. C. Hnatovsky, R.S. Taylor, E. Simova, V.R. Bhardwaj, D.M. Rayner, P.B. Corkum, J. Appl. Phys. **98**, 013517/1-5 (2005)
9. Y. Hayasaki, T. Sugimoto, A. Takita, N. Nishida, Appl. Phys. Lett. **87**, 031101 (2005)
10. Z. Kuang, W. Perrie, J. Leach, M. Sharp, S.P. Edwardson, M. Padgett, G. Dearden, K.G. Watkins, Appl. Surf. Sci. **255**, 2284 (2008)
11. Z. Kuang, W. Perrie, D. Liu, S. Edwardson, J. Cheng, G. Dearden, K. Watkins, Appl. Surf. Sci. **255**, 9040 (2009)
12. C. Mauclair, G. Cheng, N. Huot, E. Audouard, A. Rosenfeld, I.V. Hertel, R. Stoian, Opt. Express **17**, 3531 (2009)
13. F. He, H. Sun, M. Huang, J. Xu, Y. Liao, Z. Zhou, Y. Cheng, Z. Xu, K. Sugioka, K. Midorikawa, Appl. Phys. A **97**, 853 (2009)
14. J. Leach, G. Sinclair, P. Jordan, J. Courtial, M.J. Padgett, J. Cooper, Z. Laczik, Opt. Express **12**, 220 (2004)
15. J.E. Curtis, C.H.J. Schmitz, J.P. Spatz, Opt. Lett. **30**, 2086 (2005)
16. P.G. Kazansky, W. Yang, E. Bricchi, J. Bovatsek, A. Arai, Y. Shimotsuma, K. Miura, K. Hirao, Appl. Phys. Lett. **90**, 151120 (2007)
17. M. Miwa, S. Juodkazis, T. Kawakami, S. Matsuo, H. Misawa, Appl. Phys. A **3**, 561 (2001)
18. W. Watanabe, Laser Phys. **19**, 342 (2009)
19. H. Kogelnik, Bell Syst. Tech. J. **48**, 2909 (1969)
20. I.V. Ciapurin, L.B. Glebov, V.I. Smirnov, Proc. SPIE **5742**, 183 (2005)
21. S. Hirono, M. Kasuya, K. Matsuda, Y. Ozeki, K. Itch, H. Mochizuki, W. Watanabe, Appl. Phys. Lett. **94**, 241122 (2009)
22. A. Baum, P.J. Scully, W. Perrie, D. Liu, V. Lucarini, J. Opt. Soc. Am. B **27**, 107 (2010)

expected, $\Delta\theta = \Lambda/L = 0.43°$ for a sinusoidal refractive index profile [160], while the second and third orders have $\Delta\theta \approx 0.33°$ and 0.23°, respectively.

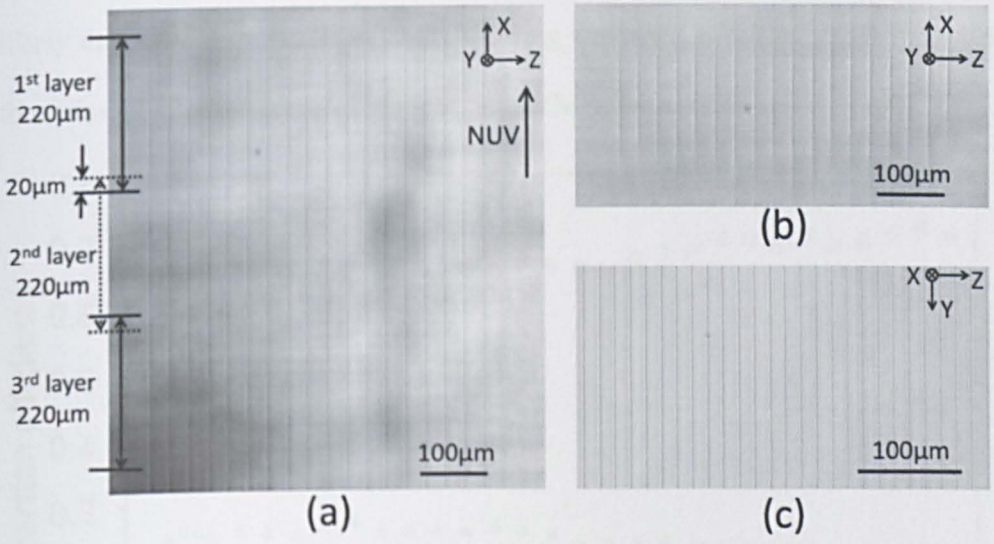

Fig. 6.6-1: (a) Continuously modified cross-section created by overlapping 3 layers each separated by $\Delta X = 200$ μm along optic axis. (b) Cross-section of 18 parallel beams modification of PMMA with $\Lambda_1 = 30$ μm. (c) Front view of a grating with $\Lambda_2 = 15$ μm pitch.

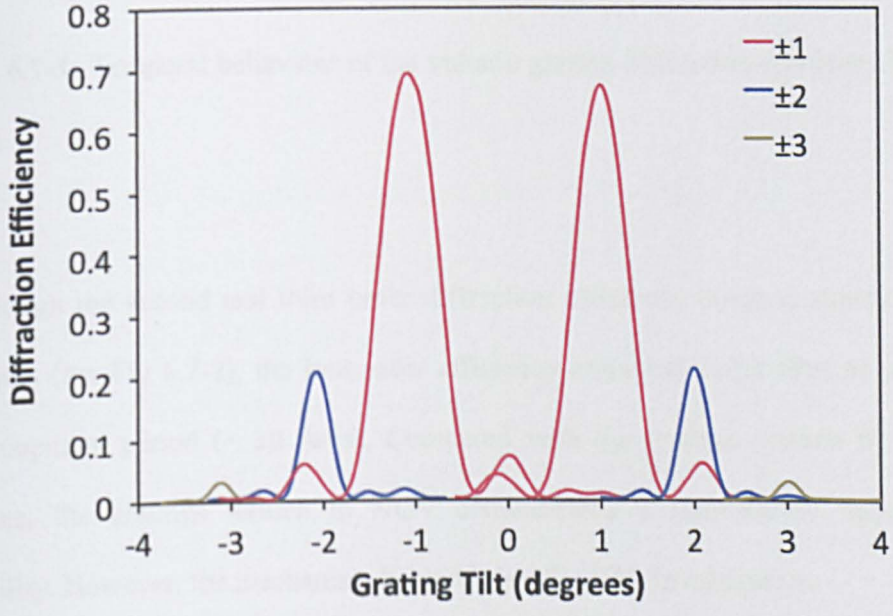

Fig. 6.6-2: Detailed measurements of the Bragg diffraction efficiency of ±1st, ±2nd and ±3rd orders after 30 days at 532 nm readout wavelength.